TOWARD INTRALUMINAL FORCE MONITORING AND AUTOMATED INSERTION IN ROBOTIC ENDOVASCULAR INTERVENTION

Masoud Razban

A thesis

In the Department

of

Mechanical, Industrial and Aerospace Engineering

Presented in Partial Fulfillment of the Requirements

For the Degree of

Doctor of Philosophy (Mechanical Engineering) at

Concordia University

Montréal, Québec, Canada

January 2021

Concordia University
School of Graduate Studies

This is to certify that the thesis prepared

By: **Masoud Razban**

Entitled: **Toward Intraluminal Force Monitoring and Automated Insertion in Robotic Endovascular Intervention**

and submitted in partial fulfillment of the requirements for the degree of

Doctor of Philosophy(Mechanical Engineering)

complies with the regulations of this University and meets the accepted standards with respect to originality and quality.

Signed by the final examining committee:

Dr. Arash Mohammadi	Chair
Dr. Rosaire Mongrain	External Examiner
Dr. Hassan Rivaz	External to Program
Dr. Youmin Zhang	Examiner
Dr. Gerard J. Gouw	Examiner
Dr. Javad Dargahi	Thesis Co-supervisor
Dr. Benoit Boulet	Thesis Co-supervisor

Approved by

Dr. Ivan Contrerast, Graduate Program Director

March/12/2021

Dr. Mourad Debbabi, Interim Dean
Gina Cody School of Engineering and Computer Science

Abstract

Toward Intraluminal Force Monitoring and Automated Insertion in Robotic Endovascular Intervention

Masoud Razban, Ph.D.
Concordia University, 2021

Endovascular interventions have been broadly embraced in treating and diagnosing vascular and cardiac diseases. The robotic practice of endovascular procedures has significantly reduced radiation exposure of clinicians and improved the precision, stability and controllability of interventional tool motion. Despite improvements in tools and robotic systems, intraprocedural risks of complications including perforation, dissection, embolization, thrombosis, brain lesions, and stroke are still high. Studies pointed out tool-tissue interaction on the arterial wall as the leading cause of complications and the associated post-treatment risks. Clinicians have limited knowledge of intraluminal interactions taking place through the length of endovascular tools during navigation as well as limited control over such interactions. This research proposes a framework for measurement, monitoring, and control of intraluminal contact force (ICF) of endovascular devices. This thesis presents an image-based sensing solution to estimate multiple contact forces (CF) along the catheter/guidewire and delivers an ICF monitoring system during endovascular navigation. It also proposes a semi-automated robotic framework limiting ICF using image-based control methods.

The proposed sensor-less approach employs a numerical finite element simulation of the tool using image-based data. Real-time image segmentation and tracking algorithms are developed to extract tool shape and compute contact deflections and pose data. An FEM model is built using nonlinear beam elements and image-based pose measurements. The model requires tool flexural rigidity distribution as a fixed-parameter input. Accordingly, a set of experiments are performed to measure the equivalent flexural rigidity along the tool using sequential three-point bending tests. To validate the accuracy of contact force estimations, an experimental setup is prepared with separated contact point phantoms allowing direct CF measurements via a F/T

sensor. The results show the effectiveness of the proposed approach in accurately estimating multi-point CFs at the side of an interventional tool. In a second study, the proposed force estimation concept is used to implement an image-based intraluminal tool-vessel interaction monitoring system, which has been tested on teleoperated robotic cannulation of aortic arteries in an anthropomorphic phantom. Moreover, this study compares intraluminal CF with the total force exerted on the vascular phantom to highlight the importance of monitoring local tool-tissue interactions. In the experimental setup, a robotic driver system is designed and fabricated based on the methods in conventional manual navigation. The FEM model is updated to consider large axial, bending and shear deformation. Detection and tracking of contacts within the phantom and computation of tool pose are obtained through a real-time imaging algorithm. The proposed method achieved intraluminal monitoring by tracking multi local ICF during procedure and building ICF contour on the phantom arterial wall. Results suggest that high-risk local overloading may happen even when vascular insertion force is low. The image-based method also computes structural stress of the tool in practice. The proposed online tool-tissue monitoring method delivers insight into the intraluminal interactions and is well-suited for clinician visual guidance, robotic control systems, and research tool design.

The final part of the thesis presents a semi-automated robotic insertion framework to control the intraluminal interaction forces under a prescribed safe reference while advancing the navigation procedure. The method uses the proposed image-based force sensing feedback in a velocity-actuated contact force control loop to perform regulated insertion. An automated retraction-reinsertion feature is developed using visual servoing of the tip to relax the excessive forces and extreme deflection caused by friction build-up. The system switches between ICF control and tip visual servoing to advance the navigation. The proposed automated insertion achieved effective control on intraluminal interaction forces during aortic arteries navigation. Experimental study demonstrates superior performance of the automated framework compared to manual teleoperation modes with and without utilizing visual ICF monitoring. Automated ICF control can minimize the risk of complications and enhance the quality of endovascular procedures. Employing ICF as a visual monitoring also improved the task performance compared to traditional teleoperation in both force and motion metrics.

Acknowledgments

I would like to offer my sincere gratitude to my co-supervisors Dr. Javad Dargahi and Dr. Benoit Boulet for their support and guidance, for providing me with this unique and rewarding learning experience, and for granting me the academic freedom to pursue an interesting research topic. A warm and kind thank goes to the member of Robotic Surgery labs and Concordia university staff for creating a friendly and motivating environment.

During my Ph.D. study, I had the opportunity to attend in *Surgical Innovation Program*, a cross-disciplinary graduate program that equips trainees to enter the clinical technology sector. I like to thank *Experimental Surgery department* of *McGill University* for leading the program with clinical resources and hospital visits, and all other universities and organizations for their supports. I also like to acknowledge the financial support of *Fonds de recherche du Québec–Nature et technologies (FRQNT)*, *Natural Sciences and Engineering Research Council of Canada (NSERC)*, *CREATE-Innovation at the Cutting Edge*, and Concordia University Research Office.

Lastly and most importantly, I love to express my deepest appreciation and gratitude to my wife, Elaheh, for her encouragement, inspiration, support, and patience through every moment of this journey. My heartfelt appreciation goes to my parents, Hossein and Masoomeh, who have been seamless support and inspiration in every stage of my life.

DEDICATION

TO MY BELOVED ELLY

Contents

List of Figures

List of Tables

Acronyms

Acronyms	Definition
2D	Two-Dimensional
3D	Three-Dimensional
ACR	Automatic Catheter Retraction
CF	Contact Force
CGCI	Catheter Guidance Control and Imaging
CPP	Contact Point Phantom
CTO	Chronic-Total-Occlusion
DOF	Degree-of-Freedom
DWI	Diffusion Weighted Imaging
EAM	Electroanatomic Mapping
EP	Electrophysiology
EPI	Echo-Planar Imaging
ICFM	Intraluminal Contact Force Monitoring
F/T	Force-Torque
FIT	Force Impact over Time
FPS	Frame per Second
GW	Guidewire
HSV	Hue, Saturation, Value
ICF	Intraluminal Contact Force
LCCA	Left Common Carotid Artery
LSA	Left Subclavian Artery
MRI	Magnetic Resonance Imaging
MS	Motion Smoothness
PCI	Percutaneous Coronary Intervention
PID	Proportional-Integral-Derivative
PVD	Peripheral Vascular Disease
PVI	Peripheral Vascular Intervention

Acronyms	Definition
RCCA	Right Common Carotid Artery
RIFCC	Robotic Intraluminal Force Control Catheterization
RF	Radiofrequency
RF	Resultant Force
RMN	Robotic Magnetic Navigation
RMS	Root Mean Square
RoR	Rotate on Retract
RSA	Right Subclavain Artery
STD	Standard Deviation
TAVI	Transcatheter Aortic Valve Implantation
TCT	Task Completion Time
VCFM	Visual Contact Force Monitoring
VIF	Vascular Insertion Force

Chapter 1

Introduction

1.1 Cardiovascular Intervention Procedures

Cardiovascular intervention has been embraced as the standard minimally invasive treatment with significant benefits over invasive open surgeries. Smaller incisions, shorter periods of recovery, pain reduction, safe procedures for high-risk patients, lower infection, less hospital time and less bleeding are some of advantages of minimally invasive percutaneous interventions. Charles Dotter performed the first therapeutic procedure of revascularization with stenting and the first vascular stent in 1960 [13] in dogs. The first human angioplasty was in 1977 by A Gruentzig. Since then, cardiovascular interventions are extended to different treatments and procedures, e.g., vascular stenting, balloon angioplasty, cardiac arrhythmia ablation, valve replacement, chronic-total occlusion treatment, atherectomy and aneurysm repair, etc. Catheter and guidewires are the primary tools to deliver a treatment or to perform diagnosis in intervention procedures. Catheters are thin, long and flexible tubes that are advanced through a small port of entry in the humans cardiovascular system and are equipped with a stent, balloon, sensor, electrode, and other features for a specific diagnosis or treatment task [13, 14]. Guidewires are solid round wires with a complex and

composite structure which offer steerability, torquability and deliverability to attain the path in anatomy where catheters follow. Cardiovascular intervention procedures are performed under visual image guidance by navigating guidewires and catheters through arteries and veins to pass bifurcations and to reach a target point. The operator performs tool manipulation tasks, i.e., insertion, retraction and rotation, under visual guidance while sensing haptic cues of forces and torques at the proximal end. Cardiovascular devices are mainly visible in fluoroscopy imaging and clinicians can visualize anatomy through injection contrast agent. Navigation steps and tool-tissue interaction behaviour highly depends on operator experiences, understanding of cardiovascular anatomy and the device mechanical property and function.

Atherosclerosis is the most common vascular disease which refers to fatty deposits build up in the artery wall and results in calcification and plaque. This limits the flow of oxygen-rich blood to the down stream organs. The main treatment of atherosclerosis is angioplasty, an intervention techniques, which is performed through opening the narrowed arteries to restore the blood flow. The narrowing of coronary arteries can develop to a complete blockage and cause heart attacks. Plaque can form in the peripheral arteries causing Peripheral vascular disease (PVD), which can lead to distal ischemia and tissue death. Plaque can develop to chronic-total-occlusion (a severe PAD) and, if not treated, may result in lower limb amputation. The catheters/guidewires are advanced to cross the lesion and recanalize the vessel by inflating a balloon and/or placing a metallic stent [15]. Cardiac arrhythmia is another common heart disease treated by a cardiovascular intervention procedure known as ablation therapy. Cardiac arrhythmia might lead to clot formation, fainting, and sudden death [16]. The electrophysiology catheter is steered into the heart chamber to map its electrical activity and diagnose the source of abnormal heart rhythm. Then, an ablation catheter delivers a small lesion to near the pulmonary vein ostia in the atrium tissue, which disrupt or eliminate the erratic electrical signals.

As with any medical procedure, cardiovascular interventions are associated with certain complications and limitations. The risk of injuries from catheter/guidewire interaction with vessels is still high, which may cause complications such as perforation, dissection, and embolization. Moreover, there is complexity in controlling and navigating cardiovascular tools with limited maneuverability from the proximal end. The lack of force detection, intraluminal information, and restricted 3D imaging add difficulties and make tasks even more complicated especially for novice operators. Procedures can be more challenging in the lesions with torturous and diseased vessels. Other complications that may occur include bleeding from the insertion site, chest pain, and increased risk of kidney damage due to injected dye contrast. Secondly there are a number of occupational health problems for interventional cardiologists. High X-Ray exposure causes disease concerns such as cataracts, cancers and brain tumor [17, 18]. Heavy leaded apron worn to minimize radiation can cause orthopedic problems (spine, hips, knees, and ankles) and high workload in a standing position [18].

Robotic Cardiovascular Interventions are developed mainly to keep clinicians away from radiation exposure and enhance tools maneuverability. In a robotic-assisted intervention, the physician can remotely manipulate and control the intervention device from a shielded workstation, thus almost no radiation exposure affect the operator. Robotic systems are successfully tested in several intervention procedures for cardiovascular treatments [6, 19–22]. Despite the benefits of robotic systems for the clinicians, the treatment success rates are still comparable to conventional manipulations and clear clinical advantages still need to be shown. Other factors also limit the widespread integration of robotic technologies in endovascular intervention, including the cost of proprietary devices, longer preparation time, installation of the system in the existing cath lab, a significant learning curve and changes in the handling of instruments. The next sections provide a review of the commercial robotic

systems as well as emerging research in robotic intervention. The benefits, limitations and potential improvements of robotic-assisted interventions, tool-tissue interaction, contact force sensing and control solutions are also discussed.

1.2 Robotic Platforms for Cardiovascular Interventions

The robotic systems developed for cardiovascular interventions are designed based on targeted therapy and devices. Current robotic-assisted intervention platforms are developed for treatment in percutaneous coronary intervention (PCI), peripheral vascular intervention (PVI), and electrophysiologic intervention (EPI). All these robotic systems employs joysticks, buttons or haptic interfaces on the master side to transfer operator commands to the slave part, i.e., the robotic drive. The following is a review of commercial robotic platforms categorized based on the application for electrophysiology therapies and vascular intervention.

1.2.1 Commercial Robotic Platform for Electrophysiology and Cardiac Ablation Therapies

The **Sensei®** robotic system by Hansen Medical (Auris Health, Redwood City, CA, USA)) is a robotic platform developed for electrophysiology therapies with application in ablation and cardiac mapping. The system employs a steerable catheter built on two pull-wire driven components, including an inner leader within a coaxial outer sheath where the actuation of eight independent tendons control the distal deflection and tip orientation. This catheter, Artisan®, delivers flexibility and stability to reach hard-to-access areas of the heart and provides contact force sensing through an instrumented pressure sensor. A haptic interface, IntelliSense® Fine Force Technology,

is also integrated within the Sensei® system to provide contact force haptic feedback as well as a visual display of forces. The applied tip contact force could positively affect ablation efficiency and lesion size. The operator uses a 3D joystick and control buttons to steer the distal tip deflection and navigate the motion. The 3D electroanatomic mapping (EAM) is integrated into this platform as the CoHesion™ 3D visualization module. The clinical report proves the effectiveness and feasibility of this remotely electrophysiology robotic system [23–25]. The Magellan system was introduced for peripheral endovascular intervention based on the Sensei® design.

The **Niobe®** Robotic Magnetic Navigation System (Stereotaxis, Inc., St. Louis, MO) [1] offers manipulating and steering of the electrophysiology catheter tip using a magnetic field generated by two permanent magnets next to the patient's body. The control of the distal deflection and tip position is achieved by using magnetic force by changing the relative orientation of robotically-controlled magnets. The physician uses an intuitive computer interface to adjust the magnetic field and precisely direct and steer the catheter's distal end. This system has been successfully used for mapping and ablation in clinical settings [21, 22, 26]. The Vdrive Robotic Navigation System is integrated with the Niobe® system, which allows remote robotic control of third party diagnostic devices with precise movements. The integrated system provides robotic navigation and stability for both diagnostic and ablation devices. The system's main limitations are the difficulties in implementing magnets in existing EP labs and longer procedure times compared to manual operation [26, 27]. **Genesis** is the new generation of the Robotic Magnetic Navigation (RMN) system based on the Niobe design with an architecture that is smaller, lighter, faster, and more flexible.

The **Catheter Guidance Control and Imaging (CGCI)** system (Magnetecs Inc., CA, USA) is another magnetic-based robotic navigation platform similar to Stereotaxis devices. The system is composed of eight electromagnets in a semi-spherical pattern, which can generate a variable magnetic field. The control on

the magnetic field allows steering of the magnetic catheter and rotation along its longitudinal axis.

The **Amigo™** Robotic System (Catheter Precision, Inc., Mount Olive, NJ, USA) offers remote control of standard EP catheter through replicating operator manipulation on an intuitive remote controller. The mechanism is build based on manually operating on EP catheters and allows for the user to remotely advance, retract, rotate and deflect the tip of an attached standard mapping or ablation catheter. The controller resembles a traditional catheter handle to minimize the operators learning curve and system preparation. A reduction of radiation exposure during procedures, a smooth integration with EP lab, and simple installation are reported as advantageous of this system [28].

Fig. 1 shows samples of commercially available EP robotic platforms. Although the current EP robotic catheterization platforms decreased the clinical radiation exposure and increased dexterity of catheter motion, no significant reduction in patient radiation exposure and procedure time was reported. Additionally, no commercial system is equipped with automation features to compensate heart motion and maintain catheter-tissue contact to improve ablation therapy. Since the manual control of the steerable section of catheters in the heart chamber is challenging and skill-dependent, automated and semi-automated robotic solutions have been proposed in the research domain. Automated control has a significant potential to enhance ablation therapy performance and improve patient care.

(a)

(b)

Figure 1: (a) Stereotaxis Robotic Magnetic solution including Genesis Robotic Magnetic Navigation (RMN), catheter Vdrive and Stereotaxis imaging [1], (b) Amigo^{TM} Remote Catheter System with an ergonomic hand-held controller [2].

1.2.2 Commercial Vascular Robotic Platforms

The **Corpath® system** (Corindus Vascular Robotics, MA, USA) is the first commercial endovascular robotic-assisted intervention platform for PCI and PVI. Corpath® 200 is the first generation of vascular robotics specifically designed for PCI. Corpath® *GRX* is the second generation build based on the Corpath® 200 clinical success which expands the application to PVI and neurovascular interventions. The robotic

intervention system allows the clinician to sit in a radiation-protected workstation and control the device movement using a joystick and touchscreen with submillimeter robotic precision. The Robotic drive holds a single-use cassette placed beside the patient and enables pull/push and rotation of guidewire and catheter. The The Corpath® system benefits from being compatible with off-the-shelf navigation as well as therapeutic devices including balloon/stent catheters and laser atherectomy catheters. The use of robots is not limited to navigation procedures but covers crossing lesions and treatments. Clinical reports showed the efficiency and safety of this robotic system as there is no report of perforation, injury or death. In nearly all of the cases, the procedure ended successfully [20]. Other studies using the system have shown 99.1% clinical success in complex coronary lesion cases [29], a 95% reduction in radiation exposure of the primary operator [20] and a 20% exposure reduction for the patient compared to manual operation [30]. The accurate measurement of the anatomy with the robotic system demonstrated a 8.3% reduction in stent usage as well [31]. A set of basic automated movements has been recently added to the Corpath® *GRX* system called *technIQ*^{TM} *Smart Procedural Automation* [12]. The automation features are built based on highly skilled operator techniques and aim to standardize treatment protocols, increase efficacy, and improve patient care. Table 1 explains these automated robotic movements set. Corpath® shares no force measurements or haptic feedback.

Table 1: Automated robotic movements set integrated in *technIQ^{TM} Smart Procedural Automation* of Corpath® Vascular Robotic Platform [12].

Automated movement	Guidewire drive	Device drive	Advantages
Rotate on Retract (RoR)	✓	✗	Rotates GW in retraction to reduce navigation time in difficult anatomy
Wiggle	✓	✗	Oscillates GW to aid advancement and prevent prolapses in tortuous vessel
Spin	✓	✗	Rotation of GW to efficiently cross lesions in complex cases and difficult anatomy
Dotter	✗	✓	Rapid back-and-forth motion to ease crossing in narrow and calcified lesions
Constant speed	✓	✓	Enables precise measurements

The **Magellan™ System** is another robotic platform developed by Hansen Medical for peripheral vascular intervention. The system utilizes its own steerable catheter, which offers higher controllability for navigation, and allows simultaneous control of a commercially available guidewire. Simultaneous control of the guidewire and catheter is a key factor in endovascular catheterization as physicians used to manual procedures are trained in this way. The Magellan™ robotic catheter is made of tendon-derived inner leader and an outer sheath and the deflections are controlled by the operator using a 3D joystick or navigation buttons at the master workstation. Although the robotic catheter allows the ability to access more challenging vessels, the system cannot be used with therapeutic devices that limit usability in performing navigation only. The other limitation is the high cost of the robotic catheter, as well as installation and preparation. The system was successfully tested for endovascular aneurysm repair and stent grafting [19], as well as other treatments including iliac and femoral artery lesions [6] and uterine artery embolization [32]. The Magellan™ system, similar to Corpath®, does not incorporate tactile or force feedback in the

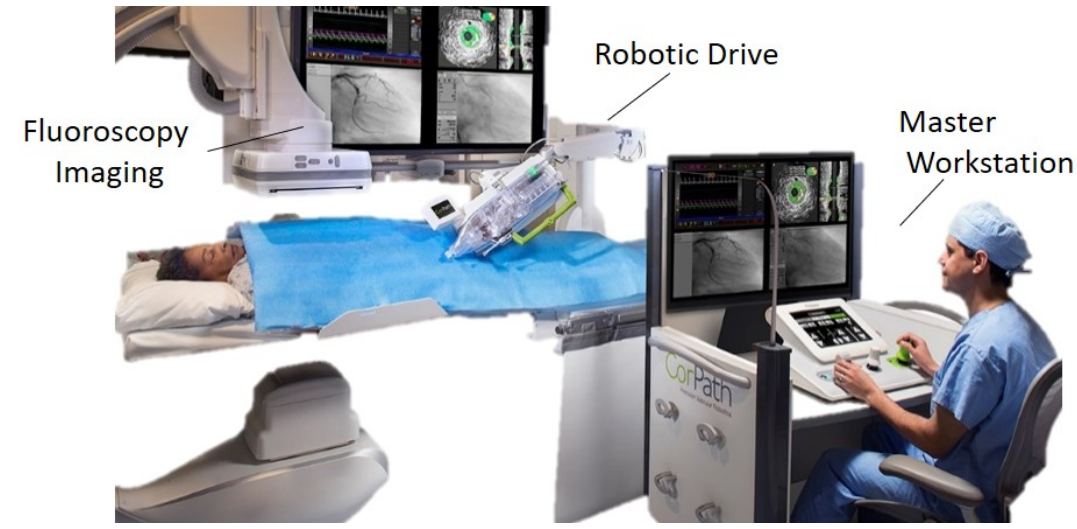

(a)

(b)

(c)

Figure 2: (a) Corpath® *GRX* vascular robotic system for PCI and PVI [3, 4], (b & c) Hansen Medical Magellan robotic catheter system for endovascular interventions [5, 6].

master workstation.

The **R-One™** (Robocath, Rouen, France) is another robotic vascular platform introduced for PCI. It is compatible with market-leading devices and cath labs, and also features robotic manipulation of guidewire and catheter. The system benefits from reproducing hand movement by independent or simultaneous rotation and translation of guidewire and catheter, separately controlled by joysticks. The system recently received the CE mark and completed its first robotic coronary angioplasties in Europe. Fig. 2 presents examples of the workstations and slave manipulators of vascular

robotic platforms. Current robotic vascular systems offer benefits and limitations compared to conventional manual intervention, as summarized in Table 2. Remote-controlled systems move the operator from the proximity of fluoroscopy imaging to a radiation-protected workstation, significantly reducing the radiation exposure for clinicians and associated health concerns, i.e., cataracts, cancers and brain tumor. In addition, the operator remains on the workstation with added comfort without the orthopedic risks and fatigue of heavy protection suits. Robotic systems have the potential to reduce exposure to the patient by improving the efficiency and speed of procedures. A more dexterous device motion with improved stability and precision is also achieved using a robotic drive compared to manual manipulation. High-resolution measurement of the anatomy, the accurate placing of stents, and enhanced visibility are also points in favor of robotic-assisted intervention. Conventional intervention may need several trials for complex task completion while robotic steerable catheters ease the navigation. However, only the simplicity in steering may not justify the robotic system cost, the modification required in the cath lab and more preparation time. Moreover, most systems employ non-ergonomic master interfaces (mostly joysticks and buttons), which change the natural device manipulation. The operator also loses the real tactile and haptic sense of manual manipulations and must adapt to a robotic haptic device if such a system is provided. Removing the tool from the hands of the interventionist and exploiting a new device for manipulation may require a longer training. Also, the clinicians may not be able to use their skills and experience in the same way as in manual procedures. Robotic systems working with conventional passive devices (like Corpath® and R-one™) add no significant dexterity compared to manual manipulation, in which the benefit of systems for patient care still needs to be clarified. Although the robotic endovascular platforms brought meaningful benefits to clinicians, the success rate, procedure time and the contrast agent does are comparable to manual manipulation. MR imaging is an alternative solution for fluoroscopy but

there are limited MRI compatibles devices and none of the current robotic systems are adapted for MR imaging capability.

Table 2: Benefits and limitations of robotic-assisted intervention compared to conventional manual intervention.

	Robotic Assisted Intervention	Conventional Intervention
Benefits		
Clinicians radiation exposure	Exposure safe workstation	High X-ray exposure
Patient radiation exposure	Potential reduction	Operator skill dependent
Steering and navigation	Stable and precise motion	Manual manipulation
Deploy stent/ballon	Locked holding in place	Devices loose during inflation
Stent placing	High resolution motion	Manual adjustment
Anatomy measurement	High resolution measurement	Visual estimation
Visual guidance	Close proximity, ergonomic visualization	Struggle to see angiography
Tortuous anatomy access	Higher dexterity, controllability	Challenging, skill dependent
Orthopedic strain, fatigue	Comfortable seated workstation	Significant with high health hazard
Complex lesion crossing	Stable control, potential automated features	challenging, skill dependent
Workload	Less stress, physical and cognitive load	High workload, standing condition
Tip contact force control	Potentially safe, autonomous	Visually estimated, risky
Limitations		
Interface learning curve	Need training, system dependent	No extra training
Haptic and tactile feedback	Robotic interface	Real sense
Integration	Need adaptation and preparation	No modification
Tool compatibility	Limited to compatible devices	No limitation

1.2.3 Emerging Research in Robotic Cardiovascular Intervention

Several studies looked into developing and improving robotic endovascular systems to leverage the procedures safety and efficacy. The focus of these studies was on different aspects of robotic platform including instruments, robotic driver, master interface, control methods and tool interaction modeling. Robotic units are mainly designed based on wheel-derived mechanisms and linear drivers with spring or actuated clamps [9, 33–39]. Manual control of teleoperation for under-actuated guidewires/catheters is not predictable and requires trial and error to attain the desired target in the anatomy. The concept of automatic or semi-automatic insertion are promoted in several studies for more efficient manipulation procedure with less tool-tissue interactions [36, 40–43]. A study successfully tested an autonomous catheter insertion system based on path reconstruction within a humanoid major vascular phantom [43]. This work was done by controlling the catheters tip to reach to a targeted point using a magnetic motion sensor. The proposed system was able to pass the catheter into the targeted bifurcations and retract it from a wrong branch. However, there was no control on the amplitude of tip rotation; that was not addressed in this study. Jayender et al. proposed autonomous navigation based on visual tracking of an active steerable catheter equipped with a shape memory alloy actuation at the distal tip [40–42]. A fuzzy PID control algorithm with guidewire force feedback was developed to increase surgical safety, decrease overshoot and precisely position the guidewire by scheduling controller strategies [44]. Some recent studies focused on learning-based automated catheterization with different algorithms including learning-from-demonstration, reinforcement learning, and imitation learning [36, 45–48]. The expert maneuver motions were observed and incorporated into a model to assist novice operators in a semi-autonomous robotic collaborative platform. Proposed learning-based methods achieved autonomous task planning, safer tool-tissue interaction and reduced movement and contact force.

Developing an ergonomic master interface and integrating haptic feedback were proposed by some researchers. Takur et al. [9] developed a master-slave catheter system with the idea of manipulating a real catheter in the master side to read the feedback and replicate the same motion on the slave robot (Fig. 3 (e)). Ergonomic master controllers are more intuitive to use and provide a platform for clinicians to leverage their skills and experience gained in the traditional procedure. Researchers also utilized other ergonomic master manipulator designs for mimicking natural skills [7, 33, 37, 49–51]. Dagnino et al. [7] proposed an ergonomic master-slave system with integrated vision-based haptic feedback through active dynamic constraints (Fig. 3 (a) and (b)). Srimathveeravalli et al. [52] evaluated the manipulation motion and force at the hand of the operator to propose a robotic system and render haptic feedback. Thorsten et al. [53] presented a palpation system for angioplasty to replicate the distal tip force of the guidewire to the proximal end in the hand of operator, which helps to complete the procedure faster with a feel on size, length and level of blockage. A master-slave tele-neurosurgery system integrated with haptic display and force sensors was developed and successfully tested by Taminoto et al. [54]. In this work, both proximal end and distal catheter insertion tip forces were measured and the proposed haptic system was able to display either distal or total proximal forces or a combination of both on the surgeon's hand. This feature is specifically valuable as the surgeon can distinguish friction forces and distal tip contact force.

Ganji et al. proposed a model-based control for semi-automatic tele-navigation of catheters inside the cardiac chamber to reach a targeted point (Fig. 3 (f) and (g)) [10, 55]. The catheter distal shaft was modeled as a planar continuum robot with rigid links and joints, in which the position of the catheter tip was found through the forward kinematic calculation. A 3DOF robotic platform for traditional electrophysiology catheter was proposed by Park et al. [35] to remotely control the insertion process. In this study, the cardiac ablation catheter motion was controlled in forward/backward,

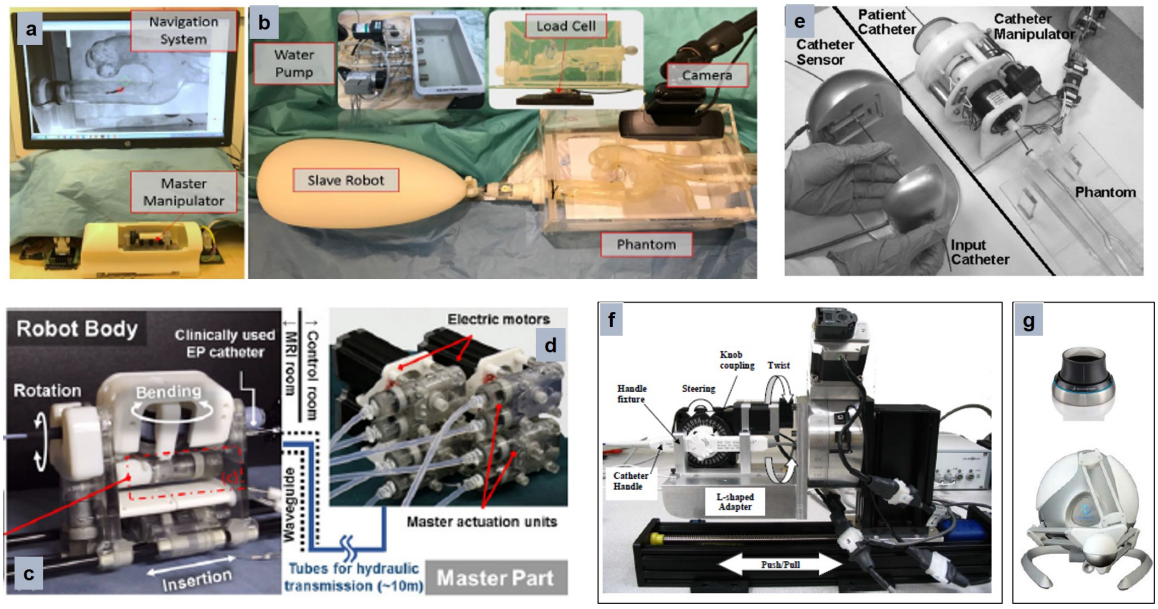

Figure 3: Robotic cardiovascular systems developed in research studies: (a) and (b) ergonomic robotic endovascular catheterization with vision-based feedback by Dagnino et al. ©2018 IEEE [7]; (c) and (d) a MR safe intracardiac EP robotic manipulator by Lee et al. ©2018 IEEE [8]; (e) master-slave catheterization system by Takur et al. ©2009 IEEE [9]; (f) and (g) intracardiac robotic-assisted navigation with master haptic device by Ganji et al. [10].

twisting and bending. The manipulation forces were measured by a sensor or estimated from motor current and then displayed on a haptic device. Lee et al. [8] presented an MR safe robotic for intracardiac EP intervention via hydraulic actuation (Fig. 3 (c) and (d)).

1.3 Contact Force Sensing and Tool-tissue Interaction

1.3.1 Clinical Challenges and Complications

Endovascular tool interaction with the vessel wall is inevitable as the navigation relies on wall interactions. Clinical studies reported vascular injuries including perforation, dissection, and rupture due to catheter/guidewire interaction with the arterial wall

[11, 56]. Wall injuries are more concerning in steering and navigating within tortuous arteries and crossing through the complete blockage known as chronic-total-occlusion (CTO). CTO devices are designed with a stiffer tip to satisfy crossing performance. Clinicians apply high proximal force on CTO wires and catheters to cross highly calcified lesions that critically raises complications likelihood, especially perforation and dissection [57, 58]. Studies have pointed out other complications such as intraprocedural risks of embolization, ischaemic brain lesions and stroke [59, 60]. Nearly 50% of cases treated with carotid stenting have reported a new ischaemic lesion in the post-treatment scan with diffusion-weighted imaging (DWI) [60]. Doppler monitoring has also shown a significant number of microemboli in carotid cannulation and stenting in both ipsilateral and the contralateral carotid territories [61–64]. The risk of embolization is also high in other cardiovascular treatment with percutaneous interventions such as transfemoral aortic valve replacement (TAVI) and thoracic endovascular aortic repair (TEVAR) [65–67]. These findings suggest that intraluminal tool interaction forces stand as a determinant factor for procedure safety and efficacy. The complications connected to tool-tissue interaction highlight the importance of manipulation techniques. Despite the importance of tool-tissue interaction, information on intraluminal contact forces is highly limited in both measurement and control methods. The tip load of guidewires as the downward force causing wire buckling may present the maximum range of safe contact point force on the vasculature. The tip load of off-the-shelf guidewires are 0-12 g for coronary wires and 0-40 g for peripheral wires.

In the cardiac ablation procedure, a specific amount of radiofrequency energy is transmitted to the tip in order to ablate a part of heart tissue which is the source of arrhythmia. Beside RF power and period, the angle of the catheter tip, magnitude, and direction of contact force affect the lesion formation and consequently the therapy efficiency. Suboptimal catheter tip contact force during lesion delivery

results in insufficient treatment and overloading that can damage or perforate the tissue. Clinical studies reported enhanced efficacy of ablation of paroxysmal atrial fibrillation (AF) using catheters with CF sensor integrated at the tip [68–70]. Contact forces of $10\,g$ to $30\,g$ in the tip of intracardiac catheters were reported preserving safety and achieving uninterrupted transmural lesions [71–73].

1.3.2 Instrumented Cardiovascular Devices with Embedded Sensors

Commercially available RF ablation catheters are instrumented with tip force sensors that can report tip angle and magnitude and the direction of the tip contact force. Examples of instrumented ablation catheters are Artisan Extend Control Catheter (Hansen Medical, MountainView, CA), Thermocool SMARTTOUCH Catheter (BiosenseWebster, Diamond Bar, CA) [69] and the Tacticath ™ Quartz ablation catheter (Abbott, Chicago, Illinois, USA) [74]. The Artisan Extend Control Catheter is integrated within the Sensei robotic platform in which force measurements are delivered by haptic feedback and displayed on a visual module.

Several studies investigated embedding different types of sensing elements at the catheter tip, mainly for the application in cardiac ablation. Piezoelectric, piezoresistive and strain-gauge sensors are utilized to measure static or dynamic forces with superior resolution and bandwidth needed for tool-tissue contact monitoring [35, 38, 54, 75–77]. Despite the promising results of such sensing elements, the integrity in cardiac catheter is challenging due to impact on the force measurement accuracy from nearby ferrous materials. Fiber optic-based sensors are developed and proven as a viable measurement solution [78]. Fiber optic sensors are integrated for contact force measurement at the tip of ablation catheters [79–82] and incorporated adequately in robotic platforms with haptic or visual force feedback. Polygerinos and Su designed cardiac catheters with MRI-compatible fiber optic sensors [83–85]. The performance of such devices

were confirmed with bench and *in-vivo* studies.

The complexity and cost of integrating force sensors are among the main reasons limiting clinical use of sensorized cardiac catheters. Other issues and restrictions include electrode spacing, influence of temperature for stable contact force measurement, interference with nearby devices (braiding of sheath, nearby circular mapping catheters) and reduced maneuverability of the distal shaft.

1.3.3 Model based Force Sensing Solutions

Indirect force-sensing methods provide an alternative solution to instrumented tools. Computational and numerical models are capable of estimating contact forces. Kinematic models of catheters have been reported in several studies with the goal of simulating the behavior of catheters/guidewires. Camarillo et al. [86] proposed a kinematic model for steerable catheters which was used for modeling the catheters in free space with tendon actuation and without contact force. Khoshnam et al. [87–90] studied the modeling and control of ablation catheter contact force based on shape analysis. They studied the effect of force in changing the shape and mapped the shape and deflection into a force estimation model. In another study, the range of contact force was estimated using a curvature catheter index and kinematic model. Rucker et al. [91] proposed probabilistic based tip pose measurements for force sensing of continuum robots which can be extended to catheters as well. In this method, high computational cost of an Extended Kalman Filter is a challenge for online force monitoring. Simaan et al. [92] studied force estimation in the general form of continuum robots. Back et al.[93] utilized a real-time Cosserat rod to model tendon driven ablation catheter and estimated tip contact force using shape detection. They also achieved force estimation and steering goals using a kinematic model of cardiac catheters. Hasanzadeh et al. [94, 95] developed online external force estimation based on the planar elastic model assuming quasi-static deformation. They extended their

work to 3D by coupling the classical cosserat rod model with a new model of the pull-wire actuation. The cosserat rod model has been implemented by Soltani et al. [96] for shape-based three-axial force and stiffness estimation as well. Contact modeling of catheter-vessel interaction in virtual reality with applications in training simulators was investigated in several studies based on methods including FEM, multi-rigid and multibody dynamics, differential geometry, continuum mechanics and cosserat rod [97–101, 101]. To the best of the author's knowledge, there is currently no force sensing solution for multiple contact forces through the entire length of the tool interacting with the vessel wall.

1.3.4 Force Control in Cardiovascular Intervention Procedures

Studies that aimed to control cardiovascular devices are two-fold: 1. contact force control on the tip of cardiac catheters, 2. proximal insertion force control in general endovascular navigation. The works related to cardiac catheter tip CF control are more extensive compared to insertion force control studies. Khoshnam et al. proposed several control strategies in model-based methods, black-box and optimal control methods to keep the contact forces safe using image-based force-sensing [90, 102]. Kenser et al. developed a cardiac catheter tip control method based on active motion compensation of heart beating to keep stable and consistent contact [103, 104]. Their method uses 3D ultrasound image guidance and force control to enable constant contact on a moving target surface. A position loop force control approach was investigated to achieve the desired force by adjusting the position trajectory [105]. They also improved force tracking using a friction and backlash compensation method.

Gelman et al. designed a handheld contact force controller device for commercial catheters [106]. Their system employs a tip sensing force feedback and closed-loop force controller with proximal velocity actuation. The proposed controller delivered

stable force control on a 1-DOF myocardial tissue motion simulator. Jayender [107] studies the control of insertion force of a catheter using hybrid impedance control. Their proposed method was implemented on 7-DoF redundant robot to perform simultaneous force/position control using proximal force feedback. This work aimed for safer catheter navigation based on insertion force sensing. However, force in the proximal end is mixed with considerable friction of devices with sheath, support catheters and other instruments. The relation between insertion force and intraluminal contact force has not been investigated.

There is a gap in the literature for measuring and estimating multiple point loads and intraluminal wall contact forces occurring during general endovascular interventions, e.g., PCI, PVI, and vascular navigation. To the best of our knowledge, there has not been an attempt to control or to limit the catheter's multiple contact forces with the vessel wall through the length of the interactions. There is still a lack of sensing technologies that can measure all intraluminal interaction forces to provide controller force feedback.

1.4 Scope and Objectives

The main objective of this research is to provide a framework to enhance the safety of tool-tissue interactions in endovascular robotic intervention procedures with a focus on a general form of vascular navigation using non-steerable catheters and guidewires. To do so, an image-based framework is proposed to estimate, monitor and control intraluminal contact forces of an endovascular tool in interaction with the vessel wall.

The contact force estimation is achieved by building a numerical finite element model of the tool via image-based data extraction. In this approach, the image processing algorithms enable real-time tracking of contacts, tool body shape, and deflections, providing the required data for creating the tool model and updating

its boundary conditions. The FEM model also requires prior information of tool mechanical properties, i.e., bending rigidity distribution over its length. Tool flexural properties can be measured through bending tests or can be provided by the medical tool manufacturer. The generated FEM model computes the external forces applied to the vessel wall at the contact points. The proposed sensor-less force estimation approach can be implemented in the current practice of both conventional and robotic-assisted intervention procedures. We have implemented the method to an ICF monitoring during aortic artery cannulation in an anthropomorphic phantom using a teleoperated robotic system. The 2DOF robotic drive is proposed based on the methods in conventional manual navigation to allow simultaneous and independent control on insertion and rotation. Master is able to remotely control the navigation while observing the maximal magnitude of ICF on the screen to avoid overloading on the arterial wall. All ICF data during navigation can be mapped on the arterial wall to study the place and severity of high-risk interaction. Furthermore, the contour map of ICF help operators to assess, understand, and improve their manipulation maneuvers. Intraluminal modeling also provides insights into the tool's mechanical performance in structural design and stress analysis. This research provides an experimental platform to evaluate local intraluminal force compared to the total force exerted on the vascular phantom to demonstrate the importance of intravascular measurements.

Another objective of this research is to develop a semi-automated robotic vascular navigation framework that maintains ICFs in a limited range through the entire interactions. The proposed ICF monitoring data provides force feedback for automation and control methods. A velocity-actuated contact force control loop can perform regulated insertion that reacts fast to the sudden ICF changes and makes the procedure smoother. Based on tip visual tracking, an automated retraction-reinsertion feature eases the excessive deflection and friction force buildup to advance the insertion procedure. The use of ICF data in both forms of automated control and visual

monitoring reduces the risk of vascular complications.

The scope of this research can be extended to the off-the-shelf catheters and guidewires in the current practice of both conventional and robotic-assisted intervention procedures. By leveraging available imaging in endovascular intervention, the intraluminal tool-tissue interaction information can be given to the operator as intra-operative visual guidance to enhance navigation safety and can be used as force feedback for the next generation of automated robotic interventions. We anticipate that such automated robotic features may raise safety to a level that a human cannot achieve. Human-robot shared control has the potential to standardize the procedures, decrease the user workload of top skilled operators and compensate for the limited skillset of novice operators.

1.5 Contributions of the Author

This thesis contains the material of three papers. The first paper, titled "A Sensor-less Catheter Contact Force Estimation Approach in Endovascular Intervention Procedures", was published in *2018 IEEE/RSJ International Conference on Intelligent Robots and Systems (IROS)*. The second paper entitled "Image-based Intraluminal Contact Force Monitoring in Robotic Vascular Navigation" has been submitted to *IEEE Transactions on Medical Robotics and Bionics* which is currently under review. The third manuscript, "Automated Endovascular Insertion Limiting Intraluminal Contact Force via Image-based Control", has been submitted to *International Journal of Computer Assisted Radiology and Surgery*.

A summery of key contributions of this thesis is as follow:

Chapter 2: **A sensor-less catheter contact force estimation approach in endovascular intervention procedures**

A model-based force-sensing method for multiple contact points at the side of

endovascular tools, i.e., a general form of non-steerable catheters or guidewires, is developed using image data. The endovascular tool is modeled as a cantilever using finite element method based on a nonlinear beam element. Image segmentation algorithms are developed to extract the tool shape, detect contact, and compute deflections and pose measurements. Estimating several point forces along the endovascular tool is achieved by simulating the deflected tool based on data extracted from image feedback. The effectiveness and accuracy of force estimations are experimentally investigated by comparing to the real sensor measurements in scenarios with random deflection and different numbers of contact point forces. The proposed method has low computational cost, is accurate and easy to implement to the off-the-shelf catheters and guidewires without making any changes in the structure or embedded sensors.

Chapter 3: **Image-based intraluminal contact force monitoring in robotic vascular navigation**

This work's main contribution is in developing intraluminal interaction force monitoring in navigation within a realistic cardiovascular phantom in a teleoperated robotic platform. The other contribution is in a comparative study between intraluminal CF and force exerted on phantom to highlight the necessity of local tool-tissue monitoring for safe procedure. It also presents intraprocedural stress analysis of the tool. The robotic system is designed and fabricated based on the methods in conventional manual navigation to allow simultaneous control of insertion and rotation. Proposed mechanism has a wheel-drive translation unit assembled on a rotational gear drive unit. Real-time detection and tracking of contacts on the phantom vascular wall have been accomplished. The numerical model is updated to consider shear deformation. Multipoint ICF monitoring has been achieved during aortic artery cannulations and the procedure force contour is obtained on the arterial wall. The proposed method does not require information about contact interaction conditions, friction, and vessel tissue properties.

Chapter 4: **Automated endovascular insertion limiting intraluminal contact force via image-based control**

This work presents a semi-automated robotic framework that limits tool-tissue contact forces through the entire length of the interaction with the vessel wall while advancing the navigation procedure. An intraluminal force control based insertion is developed to perform smooth catheterization based on the changes in interaction force. Tip visual servoing is proposed to autonomously retract the tip and retry insertion once the gradual build-up of deflections is fully relaxed. This work uses visual force sensing and visual tool tracking techniques described in Chapters 2 and 3 as the controller's feedback. The collaborative semi-automated robotic navigation successfully maintained ICF under the prescribed limit, significantly reducing the risk of complications such as perforation and dissection, stroke, and brain lesion. Automated insertion framework performance is compared to the manually controlled teleoperation with ICF visual guidance and traditional teleoperation. The proposed framework outperforms manual manipulations qualitatively and quantitatively using metrics of force and motion. We also show that the intraluminal force monitoring system can guide the operator to avoid extreme CF peaks and enhance manipulation performance.

1.6 Organization of the Thesis

This thesis is presented in manuscript-based format based on the content of three papers. All chapters, excluding Chapters 1 and 5, are duplicated from the manuscript of papers published or submitted and under review process for publication in scientific journals or premier conferences.

The first chapter provides background information on cardiovascular interventions, commercial robotic platforms, and emerging research platform for cardiovascular

catheterization. This chapter also discusses the tool-tissue interaction complications and includes literature review on contact force sensing and control methods of cardiovascular tools. Chapter 2 presents the image-based contact force estimation concept and the experimental validation of the proposed method. Chapter 3 applies the proposed concept presented in Chapter 2 into an intraluminal contact force monitoring during robotic cannulation of aortic arteries. Chapter 3 also explains robotic systems design, presents a comparative force study, and elicits stress prediction. Chapter 4 focuses on an automated intraluminal CF control framework to limit tool-tissue interactions in the prescribed safe limit and compares the proposed method with manual teleoperation experimentally. The final chapter concludes the dissertation by summarizing the remarks and contributions, discussing the limitations and describing future research directions.

To comply with Concordia University thesis recommendations, the reference lists of all chapters are combined and presented at the end of the thesis. As such, the figures and tables layout may have been modified.

Chapter 2

A Sensor-less Catheter Contact Force Estimation Approach in Endovascular Intervention Procedures

Catheter/guidewire manipulation in endovascular intervention procedures are associated with risks of injury on vessel wall and embolization. Determination of catheter/guidewire-vessel interaction contact forces can improve the navigation process safety and efficiency which prevent injuries in both manual and robotic vascular interventions. This study proposes a sensor-less sensing solution to estimate multiple contact point forces at the side of catheter/guidewire exerted on the vasculature. This goal is achieved by using image feedback of catheter-vessel interaction and numerical finite element modeling (FEM). Real-time image processing algorithms are implemented to track interaction contact points on catheter/guidewire. Image-based deflection measurement and contact points tracking data are given to a nonlinear finite element beam model to estimate the forces. The variable equivalent bending

modulus of the guidewire is found through a series of three-point-bending tests. To directly measure contact point forces, an experimental platform is prepared which simulates catheter/guidewire-vessel interaction with two, three and four contact points. The effectiveness of the proposed approach is tested in six scenarios in which force estimation accuracy of more than 87.9% is achieved. The proposed approach can be applied to various types of under-actuated catheter/guidewire in endovascular intervention procedures. This study shows that multiple catheter/guidewire side contact forces can be estimated by using the deflected shape and equivalent bending modulus property without embedding any force sensor.

2.1 Introduction

Endovascular interventions are performed by manipulating catheters/guidewires through dexterous vascular human anatomy. Operators mostly navigate under-actuated catheters and guidewires by a series of tasks consisting of inserting, retracting and rotating at proximal end. The excessive interaction forces between catheter/guidewire and vessel wall may cause complications such as damage to epithelial cells, embolization, thrombosis and dissection especially in the case of diseased and weakened blood vessels. The viable contact force information can be used to minimize risks of injury and help operators in navigation tasks. In ablation therapy, one important factor in operation efficiency is the magnitude and direction of catheter tip-heart tissue contact force. Some Radiofrequency (RF) ablating catheters are equipped with miniaturized force sensors at tip to report the magnitude and direction of single tip contact force such as Thermocool SMARTTOUCH Catheter (BiosenseWebster, Diamond Bar, CA) [108] and the Tacticath ablation catheter (St. Jude Medical Inc., St. Paul, MN) [109]. Catheters with fiber optic embedded sensor at the tip were fabricated in some studies and have been proven as a viable solution

[78, 79]. However, due to the noticeable cost of sensorized catheters, a number of studies focused on tip contact force estimation using image feedback and shape deflection analysis. Khoshnam et al. [89, 110] proposed an approach for ablation catheter tip force estimation by catheter shape analysis in free space and in case of contact with heart tissue. They applied a kinematic model and estimated the range of forces using a curvature catheter index. Simaan et al. [92] studied forces sensing in general form of continuum robots. Back et al. [93, 111] utilized a real-time Cosserat rod model to estimate tendon driven ablation catheter tip contact force and implemented a kinematic model for both force estimation and steering goals. The Planar elastic model of ablation catheter with quasi-static assumption has been given another solution for tip contact force estimation as studied by Hasanzadeh et al. [112]. Ginder et al. [113] implemented the finite element simulation on patient-specific guidewire insertion to predict guidewire and arterial deformation. Moreover, modeling methods like FEM, multi-rigid and Cosserat rod also used for simulation of cardiovascular intervention procedures [97–100, 114].

While most research have been carried out for tip contact force measurement/estimation of cardiac catheters, finding catheter body contact forces at the other areas of peripheral or cerebral vascular procedures is still a challenge. Some studies [41, 42] proposed controlling the proximal total force of catheter insertion that may make the navigation process safer and smoother. However, the total force of catheter insertion at the entry point is the sum of several contact forces and it is polluted because of friction with other vascular devices (e.g. introducer sheath, guiding catheter, etc) [115]. To prevent any injury on vasculature, the contact forces should be measured at each contact point through the entire length of interaction with vessels. Our study focuses on side contact point forces of conventional catheters/guidewires with no tendon driven actuation or embedded miniaturize sensor. These forces can be given to operator as intra-operative visual guidance to enhance the safety of navigation procedure and can be used as force

feedback for the future generation of cardiovascular intervention robotic systems.

In this study, we developed a new sensor-less contact force estimation principle for multiple contact points at the side of catheter/guidewire in interaction with the vessel wall. It is achieved using image-based contact points tracking and deflection computing parallel to a nonlinear beam finite element modeling of catheter/guidewire. A multi-contact point force measurement test setup is designed to measure catheter contact forces at each contact point directly. It physically simulates catheter-vessel interaction in different shapes and deflections. ABAQUS FEA commercial software has been used as the FEM solver which is fed with an imaged based catheter model. The planar catheter deflection is assumed to simplify experiments and reduce computational costs. Catheter segmentation and deflection measurement have been done through the imaging from an RGB camera. However, this concept can be applied to medical imaging environment e.g. X-Ray fluoroscopy, MRI and real-time Ultrasonic. Catheters/guidewires and vessel's shape extraction have been developed in several studies before [113, 116–118] which makes contact points tracking using 3D imaging data intra-operatively feasible. In the proposed approach, three-point-bending tests provide the equivalent bending modulus of catheter/guidewire. To the best of our knowledge, this is the first work that provides a sensor-less solution to estimate multiple contact point forces at the side of catheter in interaction with vessels. In the following manuscript catheter or guidewire refers to the same concept of meaning.

2.2 Sensor-less Contact Force Estimation and Experimental Setup

2.2.1 Sensor-less Contact Force Estimation Approach

As the catheter/guidewire is being inserted through the human cardiovascular system, it deflects because of interaction with the internal vessel wall. The combination of image processing and numerical solutions is used as a sensor-less catheter-tissue contact force method. The entire shape of the catheter has been tracked during the insertion procedure to locate catheter-vessel contact points and measure their deflections. Any part of the catheter that starts from a chosen point and ends in the catheter tip can be modeled as a cantilever beam.

Applying a set of boundary conditions in the FEM model equals to the deflections of contact points simulates the same condition of catheter deflection in the vessel. Fig. 4 shows the schematic view of catheter deflections in contact points with respect to its undeflected intrinsic shape. The undeformed model can be constructed as a cantilever beam tangent to the catheter at any desired point. The position of contact point i is CP_i with the length L_i, which is measured along the catheter shape. For each CP_i, its corresponding point with the same length on the undeformed model is the boundary condition BC_i. Parameter d_i is the deflection which should be applied in boundary condition i as the difference between CP_i and BC_i (see (1)). FEM model computes the reaction forces, F_i, at boundary condition, CP_i which is an estimation for the catheter-vessel contact forces. The contact forces (CFs) can be broken into components of normal (f_n) and tangential/frictional forces (f_t) on catheter. The vessel wall mechanical properties and catheter-vessel frictional coefficient data are not needed in this method. Base point for cantilever should be selected in a way to include all targeted contact points.

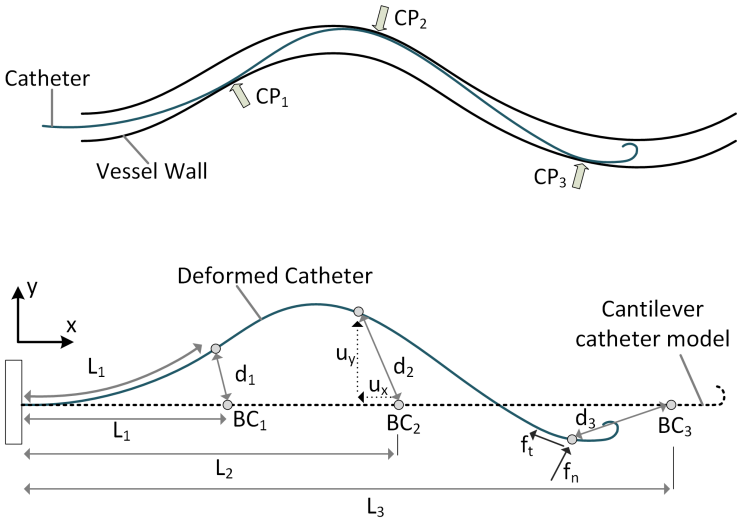

Figure 4: Force estimation concept using FEM model: CP_i is the contact point, L_i is the length of contact point on the catheter, BC_i is boundary condition points on catheter model which is the corresponding point for CP_i, d_i is the deflection of contact points, u_x and u_y are the components of deflection with respect to coordinate of cantilever.

$$d_i(u_x, u_y) = (X_{CP_i} - X_{BC_i}, Y_{CP_i} - Y_{BC_i}) \tag{1}$$

The quasi-static FEM model can be solved in real-time to estimate the contact forces as the catheter moves inside the vessel and deflection changes. Fig. 5 shows the steps of finding the catheter vessel interaction contact forces as follow: 1. Image processing catheter segmentation 2. Finding and tracking contact points 3. Computing deflection of contact points with respect to un-deformed cantilever model 4. Creating the FEM model and feeding deflections to boundary conditions 5. Reading reaction forces as estimated catheter-vessel interaction forces.

2.2.2 Experimental Setup Design

Experimental setup aims to measure guidewire contact forces at each separate contact point directly, so guidewire has been inserted into separated contact point phantoms (CPPs) instead of a full vascular phantom. Fig. 6 depicts the experimental setup

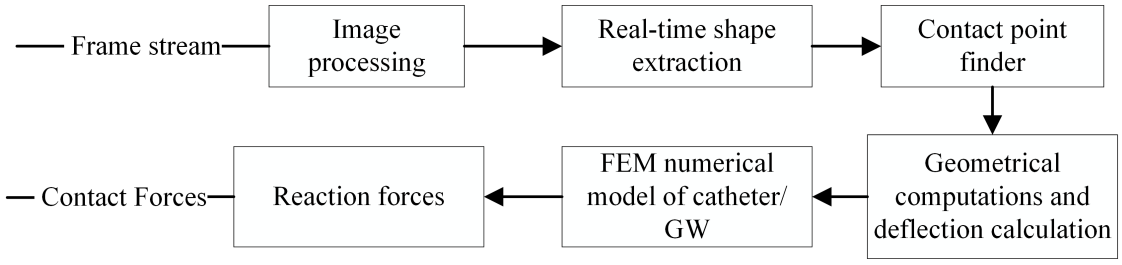

Figure 5: The flowchart of sensor-less force estimation steps.

including orange-colored contact point phantoms, camera, 6 DOF force/torque (F/T) sensor (Gamma, ATI Industrial Automation,Inc., USA) and Amplatz Super Stiff™ Guidewire (Boston Scientific, USA). Multiple 3D printed partial part of the vessel phantom, Polylactic acid (PLA) plastics, representing single contact points with the guidewire, positioned on a plate. At each experiment, one single contact point phantom rigidly is coupled to F/T sensor to provide an accurate and direct measurement of the forces exerted. The F/T measurements were read into Matlab (The Math-Works Inc., MA, USA) parallel to computational estimation at each step. As the contact forces are parallel with XY plane of the sensor, a force measurement of F_x and F_y are performed and the average Root-Mean-Square (RMS) was calculated to be an indication for total contact forces exerted on the contact point phantom. F/T sensor was zeroed before placing guidewire between contact point phantoms to remove the weights and to assure that the measured force only indicates CF with the guidewire.

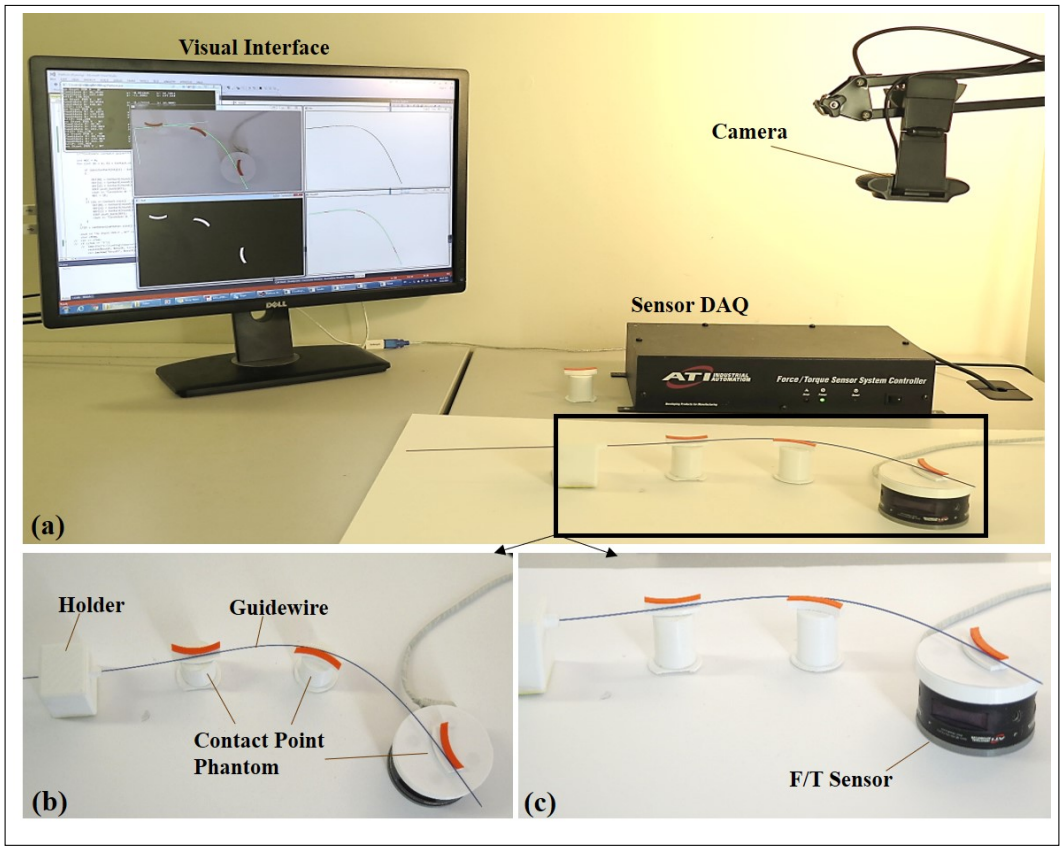

Figure 6: Experimental setup for direct contact force measurement at contact point phantoms, (a) General view of setup shows camera, direct force measurement setup and visual interface, (b) and (c) Close view depicting guidewire placed between contact point phantoms which the last one is mounted on F/T sensor.

2.3 Catheter Segmentation, Contact Point Tracking and FEM Modeling

2.3.1 Image based Catheter Segmentation and Deflection Tracking

Segmentation of the entire shape of catheter and tracking contact points are objected during the catheter navigation. The OpenCV (Open Source Computer Vision) library is used for image processing by programming in C++ interface. Images of the guidewire are continuously taken throughout an RGB camera with 1920*1080 pixels and 30Hz

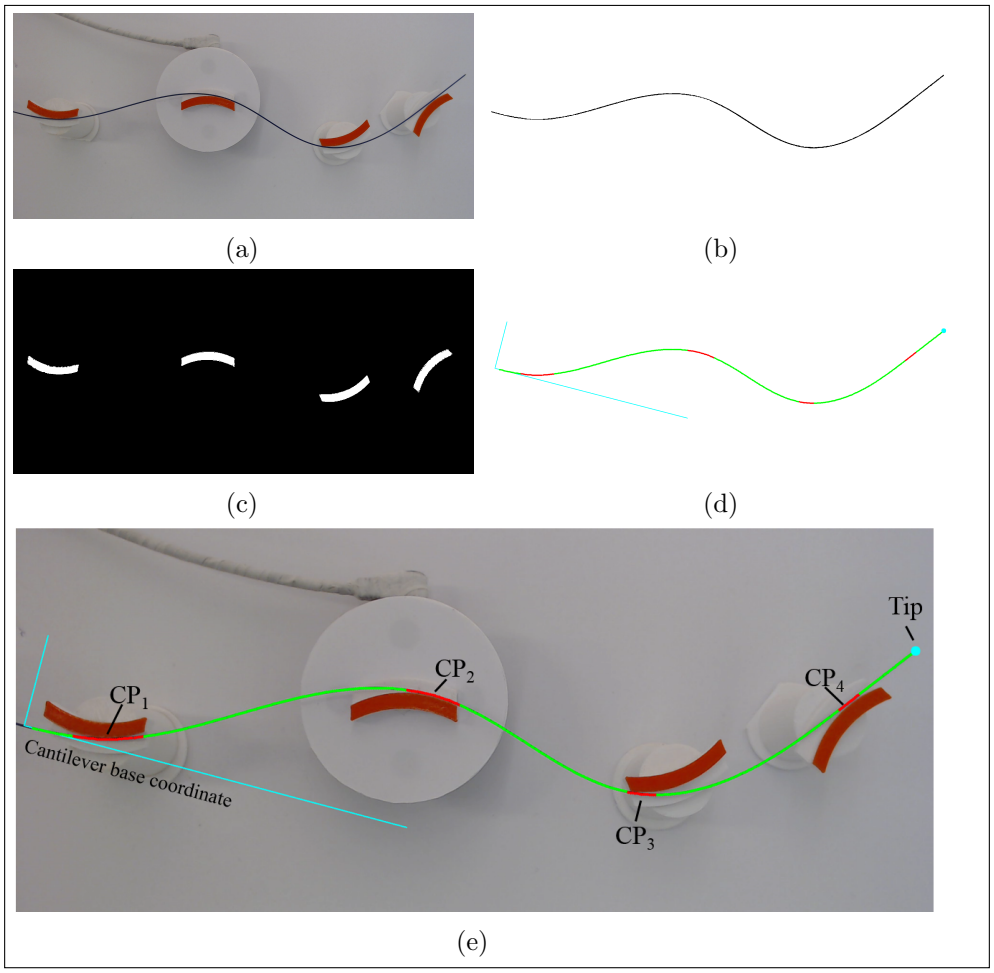

Figure 7: Guidewire segmentation and contact point tracking, (a) Original frame, (b) Masked guidewire binary image, (c) Masked vessel pieces binary image, (d) Highlighted guidewire in green and CPs in red, (e) Overlaid extracted guidewire, CPs, tip and base coordinate on the original sample.

frequency. Fig. 7 shows an example of extracting guidewire shape and locating its contact points with pieces of vessel phantom in orange color.

Algorithm 1 shows the pseudo code of the moving window search method for segmentation and tracking CPs and tip. A thresholding operation is implemented on the original frame (Fig. 7 (a)) to extract pixels in the range of guidewire HSV (Hue, Saturation, Value) color as shown in Fig. 7 (b). The same filter applied with HSV of vessel phantom color to obtain its pixels which result is shown in Fig. 7 (c). In the next step, a search algorithm with a moving window normal to the guidewire's black

Algorithm 1 Tracking the entire catheter shape and measuring deflections from camera image in OpenCV

Function image_processing(open video)

while video.read(frame) **do**
  $GW \leftarrow inrange(frame, HSV_{GW})$ ▷ guidewire HSV filter
  $VS \leftarrow inrange(frame, HSV_{vessel})$ ▷ vessel HSV filter
  while true $MovingWindow$ **do**
    $x \leftarrow 0$, $y \leftarrow 0$, $npixel \leftarrow 0$,
    for A search window normal to catheter **do**
      if Pixel value is 0 in GW **then**
        $npixel++$
        $x+ = xpixel$, $y+ = ypixel$
      end if
    end for
    $centroid(x) = x/npixel$, $centroid(y) = y/npixel$
    $arryCenter \leftarrow [centroid(x), centroid(y)]$
    if $centroid(x, y) - VS < CPreDefined$ **then**
      $arrayCP \leftarrow [centroid(x), centroid(y)]$
    end if
    if $npixel \leq minNBlackPixel$ **then** ▷ Catheter tip
      $XYtip \leftarrow [centroid(x), centroid(y)]$
    else
      $Tan \leftarrow$ Update the tangent line of catheter
      $MovingWindow \leftarrow$ Moved window align with direction of tangent line
    end if

return arryCenter, arrayCP, XYtip

pixel applied on both masked images of guidewire and vessel to compute guidewire centerline and find contact points. The search algorithm moves the window along the tangent line of the catheter, look for guidewire pixels, find their centroid and check whether the guidewire is in contact with the vessel or not. The window position is updated once each centroid point found. The tip is detected when the number of black pixels in the moving window is less than a predefined amount. In each window, a parallel search is made on vessel masked image to find the point of guidewire in contact with phantom pixels. The extracted guidewire centerline (in green), contact points (in red), tip (in light blue) and cantilever model base coordinate (in light blue) are highlighted in Fig. 7(d). They are overlaid on the original sample in Fig. 7(e)

which verifies algorithm accuracy. Proposed moving window search is robust to the possible gap or missing points.

2.3.2 FEM Model

The undeformed guidewire cantilever FEM model lays on the tangent line of guidewire (base coordinate in segmented image see Fig. 7) with the length measured from based point to the tip. Therefore, the deflection of the guidewire is measured with respect to a coordinate system on the base point such the x axis is the tangent line of guidewire. The guidewire centerline is transferred from global coordinate to base coordinate system by applying rotational and translational transformation matrix. Finding the length of catheter in mm from the base point to any wanted point on the catheter is straightforward by considering linear interpolation (see (2)) and information of mm-to-pixel size.

$$l_{CP_i} = \sum_{i=1}^{i=n_{CP_i}} \sqrt{(x_i - x_{i-1})^2 + (y_i - y_{i-1})^2} \tag{2}$$

Considering light weighted guidewires/catheters and slow-moving navigation procedures, the dynamic forces can be negligible with respect to large deflection reaction forces. The quasi-static simplification can be made to optimize the computational costs. For this study, ABAQUS commercial FEA solver is used by programming in C++ interface. The guidewire meshed with nonlinear beam elements with $3mm$ to $5mm$ size. Boundary conditions equal to the deflections at nodes of contact points are applied. A circular section with guidewire diameter and equivalent material properties assigned to the elements. The prepared model is fed to ABAQUS software solver which returns reaction forces at boundary conditions meaning contact forces. The catheter stiffness varies throughout its length and decreases closer to the tip. Thus, the different values of Elastic Modulus E are assigned to elements based on their

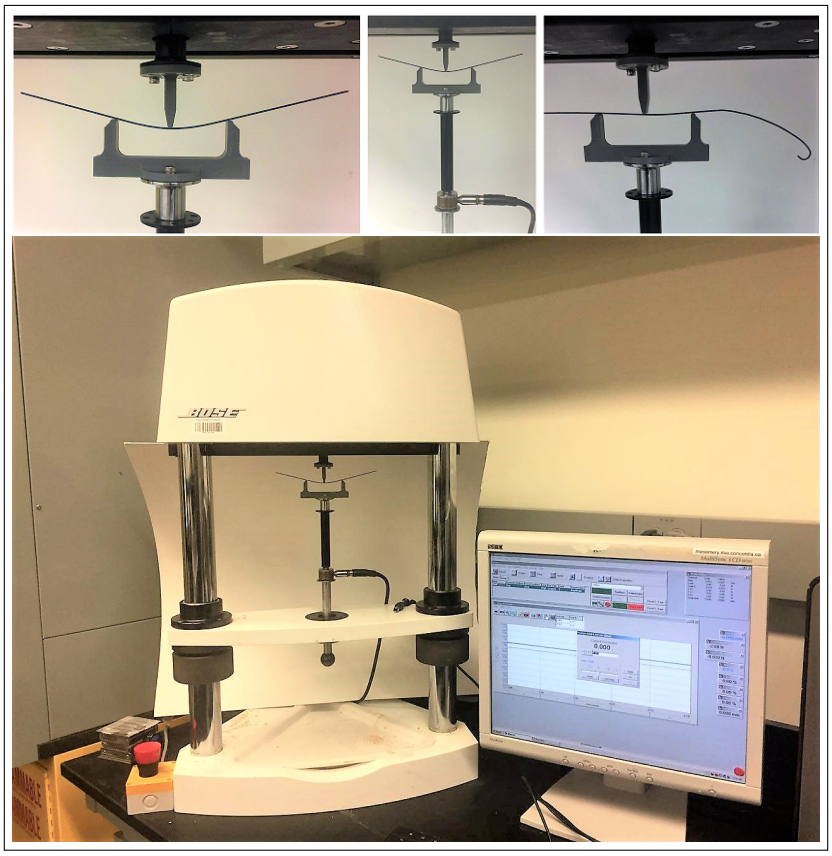

Figure 8: Three point bending test setup

distance from the tip.

Three-Point-Bending Test: Boston Scientific's Amplatz Guidewire is a stainless steel wire at the core with surrounded flat-wire coil [119]. The inner core diameter of guidewire varies throughout its length in order to provide lower strength closer to the tip for safety and higher in proximal end for stability and torquability in navigation procedures. The guidewire equivalent modulus of elasticity in bending (E_B, bending modulus) has provided by three-point-bending tests with a custom designed setup shown in Fig. 8. Tests are performed using Bose® Electroforce 3200 dynamic testing machine (Bose Corp., Massachusetts, US), equipped with a high-resolution force cell. It measures the load (P) vs deflection (d) of the specimen at the middle of the support

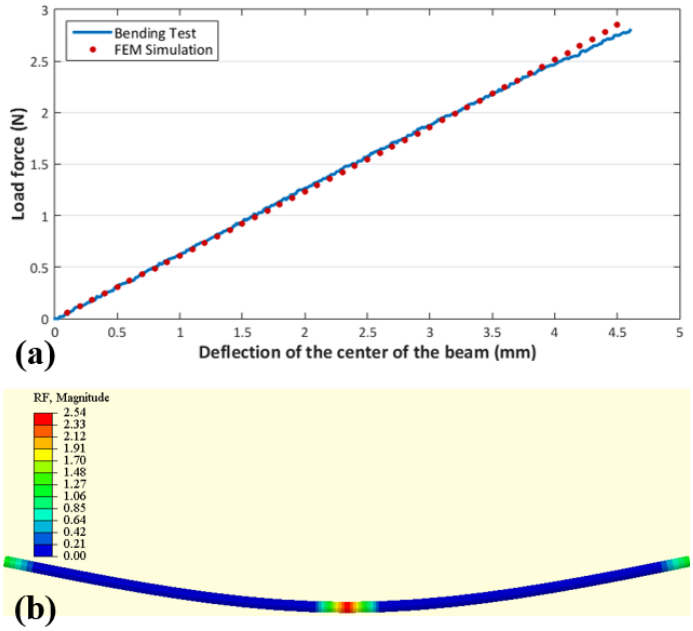

Figure 9: (a) Three-point-bending load-deflection curve (blue line) and corresponding FEM results (red dots) are in high agreement, (b) Force reaction of FEM simulation for a case with 4 mm deflection at middle span (as an example).

span. E_B is calculated using (3).

$$E_B = m\frac{L^3}{48I} \tag{3}$$

Where L (mm) is support span and I (mm^4) is the second moment of area for guidewire section. Parameter m (N/mm) is the slope of the tangent to the initial straight-line portion of the load-deflection curve. Tests are performed for pieces of guidewire cut at different distances from the tip to find E_B based on the distance from the tip. Fig. 9 shows a sample of load-deflection curve for a piece of guidewire which calculated equivalent E_B is 66 GPa. The same condition of the three-point-bending test is given to a FEM model with the equivalent E_B and reaction forces compared with tests result. The FEM results are in 98.2% agreement rate with the experimental test (see Fig. 9). This is to assure that the equivalent bending modulus is acceptable for guidewire complex structure and force estimation goal. Bending modulus of 22.2

GPa up to 73.4 GPa has been found for guidewire sections from the tip (excluding flexible coil part) to the point with 50 cm distance from it. Catheters/guidewires with the same model and build are designed to have consistent elastic modulus, thus, three-point-bending tests should not be repeated for every catheter/guidewire.

2.4 Experimental Validation, Results and Discussion

2.4.1 Experimental Validation Protocol

A number of experiments have been designed to evaluate guidewire interaction contact forces with several contact points and different shapes as guidewire being deflected in navigation procedure. Fig. 10 shows six scenarios with two, three and four contact points. At each scenario, one specific contact point was measured by F/T sensor to be compared with the sensor-less solution. It should be noted that the sensor-less method estimates all CFs however one CF targeted for evaluation purpose. In positioning two CPPs, the sensor measurement and consequently evaluation were made at the second contact point. Scenario with three CPPs evaluates the second and third contact points. In experiments with four CPPs, second, third and fourth contact points have been targeted. These six scenarios are named based on the number of contact points and then targeted contact point as follows $2CP - CP_2$, $3CP - CP_2$, $3CP - CP_3$, $4CP - CP_2$, $4CP - CP_3$ and $4CP - CP_4$.

Fig. 11 illustrates the targeted contact point displacement. At each scenario, the position of F/T sensor which hold targeted contact point was shifted toward right, left, up and down to make changes in the amount of deflection and guidewire shape. This can simulate insertion in actual vascular anatomy.

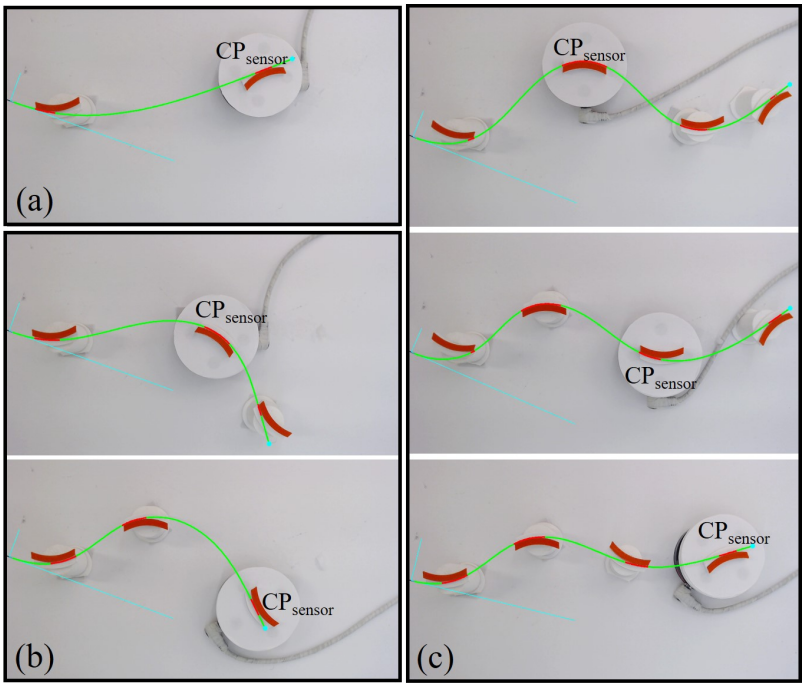

Figure 10: Six scenarios for sensor-less contact force estimator evaluation, (a) $2CP - CP_2$ scenario: Two CPPs with contact force measurement in CP_2, (b) $3CP - CP_2$ and $3CP - CP_3$ scenarios: Three CPPs and contact force evaluation in CP_2 and CP_3, (c) $4CP - CP_2$, $4CP - CP_3$ and $4CP - CP_4$ scenarios: Four CPPs and contact force evaluation in CP_2, CP_3 and CP_4 respectively.

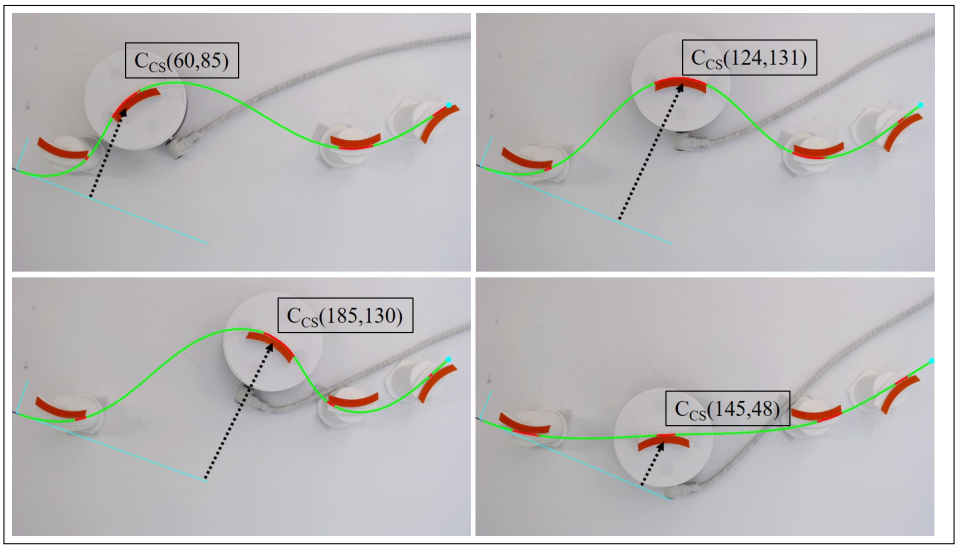

Figure 11: Moving position of F/T sensor to the left, up, right and down continuously to impose a variation in deflections and shape.

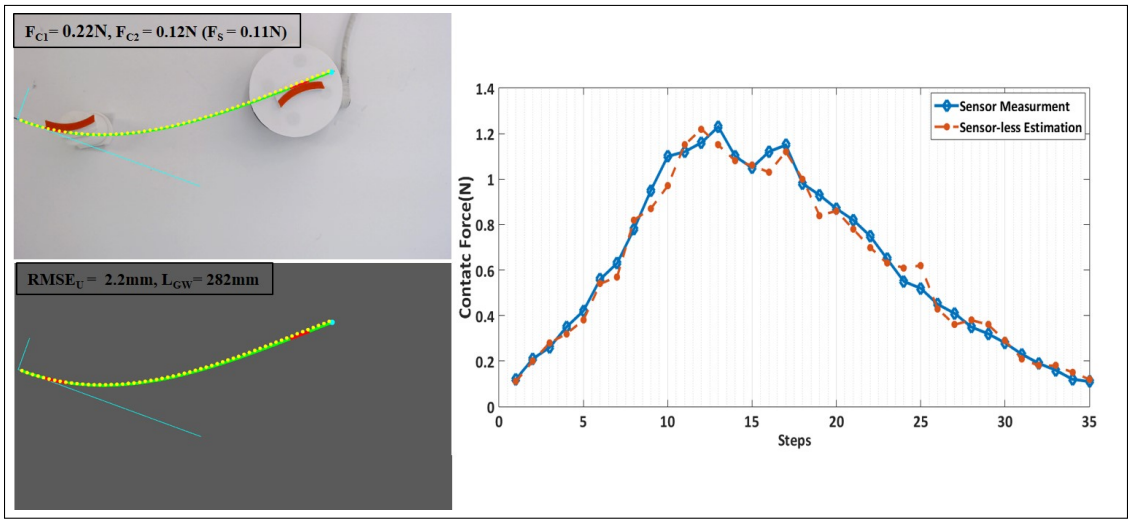

Figure 12: Example of $2CP - CP_2$ scenario showing FEM result in yellow dot on the actual guidewire in green (left). The graph of estimated CF (in red) follows measured force (in blue) with a high accuracy while CP_2 was moving (right).

2.4.2 Results and Discussion

Sensor-less guidewire contact force estimation has been evaluated in six scenarios which are physically simulating guidewire interaction with vasculature. Fig. 12 illustrates an example image of two contact point scenario $2CP - CP_2$ results. The deflected shape of guidewire from numerical modeling in yellow dots overlaid on its actual guidewire shape in green line. Fig. 12 graph shows sensor-less force estimations vs measured contact forces by F/T sensor as CP_2 was displaced continuously toward CP_1, up and down. The estimated force closely follows the measured data with 92.44% average accuracy and $0.049N$ Root-Mean-Square-Error (RMSE_F) where average and max CF are $0.62N$ and $1.23N$ respectively. $2.8mm$ RMSE_U, error in estimating the deflected shape of guidewire, proves the high reliability of FEM numerical approach in simulating guidewire deflections.

The same sort of results are collected in Fig. 13 for $3CP - CP_2$ and $3CP - CP_3$ scenarios. The average accuracy above 90% is reached in both cases with $0.091N$ and $0.073N$ RMSE_F where average CFs are $1.25N$ and $0.69N$ receptively.

The results for scenarios with four contact points confirm that an increase in the

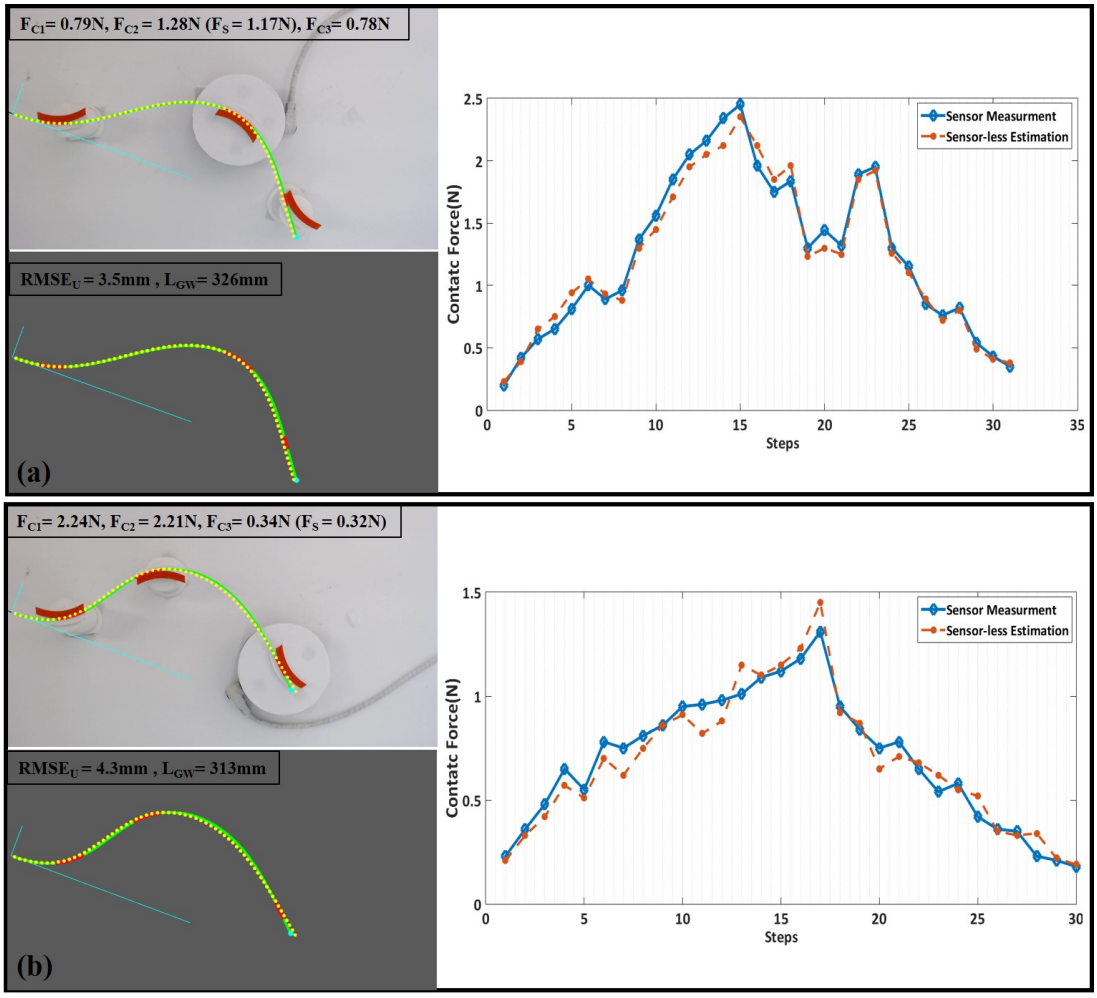

Figure 13: Yellow dots are numerical estimations and the green line is the actual guidewire. Graphs show trend in CF measurement and sensor-less estimation, (a) $3CP - CP_2$ scenario, (b) $3CP - CP_3$ scenario.

number of contacts points would not change the accuracy of sensor-less proposed approach as shown in Fig. 14 and Table 3. $4CP - CP_2$ and $4CP - CP_3$ scenarios give the average accuracy above 94%. RMSE_F ($0.093N$ and $0.12N$) is higher in these cases which is because of increased amount of exerted CF ($2.01N$ and $2.41N$ average CFs and $3.49N$ and $4.25N$ max CFs measured in $4CP - CP_2$ and $4CP - CP_3$ scenarios respectively). $4CP - CP_4$ scenario has a lower accuracy of 87.9% in force estimation compared $4CP - CP_2$ and $4CP - CP_3$ scenarios. The higher shape estimation error, in this case, might be the reason for lower force accuracy (see Table 3).

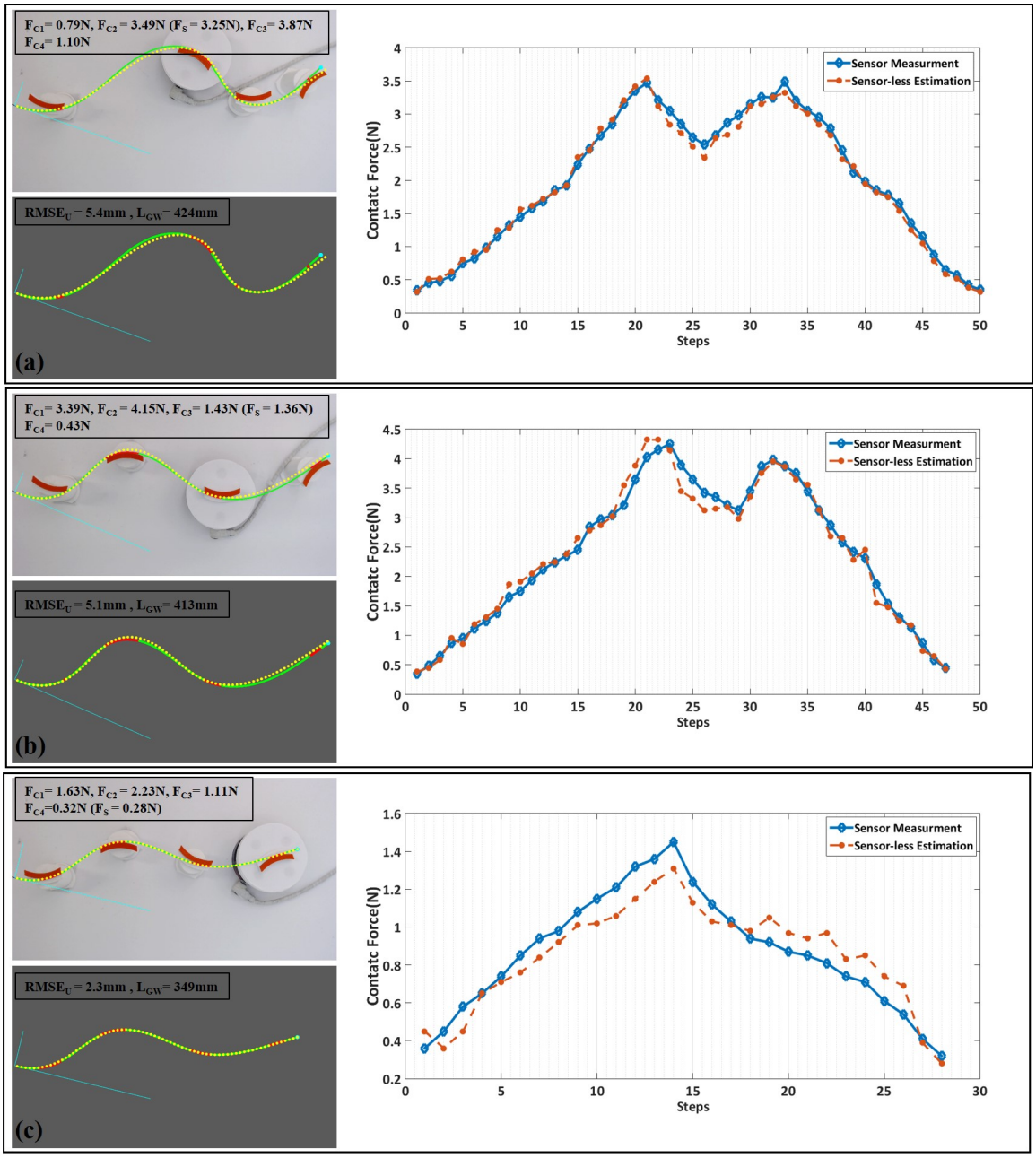

Figure 14: Yellow dots are numerical estimations and green line is actual guidewire in images. The graphs show sensor-less estimation (red) vs actual force measurement (blue) as targeted CP was displaced, (a) $4CP-CP_2$ scenario, (b) $4CP-CP_3$ scenario, (c) $4CP-CP_4$ scenario.

Table 3: $RMSE_F$ for contact force estimation, average and maximum contact force, $RMSE_U$ in shape modeling and length of the guidewire in each scenario are tabulated.

Scenario	$RMSE_F$ (N)	Average Accuracy	Average CF(N)	Max CF(N)	$RMSE_U$ (mm)	L_{GW} (mm)
$2CP-CP_2$	0.049	92.44%	0.62	1.23	2.8	264
$3CP-CP_2$	0.091	93.2%	1.25	2.45	3.9	315
$3CP-CP_3$	0.073	90.34%	0.69	1.31	3.7	332
$4CP-CP_2$	0.093	94.9%	2.01	3.49	4.3	412
$4CP-CP_3$	0.12	94.11%	2.41	4.25	4.1	432
$4CP-CP_4$	0.11	87.93%	0.86	1.45	4.8	397

Table 3 includes $RMSE_F$, average accuracy, average CF, max CF, $RMSE_U$ and guidewire length for all six scenarios. From $2.8mm$ to $4.8mm$ average $RMSE_U$ in guidewire shape estimation are captured. The higher $RMSE_U$ in scenarios with more number of CP can be because of longer guidewire length in the numerical model. Highest average accuracy of 94.9% reached in $4CP - CP_2$ and lowest one was in $4CP - CP_4$ with 87.93% average accuracy. In all cases, the estimated forces do not follow underestimation or overestimation trend meaning no systematic error is coming from our proposed approach. Noises are likely caused by the errors in deflection measurements from imaging and continuous variation in E_B through guidewire length which is assumed to be discrete in our FEM modeling. The complex guidewire structure is considered a solid cross section with the equivalent bending modulus which can affect the accuracy but is not significant. The sensor-less force estimation in all cases shows satisfactory results. The amount of forces reported here are measured for random deformations to show the significance of the method and are not necessary the same magnitude in practice.

2.5 Conclusion

Endovascular intervention procedures carry the risks of damages on arterial wall, embolization and stroke. Measuring the catheter/guidewire contact forces in interaction with vessels is beneficial to enhance the safety of navigation process. In this paper, a sensor-less guidewire contact force estimation approach is proposed by feeding image based deflection measurement data to a numerical FEM model. Guidewire segmentation throughout image processing algorithms provides information about the position of contact points on guidewire and measures the amount of deflections and lengths. Three-point-bending tests are performed to provide the equivalent bending modulus of the complex structure of guidewire to be used in the numerical model. Collected data from imaging are given to the FEM model to estimate the contact forces. The accuracy of approach has been tested throughout a custom-designed platform for direct CF measurement and physically simulating guidewire-vascular interaction with different contact points. The average accuracy in force estimations was from 87.9% to 94.9% with maximum $0.12N$ RMSE where contact force as high as $4.25N$ (average $2.41N$) is seen. The significants of the proposed force estimation approach are in its applicability on all conventional catheters/guidewires without making any change in structure or having embedded sensors. It can be a low-cost efficient multiple contact point force sensing solution by getting feedback from X-Ray fluoroscopic imaging in endovascular interventions. A safety indicator based on contact forces and max safe forces can be displayed for physician guidance. The future works focus on 3D force estimation of catheters/guidewires; contact force estimation in clinical environment and contact force control systems in vascular robotic intervention. This paper has presented the primary conceptual study for next future steps.

Chapter 3

Image-based Intraluminal Contact Force Monitoring in Robotic Vascular Navigation

Embolization, stroke, ischaemic lesion, and perforation remain significant concerns in endovascular interventions. Sensing tool interaction inside the artery is advantageous to minimize such complications and enhances navigation safety. Intraluminal information is currently limited due to the lack of intravascular contact sensing technologies. We present monitoring of the intraluminal tool interaction with the arterial wall using an image-based estimation approach within vascular robotic navigation. The proposed image-based method employs continuous finite element simulation of the tool motion using imaging data to estimate multi point forces along tool-vessel wall interaction. We implemented imaging algorithms to detect and track contacts, and compute pose measurements. The model is constructed based on the nonlinear beam element and flexural rigidity profile over the tool length. During remote cannulation of aortic arteries, intraluminal monitoring achieved tracking local contact forces, building a contour map of force on the arterial wall and estimating tool structural stress. Results

suggests that high risk intraluminal forces may happen even with low insertion force. The presented online monitoring tool delivers insight into the intraluminal behavior of endovascular tools and is well-suited for intraoperative visual guidance for the clinician, robotic control of vascular procedures and research on interventional device design.

3.1 Introduction

Endovascular interventions are leading treatments and diagnoses for cardiovascular disease. Despite improvements in tools and techniques, intraprocedural risks of embolization, ischaemic brain lesions, and stroke in percutaneous procedures are still high, especially in carotid artery stenting [59, 120]. Studies reported that 50% of the cases after carotid stenting had a new ischaemic lesion on diffusion-weighted imaging (DWI) of the post-treatment scan due to embolism. [60]. The high number of microemboli, which has been reported during navigation of catheters and guidewires, highlights the importance of tool-tissue interaction [121, 122]. Studies have further pointed out other complications, perforation, thrombosis and dissection, as a result of catheter/guidewire interactions with the arterial wall [56]. In the case of stenosis treatment, excess insertion force to cross occlusion could raise the likelihood of perforating [123]. Limited motion of under-actuated conventional catheter and guidewire can further add to the risk, especially in the case of a diseased and torturous vessel. These findings suggest that the intraluminal interaction contact force (CF) is one of the determinants of patient safety and procedure efficiency. Monitoring force information intraoperatively has the potential to enhance navigation safety and efficiency. Practical applications are threefold:

- Integrating CF data into intraoperative visual guidance for clinicians to bring safe catheter/guidewire manipulation. Intraluminal insight could minimize the risk of stroke, embolism, vessel perforation, or dissection. It could further

limit human mishandling, especially in the case of novices, with implications to improve training for complex procedures.

- The development of an automated robotic surgery system that maintains CF in a safe range and improves smoothness using realtime intraluminal data. Vascular robotic technology demonstrated definite advantages in catheter controllability, stability, precision, and lower radiation for clinicians [124–128]. With the advent of artificial intelligence, a safe and autonomous form of robotic surgery can be introduced [128, 129].

- Intraluminal force information, along with catheter deflection data can also be used for research on design of interventional tools aimed to minimize vessel injuries and maximize maneuverability, torquability and deliverability. It would be beneficial to study the intraluminal performance of interventional devices and optimize their design.

Intraluminal interaction information is limited due to the lack of force sensing elements along the endovascular tools or other remote sensing technologies. Tool-tissue contact force sensing remained limited to the tip single point force measurement. In electrophysiology, proper contact of the catheter tip and contact force are essential due to the chance of over-burn in case of excessive CF or inferior lesion quality in weak contact [130]. Studies proposed ablation catheters with tip force sensors [78, 79, 103] and some are available commercially [108, 109]. Instrumented cardiovascular tools remain limited to tip-mounted force sensing in which the complexity of integrating sensing elements, cost, maneuverability, and interference with nearby devices are some of the associated challenges. The instrumentation of guidewires is more challenging due to their smaller diameter and complex structure. Indirect force estimation at the tip of ablation catheter has worked based on modeling and shape analysis, e.g., kinematic model, cosserat rod, and piecewise planar elastica: [93, 94, 110, 112, 131] has

reported promising results. On the other hand, proximal insertion force measurement and methods to control it have been used in robotic catheterization [42], even though this force does not represent local vessel interaction forces. A quantitative analysis of the total contact force between the instrument and cardiovascular phantoms has been established in robotic navigation [132] as well and used as an assessment metric [45, 133] of navigation, whereas the relation between the total exerted force and local intraluminal CF is not entirely clear.

Monitoring intraluminal vessel contact forces throughout the length of the tool is a gap in the literature. In previous work [134], we presented and validated a sensor-less approach to estimate multi-point load forces at the side of interventional tools. This study aims to develop the proposed approach to intraluminal interaction force monitoring within navigation of an anthropomorphic cardiovascular phantom and to employ a teleoperated robotic platform. The FEM formulation has been improved to consider shear deformation based on Timoshenko beam theory. Image segmentation algorithms have been updated for intravascular contact tracking and pose measurements within the phantom. This study also presents a quantitative analysis to investigate the resultant force exerted on the vasculature compared with intraluminal contact forces (ICF), to highlight the potential need for local tool-tissue monitoring. A two-degree freedom (DOF) insertion robot is designed and fabricated based on the methods in conventional manual navigation which allow simultaneous and independent control of insertion and rotation. The 6 DOF force/torque sensor is coupled to the aortic arch phantom to measure the resultant force exerted on the vasculature. catheter/guidewire, as a fixed model parameter input, is measured through a sequential bending test over its length. The nonlinear finite element model is set to simulate the tool navigation using real-time image-based pose measurements. Solving the inverse FEM model estimates the contact forces and catheter's deflected shape. We present the contour map of intraluminal CF on vessel boundaries and

the tracking of multiple local ICF. An intravascular stress analysis of the tool is also conducted via the proposed method. In the manuscript, "catheter" refers to any general type of non-steerable catheters and guidewires for conventional endovascular intervention.

3.2 Methods and Algorithm

3.2.1 Contact Force Estimation

The accuracy of the proposed sensor-less force estimation concept was shown in the previous work [134] through a direct force measurement setup, i.e., single contact point phantoms mounted on a 6-DOF F/T sensor. An estimation accuracy of over 87% was achieved in agreement with force sensor measurements [134]. The proposed method is based on continuous simulation of catheter deflection as a beam using data from real-time imaging. Image processing segments and tracks the deflected catheter shape and locates the interactions with the internal wall of the vasculature. Using image processing data and prior knowledge about the intrinsic shape of the catheter, an FEM model is built and solved. Deflections induced by the vessel wall at the contact points set the boundary conditions of the model, and reaction forces computed from these boundary conditions return the contact forces. Deflections are fed to the model continuously to simulate catheter manipulation. The FEM model is based on the Timoshenko beam element, considering nonlinear large deformation. The model assumes that the catheter structure is a uniform round beam with an equivalent bending modulus.

Let us describe a schematic view of a catheter-vessel interaction as shown in Fig. 15. A section of the catheter beginning at any desired point and ended at the tip is modeled as a cantilever, which has all contact points included (window shown in Fig. 15). The model is created in the local coordinate of the catheter, having

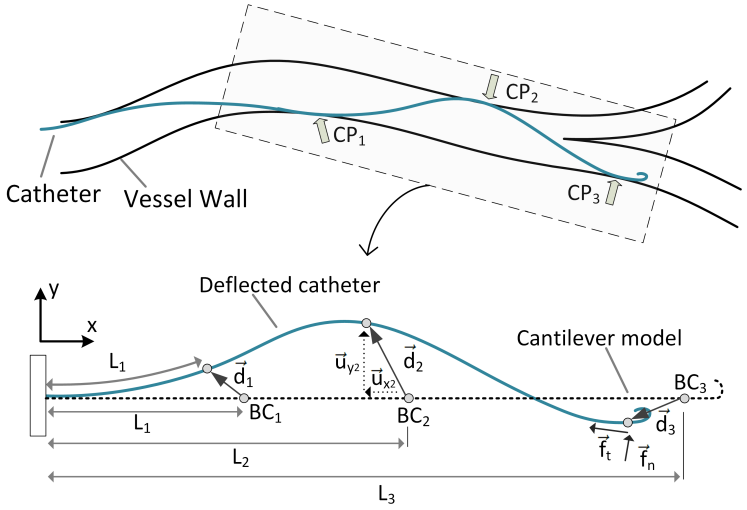

Figure 15: Force estimation concept showing deflected catheter and constructed cantilever model. CP_is are the contact points with length of L_i on the deflected shape and BC_is are the associated boundary condition on the model.

the $\vec{x}$ axis tangent to its base. This is to compute deflection from the catheter base perspective and isolate it from the global coordinates. The cantilever model has an intrinsic catheter body of length equal to the deflected shape in the window, $L_{cantilever} = L_{tip}$. The model length varies as the catheter advances or retracts during navigation. The initial positions of contacts points on the model have equal lengths as on the deflected catheter. For instance, the position of contact point i is CP_i, which has length L_i along the deflected shape, and the corresponding point with the same length on the cantilever model would be the boundary condition BC_i, i.e., it is the contact point before being deflected. Contact deflection $\vec{d_i}$ is the displacement between the deflected contact point position, P_{CPi}, and its rest position on the model, P_{BCi} (see (4) and (5)). Deflections, $\psi(d) = \{\vec{d_i}\}$, are applied to boundary conditions $BC = \{BC_i\}$, respectively. By solving the inverse FEM model, the catheter is being deflected as it is interacting with the vessel, which simulates the current state. The FEM model computes the reaction forces, $\bar{CF} = \{\bar{F_i}\}$, at boundary conditions as estimates of the contact forces on the vasculature. Even though the magnitude of contact forces matters for safety, CF can be broken into components of normal ($\vec{f_n}$)

and tangential/frictional forces ($\vec{f_t}$) if such information is needed. As the catheter navigates through the vasculature, its deflected shape, the position of contact points, and the amount of deflection change. The cantilever FEM model parameters and computed contact forces are updated in real-time accordingly.

$$\vec{d} = \vec{u}_x + \vec{u}_y = \begin{bmatrix} u_x & u_y \end{bmatrix} \tag{4}$$

$$\psi(d) = \begin{bmatrix} \vec{d_1} \\ \vdots \\ \vec{d_i} \end{bmatrix} = \begin{bmatrix} u_{x1} & u_{y1} \\ \vdots & \vdots \\ u_{xi} & u_{yi} \end{bmatrix} = \begin{bmatrix} x_{CP_1} - x_{BC_1} & y_{CP_1} - y_{BC_1} \\ \vdots & \vdots \\ x_{CP_i} - x_{BC_i} & y_{CP_i} - y_{BC_i} \end{bmatrix} \tag{5}$$

In our experiments, a planar projection model is adapted to demonstrate practical feasibility as a proof of concept for ICF monitoring where the distal section of the tool almost lays within a plane. Thus, in this particular test case, the effect of out-of-plane deflection is considered minor compared to the large in-plane deflections. This might not apply to other endovascular procedures requiring a 3D implementation. Iliac curve arteries and coronary arteries are examples where the out-of plane deflection and 3D imaging should be considered.

3.2.2 Image Segmentation and Contact Tracking

Image segmentation obtains data required for the model, including lengths from catheter base to every contact point and tip, positions and deflections of contact points in the local coordinates of the catheter (see Fig. 15). The OpenCV (Open Source Computer Vision) library is used for image processing programmed in C++. Images are continuously sampled through an RGB camera with 1920*1080 pixels at 30 frame per second (FPS). The RGB image is converted to grayscale to be similar to X-ray fluoroscopic images. Medical imaging and visualization systems (X-ray fluoroscopy, CT and MRI) enable the detection and tracking of the shape of the catheter and

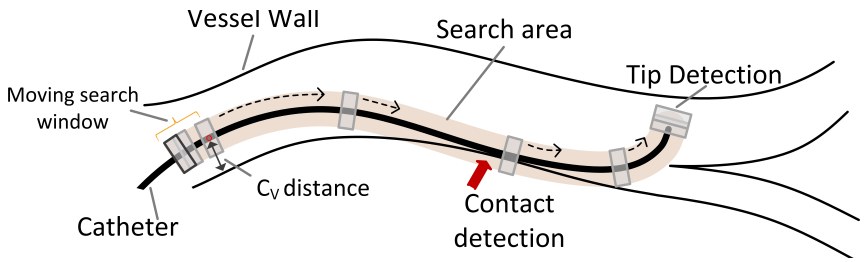

Figure 16: Moving search window sweeps catheter along its length to extract centerline, and detect contacts and tip.

vessel boundaries in cardiovascular interventions. In this study, we detect the vessel using the contrast between the vascular phantom and the background, similar to injecting contrast agent to visualize the lumen in X-ray fluoroscopy. We assume there is no extreme movement or change in vessels during the procedure; however, an online calibration technique can be used to match the vessel image in case of any movement like breathing in a clinical case.

Image segmentation is divided into two main phases: extracting mask images of the tool and vessel boundaries, followed by search and tracking (Fig. 16). A Gaussian filter (Gaussian kernel of size=5) is applied to filter out noise and then, a canny-edge detector algorithm (kernel size of 3 for the Sobel operations, ratio of lower to upper threshold of 5:1) is used to extract vessel boundaries [135, 136]. To extract catheter pixels, a thresholding operation is implemented on the grayscale frame. Then, dilation followed by erosion are applied to fill possible gaps and connect lines. The imaging algorithm is tested on the cannulation of aortic arteries by a guidewire (experimental setup is explained in later sections). Fig. 17 (b) and (d) display images of the phantom boundary mask and a guidewire mask, respectively.

An algorithm with a moving search window normal to the guidewire curve is designed to sweep the entire length of the guidewire, as depicted in Fig. 16. The algorithm moves a rectangle search window along the tangent to the guidewire $\theta(s) = \frac{dy}{dx}$, where s is the position along the curve. The starting point of the search is determined with an initial search step over the base frame. The search window

Algorithm 2 Segmentation and tracking

Function image processing

video.read($frame$)

$frame \leftarrow RGBtoGry(frame)$

$frame \leftarrow Gaussianfilter(frame)$ ▷ filter out noise

$B_{VS} \leftarrow canny(frame)$ ▷ extract vessel boundaries

while video.read($frame$) **do** ▷ tracking

  $GW \leftarrow threshold(frame)$ ▷ extract guidewire

  $GW \leftarrow$ dilate and then erode GW

  while Moving search window is true **do** ▷ search

    for search pixel of window normal to catheter **do**

      if pixel value is 0 in GW **then**

        compute center of pixels

      end if

    end for

    $C_{GW} \leftarrow [centroid(x), centroid(y)]$

    if $C_{GW} - B_{VS} < predef$ **then** ▷ contact detection

      $P_{CP_i} \leftarrow [centroid(x), centroid(y), L_{CP_i}]$

    end if

    if $npixel \leq minNPixel$ **then** ▷ tip detection

      $P_t \leftarrow [centroid(x), centroid(y), L_{tip}]$

    else

      $\theta \leftarrow$ update the tangent to the catheter

      $P_{MovingWindow} \leftarrow$ update and move search window

    end if

  end while

return $C_{GW}, B_{VS}, P_{CP_i}, P_t$

finds guidewire pixels and computes their centroid C_G. In each window, a parallel logic operation is made on the masked vessel image to find the point of contact with boundaries (VB) where the distance of the guidewire centerline and VB, C_V, is less than a predefined contact distance. The search window position is updated along $\theta(s)$ once each centroid point is found and moved toward the tip. The tip is detected where the number of contiguous pixels is less than a predefined amount. Algorithm 2 presents the pseudo-code of the extraction and moving window search method in segmentation and tracking. The proposed moving window search is robust to possible gaps or missing points.

Fig. 17 shows step by step segmentation results for interaction of a guidewire with

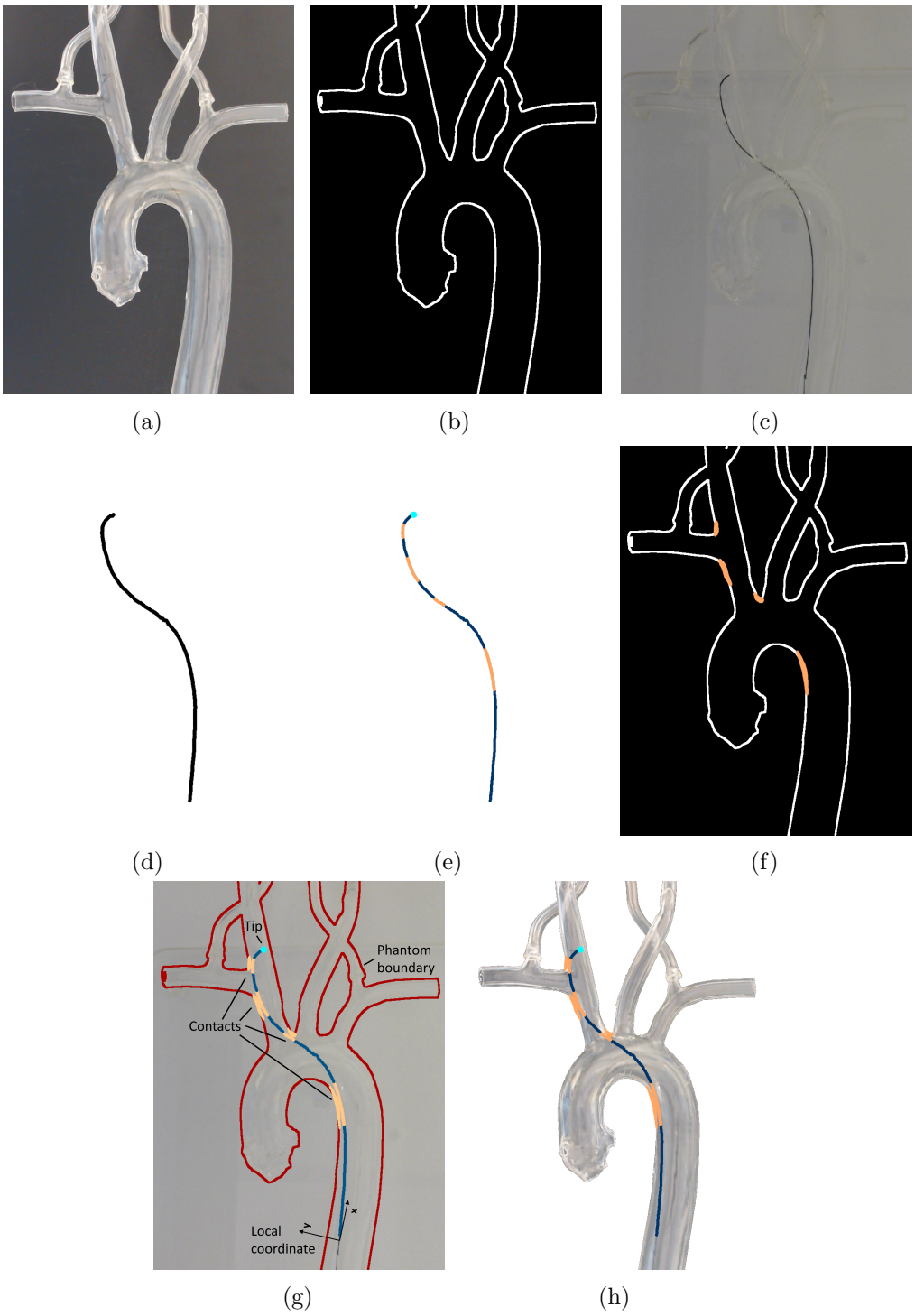

Figure 17: Steps in image segmentation of tool interaction and tracking contacts: aortic arch phantom (a), phantom boundaries mask (b), navigated guidewire in RCCA (c), guidewire mask (dilated for visual purpose) (d), contact and tip detection on GW (e), contact detection (f), segmented guidewire and vessel displayed on the original frame (g) and (h).

the aortic arch phantom in our experimental. Fig. 17 (g) and (f) depict segmented guidewire-vessel interaction overlaid on original frames, which show the effectiveness of the segmentation and search algorithm.

The last step converts pixel values to length units using camera calibration parameters. Afterward, the length of any desired point along the guidewire can be computed by numerical integration. Derived parameters are: tip pose $P_t = \{x_t, y_t, l_t\}$, contact point pose $\{P_{CPi}\} = \{x_{CP_i}, y_{CP_i}, l_{CP_i}\}$ and GW center-line pose $\{C_{GW}\}$.

3.2.3 Finite Element Model

Consider a planar two-node beam element of length l, where each node has three degrees of freedom, as defined in Fig. 18. The nodal displacement vector contains longitudinal (u_x), transverse (u_y) displacement and rotation (φ) for both nodes.

$$e = \begin{bmatrix} u_{x1} & u_{y1} & \varphi_1 & u_{x2} & u_{y2} & \varphi_2 \end{bmatrix}^T \tag{6}$$

The global elements coordinate vector is defined as

$$\{e\} \equiv \begin{bmatrix} u_{x1} & u_{y1} & \varphi_1 & \dots & u_{x(N+1)} & u_{y(N+1)} & \varphi_{(N+1)} \end{bmatrix}^T \in R^n \tag{7}$$

where N is the number of element and $n = 3(N + 1)$ is the number of degrees of freedom. In the earlier study [134], we presented results based on Euler-Bernoulli (EB) beam theory whereas here the formulation has been updated to the Timoshenko beam theory. EB assumes thin beams where angular distortion due to shear deformation is considered negligible, and cross-section is perpendicular to the bending line (neutral axis). Timoshenko beam theory is generic compared to EB theory. Its employed formulation accounts for large axial, bending, and shear deformations as well as large translation and rotation of the beam structure. The governing equations of

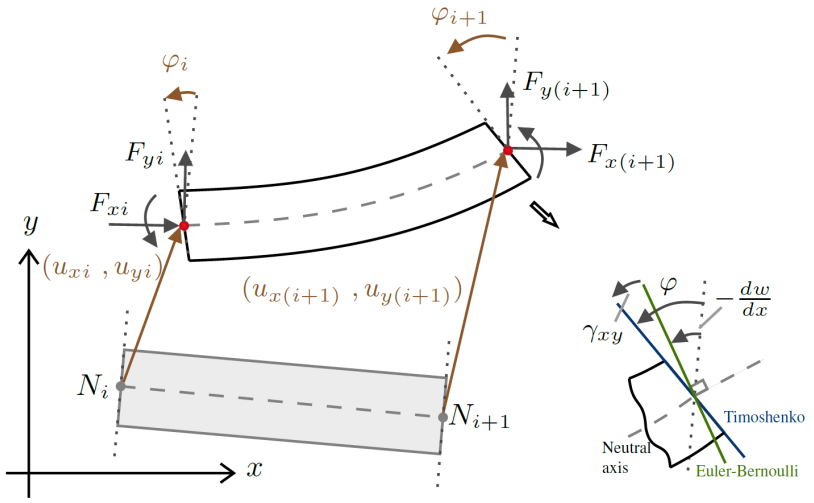

Figure 18: Generic beam element, including the nodal forces (F) and the displacement vectors (u), showing initial and deformed states. Euler-Bernoulli beam is compared with that of a Timoshenko.

Timoshenko beam theory are the following:

$$\frac{d^2}{dx^2}(EI\frac{d\varphi}{dx}) = q(x) \tag{8}$$

$$\frac{dw}{dx} = \varphi - \frac{1}{\kappa AG}\frac{d}{dx}(EI\frac{d\varphi}{dx}) \tag{9}$$

where E and G are the elastic modulus and shear modulus. L, I and A are the length of the beam, second moment of area and cross section area, respectively. κ is the Timoshenko shear coefficient and $q(x)$ is the load [137]. Fig. 18 compares Timoshenko beam deformation to EB, where the cross-section of a beam element remains planed but not necessarily perpendicular to the beam axis, i.e., $\varphi(x) \neq \frac{dw}{dx}$ and γ_{xy} is shear [138, 139]. Timoshenko can be used for thick as well as slender beams, which is the more accurate choice for modeling of catheters and guidewires, especially where the beam cross-sectional dimensions is small compared to typical distances along its axis.

The equilibrium of a finite element beam model at time t is

$$M\ {}^{t}\ddot{u} + C\ {}^{t}\dot{u} = {}^{t}R - {}^{t}F \tag{10}$$

where $M \in R^{n\times n}$ is the mass matrix and $C = \alpha M$ is the damping matrix proportional to mass with coefficient α. $R \in R^n$ is the external load vector and $F \in R^n$ is the internal force vector in global coordinates. $\ddot{u}$ and $\dot{u}$ are acceleration and velocity vectors, respectively [140]. The velocities and acceleration vectors are small during navigation because of continuous contact with the vessel. Further, considering the low mass of the catheter/guidewire, the dynamic force is small compared to large external forces caused by large deflections. Thus, we are implementing a quasi-static solution to minimize the computational cost and reach a real-time execution.

Nodal force is formed based on individual vectors considering element connectivity.

$${}^{t}F_j = K\ {}^{t}u_j \tag{11}$$

$$K \equiv K_L + K_{NL} \tag{12}$$

${}^{t}F_j \in R^6$ is the internal nodal point force of the element j and ${}^{t}u_j \in R^6$ is the displacement vector. The stiffness matrix ($K \in R^{6\times6}$) consists of linear ($K_L \in R^{6\times6}$) and nonlinear ($K_{NL} \in R^{6\times6}$) parts [141]. Strain-displacement equations contain nonlinear terms that must be considered in the nonlinear part of the stiffness matrix. K_{NL} is achieved by applying Castigliano's theorem to the strain energy which counts the interaction between axial load and lateral deformation [142].

After transferring the finite element matrix of the local principal axis of the elements to global cartesian co-ordinate and performing an element assemblage process, the

incremental equilibrium equation of quasi-static analysis is:

$$({}^{t}_{t}K_L + {}^{t}_{t}K_{NL})\,{}^{\Delta t}u = {}^{t+\Delta t}R - {}^{t}_{t}F \tag{13}$$

where ${}^{t}_{t}K_L$ and ${}^{t}_{t}K_{NL}$ are stiffness matrices at time t, ${}^{t}_{t}F$ is the nodal point force at time t and ${}^{t+\Delta t}R$ is the externally applied nodal load at time $t+\Delta t$ [143]. The case of our problem is an inverse finite element since we have nodal displacement vectors u_i from imaging data to calculate R_i as the interaction contact forces. R is the resultant of all external forces applied to the catheter from the vessel, including normal and friction forces.

$${}^{t}R = {}^{t}R_f + {}^{t}R_n \tag{14}$$

R is computed regardless of type, condition, or material properties of the external environment. Viscoelastic effects of the tissue are already seen in the nodal displacement u as the softer or harder vessel would result in a change in deflection and model computes the associated forces simulating such change due to vessel material property. Consequently, no information about contact condition and tissue characteristics is needed. A geometrical computation is essential to create the cantilever model from imaging data, as given in Algorithm 3. The model is made based on intrinsic shape information and total length of guidewire used in experiments, L_{tip}. The boundary

Algorithm 3 Model preparation

Input Data from image-based pose measurement
$L_{beam} \leftarrow L_{tip}$
Create cantilever beam from intrinsic shape and L_{beam}
for $i < N_{CP}$ **do**
    $L_{BC_i} \leftarrow L_{CP_i}$
    Locate position of P_{BC_i} on cantilever beam based on L_{BC_i}
    $d_i = P_{CP_i} - P_{BC_i}$
    Apply d_i to BC_i
for $n < N_{elements}$ **do**
    Compute element length from tip S_e
    $EI_{element} \leftarrow EI(S_e)$ ▷ assign mechanical property

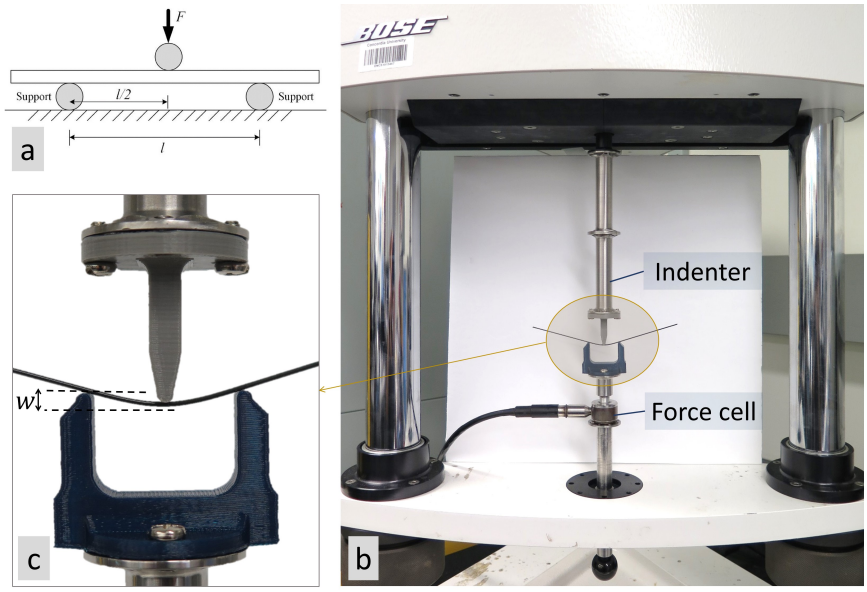

Figure 19: Three-point bending test: schematic concept (a), ElectroForce dynamic testing machine (b), deflected guidewire under test (c).

conditions are located on the model at the points (with L_{BC}) having an equal length to the contact points L_{CP}. The displacement vector d_i is measured from BC_i to CP_i (see 4) which is assigned to its associated boundary condition. Each element has an individual mechanical property EI, which is elaborated in the next section. The FEM modeling is coded in C++ and the associated beam model is solved using ABAQUS, B21 beam with active $Nlgeom$.

3.2.4 Flexural Rigidity Distribution

Cardiovascular devices have different mechanical properties, designs, and geometries to achieve specific tasks. The local flexural rigidity of guidewires varies along the its length. Clinical performance, i.e., steerability, torquability, penetration, deliverability, and safety, depends on the mechanical property profile over the length [144]. It needs lower flexural rigidity at the distal tip while higher rigidity is desired toward the proximal end.

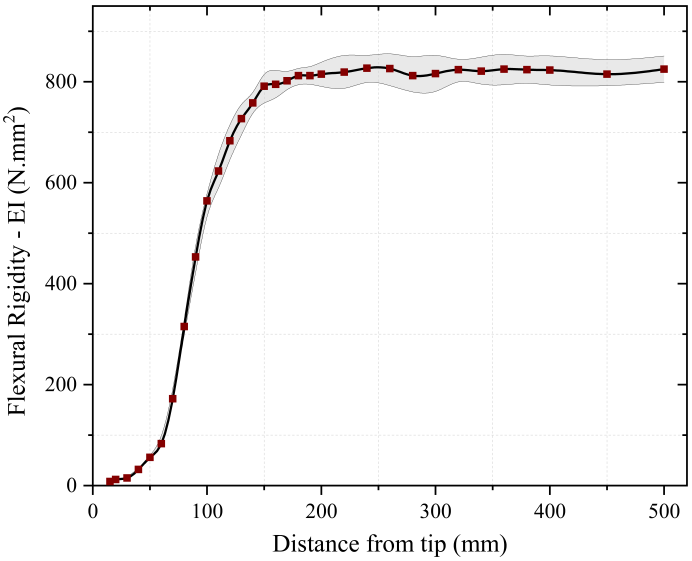

Figure 20: Flexural rigidity distribution of the guidewire based on distance from distal tip. Average value and deviation are shown.

The flexural rigidity distribution is measured through sequential three-point bending tests, Fig. 19, along the length as presented in [134]. The bending modulus is proportional to the fourth power of the radius, so a slight change in radius can greatly affect the accuracy of bending modulus measurements, consequently force estimation. Hence, we aim to determine and utilize EI instead of E. Fig. 20 shows the flexural rigidity distribution of a Zipwire^{TM} Stiff guidewire (Boston Scientific, USA) measured as a function of length from the tip, $EI(s)$. To do so, sequential three-point bending tests were performed over 0 - 500 mm distal end at increments of 10 mm (over 0 - 200mm), 20 mm (over 200 - 400 mm) and 50 mm (over 400 - 500 mm). We used a Bose® Electroforce 3200 dynamic testing machine (Bose Corp., Massachusetts, US). The support span length was 30 mm, and loading speed of the machine was fixed at 20 $mm.min^{-1}$ to eliminate any potential dynamic effect. Each test was repeated three times, and the average value and standard deviation were computed. Rigidity changes sharply within 15 cm of the distal tip and stays consistent beyond it. In the model creation, the algorithm measures element lengths from the tip and assigns individual mechanical properties to the elements based on the rigidity graph (see algorithm 3

lines 9 - 11).

3.3 Experimental Platform and Study Protocol

3.3.1 Experimental Setup

The setup has a transparent, realistic, anthropomorphic training phantom (fabricated from Acrylic glass and transparent) representing the aortic arch and extended carotid structure with normal configuration (Fig. 21). A camera is mounted above the phantom to provide image feedback for force estimation and also operator visual guidance. A robotic platform is designed to remotely navigate the guidewire (Fig. 21 (b)). The robotic driver (slave) is controlled by the operator (master) using a keyboard/joystick to command the manipulation procedure. A Zipwire^{TM} Stiff guidewire with angled tip shape is used with no support catheter. The operator performs navigation under image-guidance using a live gray-scale image simulating 2D fluoroscopy projected on a monitor, i.e. the constant transformation of camera image to a real-time gray scale frame stream. It is a general case study of any non-steerable catheter or guidewire navigation through cardiovascular anatomy.

Part of the aim of this paper is to study and compare the total force exerted on the vasculature, i.e., the insertion force in our setup, with intraluminal interaction contact forces. To do so, the phantom is mounted on a six-axis force-torque (F/T) sensor as shown in Fig. 21 (d) (Mini40; ATI Industrial Automation, Inc, Apex, NC). The setup provides force measurement in the X, Y and Z directions. The phantom is placed on its gravity center to hinder tilting or vibration during the procedure. The force sensor platform and phantom are isolated from any other support or contact, so that the force measurement corresponds to the resultant catheter-vessel force vector. The F/T sensor readings are obtained through a Data Acquisition system (National Instrument DAQ) using a software which records data at 60 Hz and computes resultant magnitudes of

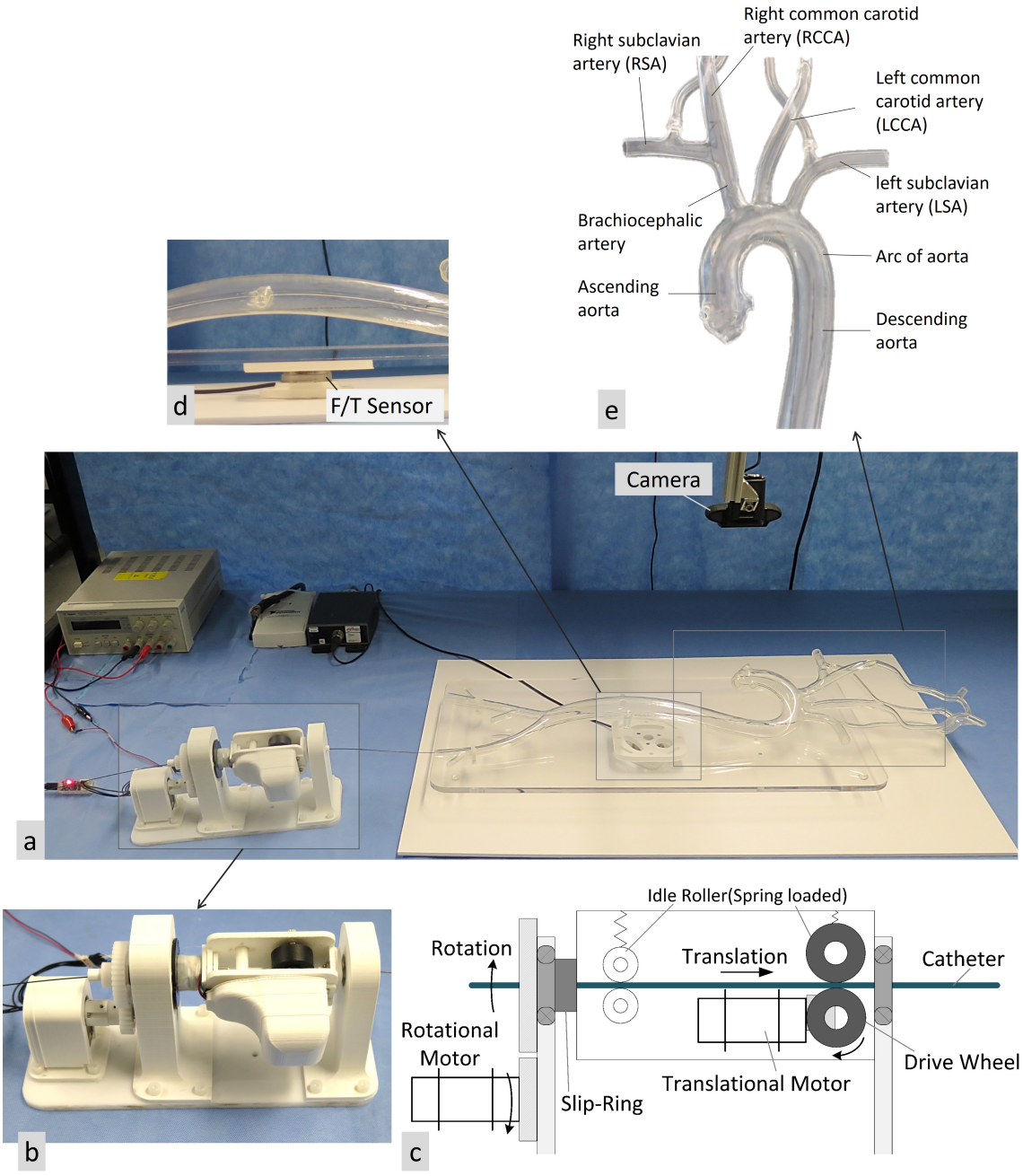

Figure 21: Experimental setup used for force monitoring tests (a) depicting robotic catheter drive (b), schematic design (c), force measurement platform by F/T sensor (d), aortic arteries (e).

the 3D force measurements. Measurements are zeroed at the very beginning of each test to omit the weight of the phantom or any undesired load. Also, phantom is not perfused which would not affect the proposed method evaluation. However, the fluid

dynamic effect of blood in clinical condition might need be considered where such effect would be minimal in case of extreme deflection as tool is firmly supported by contact points.

Robotic Navigation System: A robotic driver system is designed based on the methods in conventional manual navigation of non-steerable catheters/guidewire, i.e., techniques similar to the push, pull, and twist. The design (Fig. 21 (c)) has two degrees of freedom as of insertion and rotation similar to the designs in [9]. It consists of a translational driver unit mounted on a slip-ring gantry, which allows the rotational motion of the catheter simultaneous to insertion motion. Simultaneous rotation-insertion motion is a acquired skill in manual manipulation that is featured in the proposed robotic system. The design includes two servomotors (Dynamixel XH430 series, ROBOTIS, CA, US) under velocity control law based on a PID controller. Catheter translation motion is achieved by a fractional drive wheel and a secondary spring-loaded idler roller coupled opposite-side of the drive wheel to guarantee sufficient frictional force. The second motor rotates the whole translation unit on a housing gantry equipped with a slip-ring. It allows unlimited rotation of catheter to facilitate maneuverability.

3.3.2 Study Protocol and Data Analysis

One operator performed remote robotic navigation of the guidewire through supra-aortic vessels, including the right subclavian artery (RSA), the right common carotid artery (RCCA), the left common carotid artery (LCCA) and the left subclavian artery (LSA), see Fig. 21 (e). Cannulations were repeated five times for each targeted artery. The position and length of contact interactions are obtained from image segmentation along with the CF estimation results from the FEM model to visualize CF monitoring on vessel boundaries. Resultant insertion forces on the phantom are recorded with the F/T sensor. The quantitative analysis is performed on the parameters of intraluminal

CF and resultant forces, including: average of peak force, standard deviation (STD) of peak force, average of mean force, force-time impact (force integral over time). The FEM estimation error is analyzed based on GW deformed shape estimation, i.e., planar distance between actual GW and the simulated results. If (h_i, q_i) represent coordinates of each points on the actual shape and (H_i, Q_i) as the coordinates of points from the FEM model, then the estimation error (E_P) is expressed by

$$E_P = \sqrt{(h_i - H_i)^2) + (q_i - Q_i)^2)} \tag{15}$$

The structural stress of the GW is obtained from the FEM model. It results in an intraluminal stress study during navigation.

3.4 Results and Discussion

3.4.1 Intraluminal Contact Forces

Fig. 22 depicts an example of guidewire FEM model and simulated results at a given time during cannulation of RCCA. Subfigure (a) presents the FEM model structure: the guidewire beam model (meshed in red), deflection vector d_i which is applied to boundary condition BC_i, the simulated guidewire in blue contour highlighting reaction forces, direction and magnitudes of four local contact force vectors and the contact positions on the vessel wall. In this example, contact forces are: $|\vec{f_1}| = 0.17\,N$, $|\vec{f_2}| = 0.26\,N$, $|\vec{f_3}| = 0.09\,N$, $|\vec{f_4}| = 0.03\,N$. Contact forces closer to the distal end ($\vec{f_3}$ and $\vec{f_4}$) are significantly lower than $\vec{f_1}$ and $\vec{f_2}$ which is due to lower GW flexural rigidity in that region. Fig. 22 (b) compares modeling results represented as green dots to the actual GW shape from image segmentation in blue curve. A visual comparison suggests that the model mimics the GW behavior.

Fig. 23 displays a graph tracking local CFs during navigation of the RCCA. At the

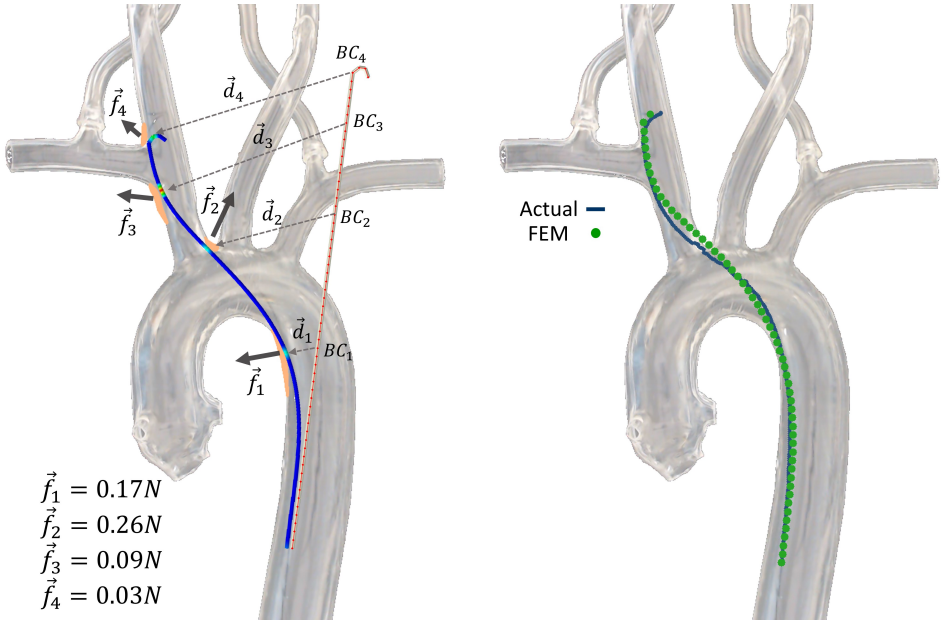

(a) (b)

Figure 22: FEM model of GW at a given time: meshed beam model, boundary conditions, deflection vectors, simulated shape and estimated CF vectors applied to the vessel wall (a), actual GW from imaging compared to FEM modeling (b).

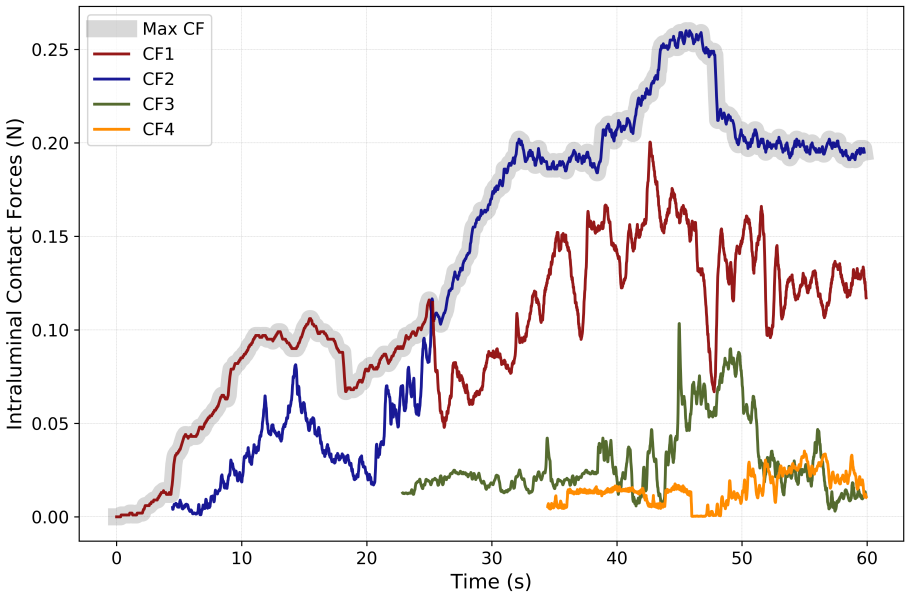

Figure 23: Example of image-based intraluminal contact forces monitoring for every local contact points through RCCA navigation. CF_4 to CF_1 are named from the distal tip toward the proximal end.

beginning of the procedure, the GW has only one contact, and the number of contacts is increasing to four as GW is advancing. The maximal ranges of CF_3 and CF_4 are $0.04\,N$ - $0.11\,N$ whereas the ranges of CF_1 and CF_2 are about $0.205\,N$ - $0.26\,N$. The ascending trend is seen for all CF values, but CF_1 and CF_2 forces increase to larger values. This is because the CF_1 and CF_2 positions are moving away from the tip over insertion which gradually shifts contact to the stiffer regions, whereas CF_3 and CF_4 are just happening at the softer regions close to the tip. CF magnitudes are fluctuating because of the GW slip-stick motion on the phantom wall.

Maximal intraluminal CF, as the main safety performance metric in interventional procedures, is highlighted on a gray shadow in Fig. 23. Maximal CF was on CF_1 and turns to CF_2 after the guidewire gets in contact with more points and is being highly deflected at the middle region (see Fig. 23 where CF_3 starts). It was observed that every procedure has a unique CF monitoring trend; however, maximal contact forces were always happening on contact points far from the tip rather than near.

A map of CF on vessel interaction boundaries over the time of the procedure is presented in Fig. 24 (results are for the same trial presented in Fig. 23). CF magnitudes are color-coded on their coordinate of interaction. The guidewire continuously interacts with the inner lumen arterial wall in which some parts of the wall get in contact several times. Maximum CF is visualized cases where several interactions occur on a part of the lumen. The path of interactions starts from both side of the descending aorta, gets to the aortic arch bifurcations and moves into RCCA where it mainly interacts with the right side of RCCA. Maximal contact forces are localized at the bifurcation edge of RCCA in the aortic arch, about $0.26\,N$, and downward in the right side of the descending aorta, about $0.2\,N$. This is due to the large deflection induced on the GW at those regions and also the guidewire's high rigidity modulus.

Fig. 25 depicts CF contour map of RSA, LCCA, and LSA cannulation. In these examples maximum CFs are $0.31\,N$, $0.08\,N$ and $0.11\,N$ for RSA, LCCA and LSA,

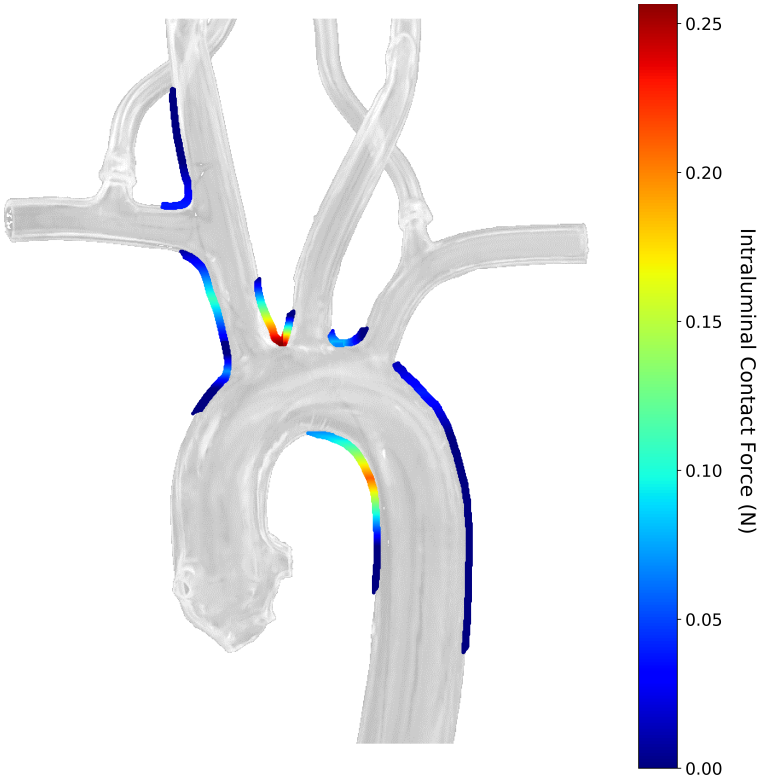

Figure 24: Guidewire-vessel interactions and intraluminal contact forces map computed during navigation of RCCA.

respectively. Observing the CF contours suggest that maximal CF in the procedures mainly happens at the bifurcation edges, where the guidewire path changes, and it is being forced to bend by the edge wall while advancing. In other words, the bifurcation edge wall acts as a support for the GW. Additionally, guidewire sticking to the phantom wall leads to more friction forces and consequently, more push force and CF. RSA contours looks similar to RCCA in terms of magnitudes and maximal CF locations on the vessels. This is because of common navigation procedure up to RCCA-RSA bifurcation, which consequently results in similar GW motion and interactions map.

Table 4 shows intraluminal contact force metrics in all cannulation experiments. Cannulation of RCCA and RSA are associated with higher contact forces compared with LCCA and LSA, since these procedures are more dexterous and engage a longer

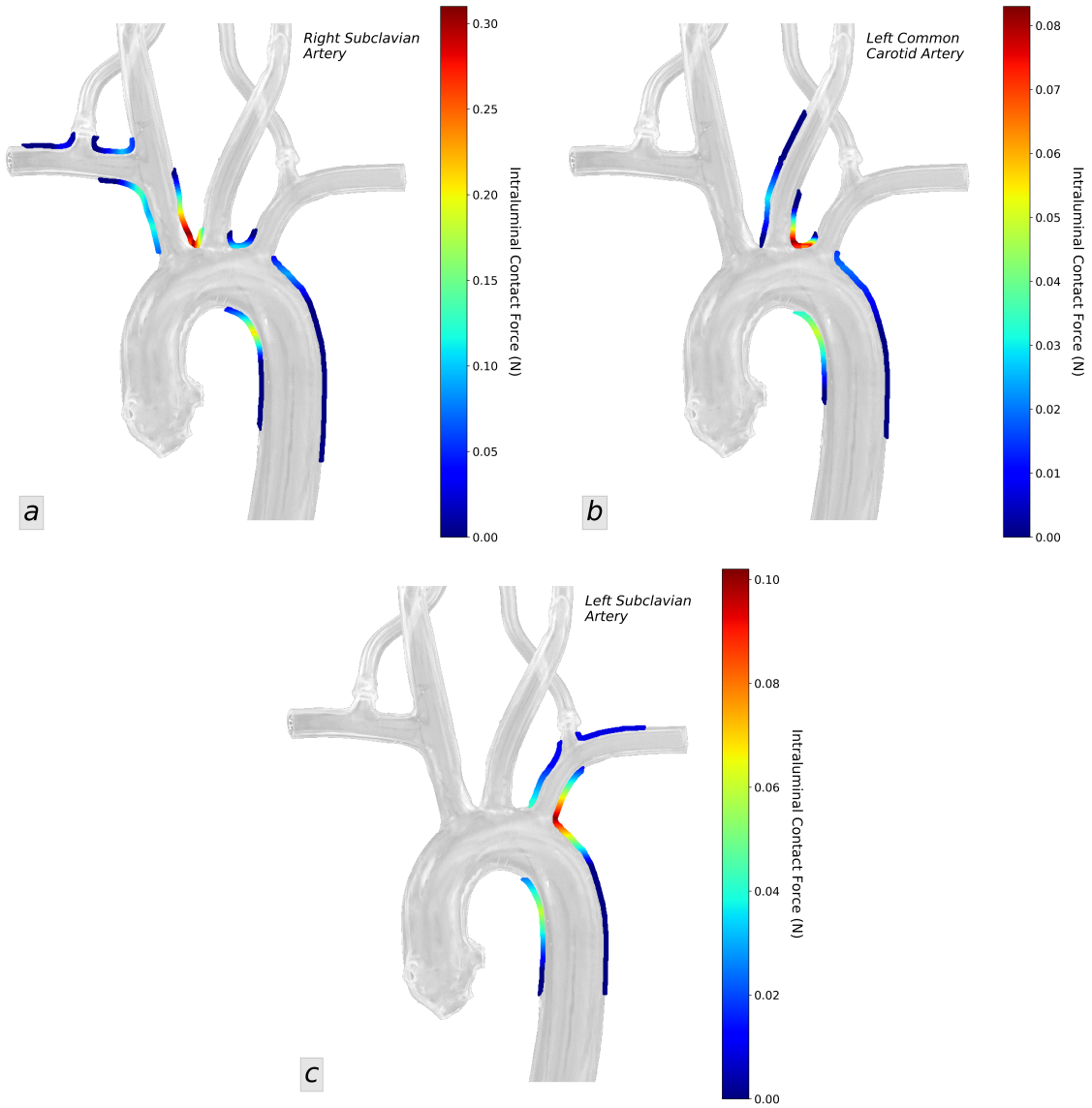

Figure 25: Intraluminal contact force monitoring results showing magnitude and position of applied forces on arterial wall through cannulation of Right Subclavian Artery (a), Left Common Carotid Artery (b), Left Subclavian Artery (c) (force scales are different in sub-figures).

portion of GW with larger deflections and larger friction forces. The highest CF peak up to $0.37\,N$ was observed in RSA cannulation. Average of peak CFs were $0.24\,N$, $0.305\,N$, $0.092\,N$ and $0.114\,N$ at RCCA, RSA, LCCA and LSA respectively and average of mean CF were $0.14\,N$, $0.172\,N$, $0.041\,N$ and $0.046\,N$. The standard deviation of peak CF was from $0.021\,N$ to $0.053\,N$ showing a big variation over trials.

Table 4: Mean values for computationally predicted intraluminal contact force and measured resultant force.

	RCCA	RSA	LCCA	LSA
Intraluminal Contact Forces				
Average Max CF (N)	0.24	0.305	0.092	0.114
STD Max CF (N)	0.053	0.046	0.021	0.026
Average Mean CF (N)	0.142	0.172	0.041	0.046
Average F-T Integration (N.s)	8.57	9.85	1.23	1.17
Resultant Force				
Average Max force (N)	0.291	0.321	0.074	0.081
STD Max CF (N)	0.082	0.104	0.034	0.038
Average Mean force (N)	0.078	0.093	0.031	0.035
Average F-T Integration (N.s)	4.75	6.45	1.06	0.875

It infers that not all procedures have small CF, but some may cause damage to arterial cells. Force time integration or force impact is a performance metric for quality of the procedure; a lower value indicates faster procedures with lower CF, i.e., the best desired scenario. Force impact was from $1.17\,N.s$ at LSA up to $9.85\,N.s$ at RSA. The higher value of CF and longer time of cannulation to reach the targeted point in RSA and RCCA resulted in significantly greater Force-Time integration $(N.s)$.

3.4.2 Estimation Error

A validation of the proposed method showing accuracy and effectiveness in multi-point force estimations were performed in a earlier study [134]. It suggested that a smaller error in force estimation was associated with a smaller shape simulation error. In this study, direct intravascular force measurement is not possible, thus the performance evaluation is conducted based on shape estimation error by comparing actual GW deflected shape and FEM simulation. Table 5 includes maximum and average root-mean-square-errors in shape estimation along with GW lengths values and average applied deflections in contact points. The estimation error is defined in

Table 5: Model accuracy based on shape estimation error along with GW lengths and deflections.

	RCCA	RSA	LCCA	LSA
Max length (mm)	314	332	257	193
Mean length (mm)	211	224	176	124
Mean deflection (mm)	63	75	51	42
FEM Estimation Error (E_p)				
$RMSE_u\,(mm)$	2.2	3.1	1.8	1.3
$MAXE_u\,(mm)$	4.3	5.7	3.2	2.4

Eq. 15. Within all arteries, maximal errors are $4.3\,mm$ and $5.7\,mm$ for the RCCA and RSA cases, respectively, where the maximum GW lengths are $314\,mm$ and $332\,mm$. Average applied deflections are between $42\,mm$ and $75\,mm$ within the arteries. The estimation error is higher for scenarios with larger deflection.

3.4.3 Resultant Exerted Forces

Some studies proposed the measurement of total catheter/GW insertion forces or total contact forces applied on a phantom for either contact force evaluation or insertion force control [41, 132]. Total catheter insertion force does not represent the local CF applied on the inner arterial wall, while it is likely to be the resultant of intraluminal CFs plus unknown friction forces from introducer sheet, access point, etc. Here, we are comparing maximal intraluminal CF with resultant exerted force (RF) on the phantom recorded by the F/T sensor platform. Fig. 26 shows samples of force comparisons within arteries. There is no consistent trend; the maximal intraluminal CF is higher or lower than RF; however, in the majority of times, intraluminal CF is larger. RF may fall through procedure while CF remains large. It also suggests that RF is not a promising indication of complications since it is not as high as the CF, and their peaks do not match. Table 4 includes intraluminal CF and RF metrics. Max RF values may be higher compared to max CF, whereas mean RF is always showing lower

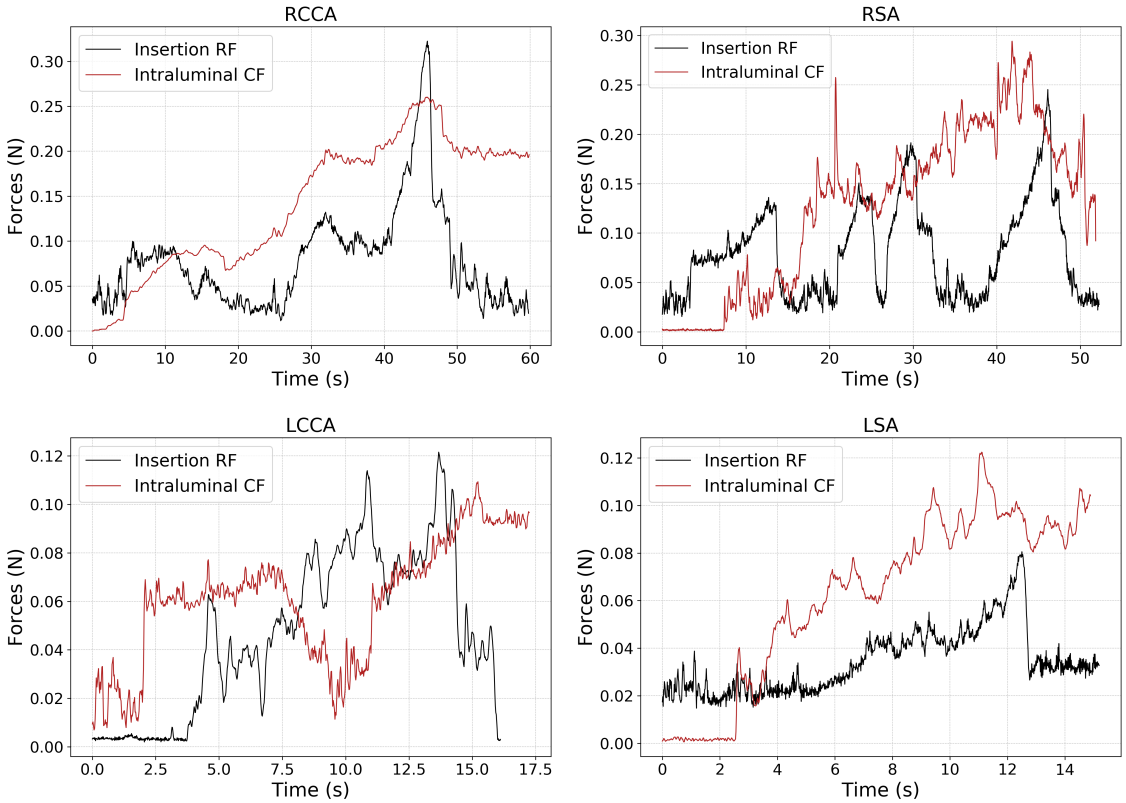

Figure 26: Total force exerted on the phantom, RF, is compared with maximum local intraluminal CF in cannulation of arteries.

values. This means that low catheter/GW insertion force could increase deflection gradually, which may lead to a high intraluminal CF with a risk of arterial wall injury. Monitoring and controlling RF, or insertion force, might smoothen the procedure, but it does not necessarily prevent excessive CF and subsequent complications.

3.4.4 Stress

In the proposed method, we can extract stress and strain from the GW/catheter FEM model at any instant of time. Guidewire material is linear, i.e., elastic strains. Fig. 27 presents samples of GW stress contour in arteries. Using intraluminal information, GW structure can be optimized to maximize navigation performance while minimizing CF and stress.

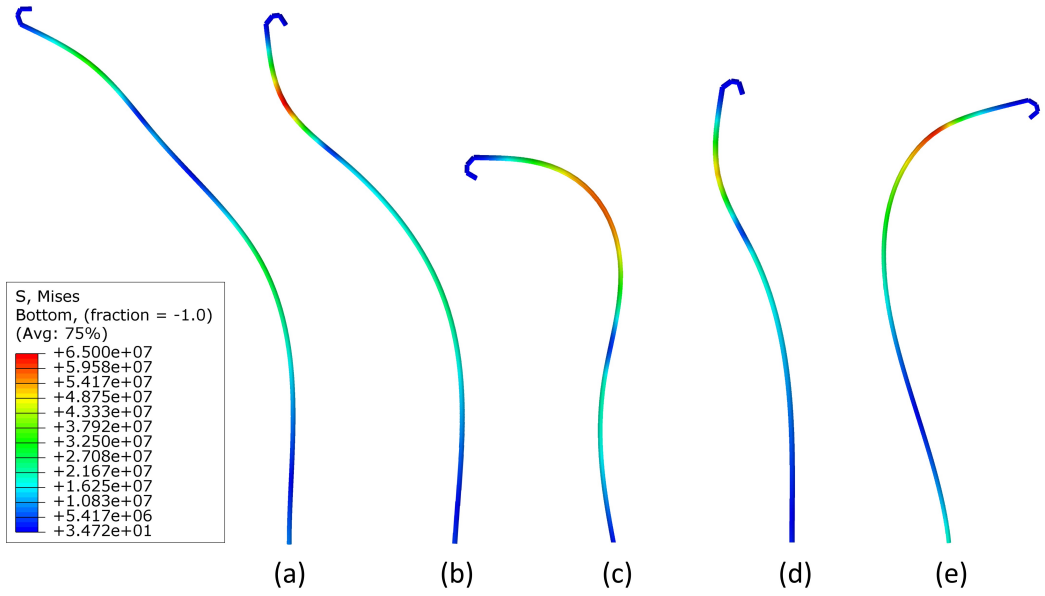

Figure 27: Stress estimation of GW during cannulation of arteries, RSA (a), RCCA (b), aortic arch (c), LCCA (d), LSA (e).

3.4.5 Discussion and Limitations

The observed errors in estimation could be due to measurement error in GW bending modulus over its length. Sharp changes in flexural rigidity may not be appropriately seen in sequential experiments. However, manufacturers have bending information based on their design, which can be used if such information is provided. Another error source is that the GW model is initially considered as a straight cantilever, whereas small deflection of the structure is observed for high initial lengths. The accuracy of force monitoring varies depending on the correctness of image segmentation as well, but is not sensitive to it. Camera calibration could cause such errors in this study, which may not be an issue in commercially available clinical imaging systems.

The proposed force estimation does not require information on arterial wall material properties and tissue deflections, which is considered an advantage; however, having that information would help to estimate local pressure profile on contact. It is almost certain that a distributed contact may happen but it should result in a wider contact

area, which produces lower pressure and risk. In this study, the amount of force, deflection, stress, and other parameters are reported for navigation of a GW in a training phantom, therefore, they are not necessarily as the same magnitude as in clinical practice, and such conclusion should not be made.

3.5 Conclusion

Tool-vasculature interaction was reported to be the leading cause of complications and major concern, such as embolization, stroke, ischaemic lesion, and perforation, in endovascular interventions. In this study, the case of catheter contact point forces is of interest, as it is the extreme condition with a high risk of over-pressure on the vasculature. We implemented an image-based intraluminal catheter-vessel interaction monitoring tool based on imaging data and numerical computation. The image segmentation algorithms successfully detect and track contacts, vasculature boundaries, catheter and compute needed pose measurements. The FEM model effectively simulates manipulation and predicts contact forces and structural stress. Remote cannulation of the aortic arteries was performed using a robotic unit and intraluminal contact force monitoring was achieved by tracking local CFs and building a contour map of CF on the arterial wall. Results suggest that RCCA and RSA associated with higher CF where maximal CF happens at the bifurcation edge of the aortic arch. The estimation error was low, showing the fidelity of the model. Contact forces can be visualized intraoperatively for clinicians to prevent injuries and reduce the learning curve for novices. CF could be used by the robotic system as a feedback for restrained force control. Resultant forces exerted on the vascular phantom is directly measured and compared with local CF trend, where small RF and catheter insertion forces could be detected while ICF was large on the vessel wall. The model can predict structural stress of a GW besides CF data in practice, which can help

to research and optimize the design of interventional tools. Nearly all cardiovascular procedures are under 2D real-time imaging. Physicians keep the imaging plane tangent to catheter motion, which we have simulated experimentally in this study. Extending the proposed methodology to 3D is an intuitive step that requires an upgrade to a 3D imaging platform and 3D FEM modeling. The proposed method can be further implemented on other types of interventional devices and cardiovascular procedures.

Chapter 4

Automated Endovascular Insertion Limiting Intraluminal Contact Force via Image-based Control

Under controlled tool-tissue interaction is the leading cause of complications and risks in endovascular interventions. Clinicians have little understanding of intraluminal interactions taking place through the length of endovascular tools as well as limited control over them. Manually derived vascular robotic systems have not achieved control of the intraluminal contact forces (ICF). This paper tackles the issue through a semi-automated vascular robotic framework to control tool-tissue interaction forces under a prescribed safe reference while advancing the navigation procedure. The proposed system is composed of ICF control and visual servoing. A force control-based catheterization performs regulated tool insertion based on image-based ICF sensing. An automated retraction-reinsertion feature employs visual servoing of the tip to ease the excessive ICF and extreme deflection caused by the gradual build-up of wall friction forces. The automated method was tested within a realistic simulation environment in robotic cannulation of aortic arteries and assessed compared to two

manual teleoperation modes: with visually ICF monitoring, and without access to ICF data. Automated force control-based catheterization has successfully limited all interaction forces under a safe range while advancing a guidewire to complete the procedure through autonomous retraction-reinsertion. Smoother motion, reduced ICF, and decreased workload has been achieved by automated robotic control. Employing the visual ICF monitoring system in manual teleoperation has shown improvement in force and motion metrics but not well as the automated technique. Tool-tissue ICF control can potentially improve the quality of endovascular navigation and minimize intraprocedural and post-treatment complications and risks of vessel wall damage.

4.1 Introduction

Medical robotic systems continue to embrace and integrate advancements to become more featured, intelligent, and adapted for specific needs and treatments. Magellan System (Hansen Medical, Mountain View, CA, USA) and CorPath GRX system (Corindus Vascular Robotics, MA, USA) are within commercial robotic-assisted intervention systems developed for peripheral vascular and percutaneous coronary interventions (PCI) receptively. Teleoperated endovascular robotic intervention offers advantages including significant reduction in radiation exposure (operator shields from X-ray radiation), precise positioning, sub-millimeter measurements, increased stability, controllability, and added comfort in a seated cockpit control unit. As an example, recent clinical evidence in robotic PCI demonstrates the feasibility and safety including 99.1% clinical success in complex coronary lesion cases [29], 95% reduction in radiation exposure to primary operator [20] and 20% to patient compared to manual [30], as well as significant reduction in measurement errors and need for extra stent [31].

Despite all the progress in vascular robotics, the control of interactions with anatomy through the entire tool shape, i.e., not just the tip but also side forces, is still

unsolved [145]. Clinical studies show that perforation, embolization, dissection, and thrombosis are among several complications due to endovascular tool interaction with the arterial wall [11, 56]. Fig. 28 shows computed tomography images of perforation and dissection in aortic arteries intervention. In the treatment of atherosclerosis (i.e., thickening of arteries due to build-up of fatty deposits that form a hardened plaque), the excessive pressure on vascular wires and catheter and applying higher force to cross highly calcified lesions may cause vessel perforation and significantly raises other complications' likelihood [57, 58]. Furthermore, intraprocedural stroke and post-treatment ischemia brain lesions are still significant risks in endovascular carotid artery intervention and stenting [59, 60].

Studies concerning catheter-tissue interaction (contact force measurements and control) are mainly limited to the single point force at the tip of steerable electrophysiology catheters for heart arrhythmia treatment, whereas dangerous contacts may also occur along the length of the catheter body [56, 145]. Recent research has developed a force regulation system combined with 3D ultrasound imaging and visual servoing to maintain catheter tip force level through compensating the motion of heart tissue [104]. Other studies investigated the modeling and control of ablation contact forces using estimation methods based on catheter shape analysis [90, 110].

Researchers also targeted catheter proximal forces sensing as an alternative solution to develop either force control-based robotic insertion [41, 42] or haptic and tactile feedback systems to recreate insertion force from the intervention devices [49, 115, 146–149]. Fuzzy control algorithms based on guidewire insertion force were investigated to increase safety and precise positioning [44]. A hybrid impedance control scheme was implemented on a 7-DoF robot enabled with proximal sensing to perform simultaneous force/position control for driving the catheter [42]. Further studies moved toward automated catheter delivery systems using image guidance, active steering, and proximal sensing feedback [41]. However, the proximal driving force is the sum of all

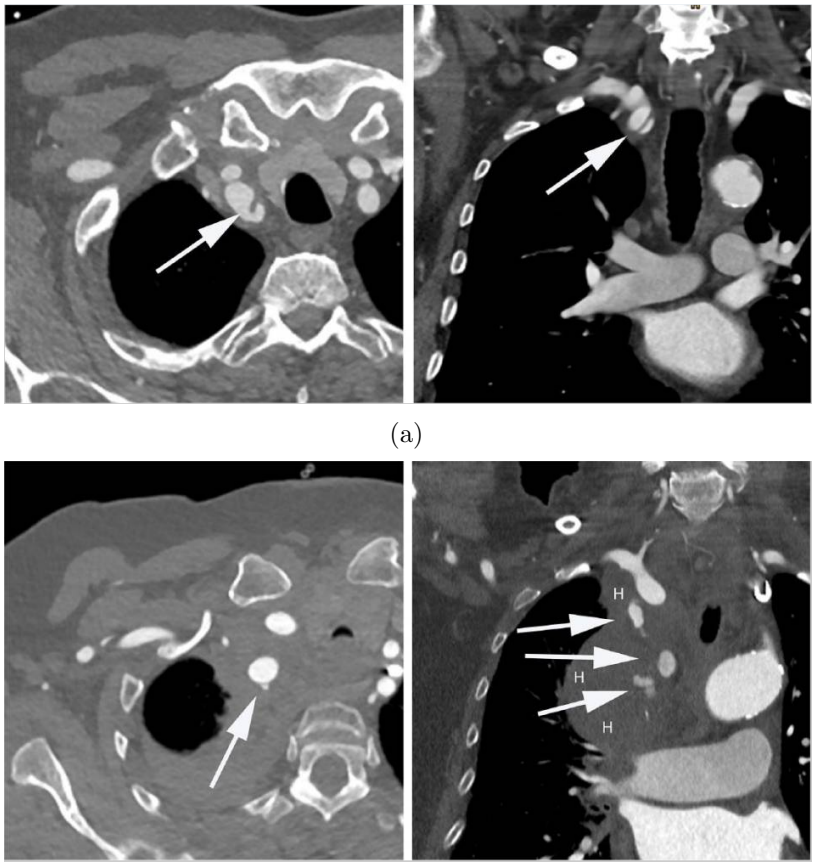

(a)

(b)

Figure 28: Examples of perforation and dissection in aortic arteries intervention (a) computed tomography showing dissection of the brachiocephalic trunk, (b) computed tomography showing perforation of the right subclavian artery [11].

catheter-vasculature collision forces plus the friction of introducer sheath and other vascular devices, in which sensing cannot distinguish intraluminal contact force (CF) at a local interaction point. Controlling the total driving force can make the procedure smoother, more stable, and continuous, but may not necessarily guarantee a safe interaction with lower local intraluminal CF. However, local intraluminal interaction of common non-steerable guidewires and catheters through the entire length of contact drew less attention due to a lack of measurement tools and complexity of controlling such highly nonlinear under-actuated system. Some other recent studies have looked into enabling automated robotic catheterization using learning-based techniques based on catheter motion trajectory from expert demonstration, reinforcement learning, and

imitation learning [36, 45–48], which resulted in a reduction in the direct force exerted on the vascular model. Other studies suggest reduction in total contact forces exerted on vascular using robotic system with steerable catheters compared to conventional catheterization [145]. Although a reduction in exerted force on the vasculature, i.e., resultant of all CFs, suggests an improvement in the navigation procedure [133], our recent investigation showed that large intraluminal point CF may occur on the arterial wall even at small total CF exerted on the vascular phantom [150].

The above described issues have led us to investigate measuring intraluminal contact point forces using image-based estimations and automating robotic insertion to maintain local contact forces in a safe range based on the image-based sensing feedback. In previous works [134, 150], we presented an image-based contact force estimation approach using the continuous numerical modeling of the catheter and delivered an intraluminal CF monitoring system for the entire length of catheter-tissue interaction.

This paper proposes an automated approach to drive the tool insertion and control the maximal local contact forces, and consequently keep all interaction forces in a prescribed safe limit. Features of the proposed semi-automated cooperative robotic method are described as follow:

- A human-robot shared control where the operator controls the rotation and commands the insertion while the robot automatically regulates the insertion speed, stops the procedure, and performs automated retraction-reinsertion trials to limit the interaction forces in a safe range.
- A cascade velocity actuated force controller system based on the image-based intraluminal contact force sensing feedback that actively adjusts catheter insertion speed for optimal response to sudden change/peaks in interaction forces.
- An automated catheter retraction based on the tip visual servoing relaxes excessive jammed tool deflections and the associated contact force to allow

reinsertion at lower force levels.

The proposed automated technique implemented in our experimental robotic-assisted vascular intervention platform, which includes a 2 DOF vascular robotic drive, an anthropomorphic aortic arch phantom, a 6 DOF torque/force sensing coupled on the phantom, and a camera. The teleoperated framework allows the operator to remotely perform navigation tasks under visual guidance, which is the same image feedback used for contact force and tip position sensing. The proposed automated cooperative teleoperated framework is validated through a set of experiments in cannulation of aortic arteries, in which they are compared with manual teleoperation using the intraluminal contact force monitoring system [150] and traditional teleoperation. The effectiveness of employing the intraluminal CF data into a monitoring system for the operator's visual guidance is also investigated compared to traditional operations. The quality of the procedures are further assessed by comparing performance metrics of distal tip trajectory, intraluminal contact forces, and applied forces on vasculature phantom.

Results suggest the effectiveness of the proposed cooperative framework to achieve safe and efficient intervention as well as the following contributions:

- The proposed robotic approach based on the CF controller and automated tip retractions achieves controlling catheter-arterial wall interactions within a safe prescribed force limit, which significantly reduces the risk of complications such as perforation and dissection, stroke, and brain lesion.
- The proposed method is able to finish the intervention tasks successfully where the safe limit is feasible based on tool properties and targeted anatomy.
- It is observed that jerky and slip/stick motion is more likely where the catheter is largely deflected and CF is high, in which the controller has engaged in regulating insertion speed and smoothening such motion.

- Comparative experiments demonstrate the efficacy of the proposed robotic method with smoother catheter path, reduced intraluminal and vasculature exerted forces, and reduced operator workload.
- We show that intraluminal force data integrated within a visual monitoring system guides the operator to avoid extreme CF peaks and achieves reduction in interaction forces as well as an enhanced smoothness of tip trajectory.

To the best of our knowledge, this work is the first reported attempt to perform robotic vascular intervention with an automated intraluminal contact force control to limit the entire interaction forces through the length of the catheter/guidewire. We have generalized the method for conventional vascular tool. In the manuscript "catheter" refers to any general type of non-steerable catheters and guidewires. The rest of paper is organized as follow: Section 4.2 explains the automated force control system and human robot shared control method; Section 4.3 describes the robotic vascular teleoperation framework; Section 4.4 presents the experimental results, comparison, limitation and discussion; Section 4.5 concludes the study.

4.2 Methods

4.2.1 Robotic Intraluminal Force Control-based Catheterization

Vascular tool interaction with the vessel wall may lead to aggressive contact force with the risk of serious complications, i.e., perforation, penetration, and dissection. Physicians try to avoid vessel injury by relying on visual 2D fluoroscopy guidance and tactile cues from the small driving force and torque sensing at the fingertip. The tactile sensing is also highly noisy due to friction of catheters and guidewires with introducer sheath, support, or guide catheters. Accordingly, interventionists have

little understanding of the intraluminal interaction taking place. While the operator performs manipulation to attain a targeted artery, pass tortuous anatomy, or cross a blocked vessel, the chance of complication increases as interaction contact forces are rising.

The robotic intraluminal force control-based catheterization (RIFCC) attempts to drive the tool while maintaining supervisory control on all intraluminal contact point forces through the vessel interactions. RIFCC aims to restrict contact force in the safe range to prevent complications with manual robotic teleoperation due to uncontrolled CF. The image-based contact force estimation, as presented in previous works [134, 150] provides intraluminal contact force feedback for the robotic system. The estimation is based on a nonlinear finite element catheter model developed using image-based data. The deflected pose is extracted from real-time imaging and catheter deflections fed to the inverse FEM model to compute the CFs. Proposed RIFCC uses a contact force controller, which regulates the catheter driving based on intraluminal CF feedback. The force controller updates the catheter insertion speed to damp peak forces and maintains CF safely, preventing jerky motion and slip-stick condition, i.e., increased smoothness. Since the force controller drives the catheter, not the operator, it responds fast to an increase in CF due to longitudinal friction build-up and excessive deflections. The controller also decreases the insertion speed as the CF trend increases to let the catheter slide rather than stick to the wall. This may minimize the chance of vessel injury and complications. On the other hand, lower contact forces result in higher insertion velocity to save operation time. By reducing the operation time, a lower dose of contrast agent is needed, and less X-Ray exposure is given to clinicians and patient. The controller is more engaged as ICF is getting close to the max safe ICF threshold; otherwise, the operator can adjust the insertion maximum speed as desired for navigation purposes. There is more than one contact point force through the length of catheter interaction, in which the maximal ICF point is fed to the control

loop as feedback.

RIFCC works on the linear translation of the catheter to achieve the desired goal. Once the controller reaches the maximal safe ICF limit, the system switches to an automatic catheter retraction (ACR) step. ACR retracts the tip using visual tracking, and it eases excessive contact forces caused by extreme deflections through relaxing the catheter body. Without the retraction step, the force controller slightly oscillates over the CF safe threshold and cause the navigation procedure to get stuck and stay in a risky condition. During the retraction-reinsertion procedure, a small amplitude proximal wiggling is added to the catheter motion as an intentional disturbance to reduce the coaxial friction. This approach has been learned from clinical expert reasoning in manually navigated cases. When resistance to insertion met or a chance of damage is raised, the physician retracts the catheter and may rotate or wiggle to achieve smoother and safer reinsertion through the relaxed bulking, deformation, and frictional forces on the device. ACR employs visual servoing of the catheter tip position to a pre-defined displacement target. Vision sensing provides position feedback through the image segmentation and tracking methods presented in [134, 150]. Retracting the distal tip ensures relaxing deflections since the whole body of catheter should retract before the tip moves.

4.2.2 Insertion Model

Let us describe the dynamics of catheter insertion as a simplified model presented in Fig. 29. A linear robotic drive pushes a cart attached to the catheter proximal end in one single direction, while other directions are constrained. Elastic beams represent the catheter's sections, connecting contact points to the cart and the other contact points. Angular springs are placed at the beams' revolute joint, which makes bending moment between catheter's sections. Each beam has its own nonlinear bending stiffness, which is a function of the beam's deformed state. Weightless elements with frictional contact

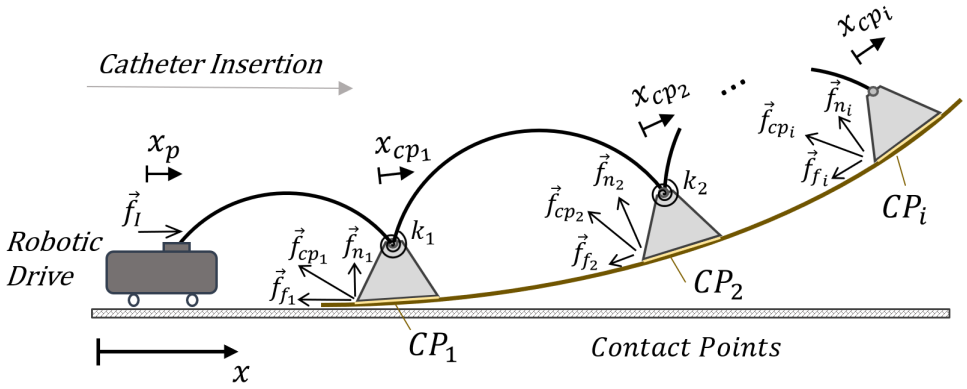

Figure 29: Schematic model of intervention tool insertion includes elastic nonlinear beams between contact elements with frictional contacts on an uneven surface which would induce lateral deflection as of being inserted in the vasculature.

on the surface describe the contact points. The frictional coefficient, $\mu(x)$, is also nonlinear as a function of the path represented by the position x_{cp}. As the cart moves, beams are being deflected in axial directions, which results in the frictional force of f_{f_i} exerted to CP_i. The curved surface presents the vascular path, which induces the lateral deflection to the beam at the contact points, leading to a normal contact force of f_{n_i}. The resultant of f_{f_i} and f_{n_i} is the contact force f_{c_i}. We can describe catheter motion as the cart pushes the first beam and contact element, which consequently pushes the other beams and contact elements. The whole system moves as the beam deflection, frictional forces, and distance between contact elements could fluctuate to the nonlinearity.

In order to control interacting contact forces F_c, one solution would be to control a position reference $x|_{F_c=F_r}$ for which $F_c = F_r$ using the position control law [151]. However, in the case of catheter insertion with complex and nonlinear elastic parts, it is not possible to determine what position corresponds to the reference force F_r. Thus, the proposed solution is a velocity controller based on the force error, where a velocity is commanded to the manipulator in the direction that decreases the force

error. It uses the inverse damping law:

$$\dot{x}_p = b\ \Delta F \tag{16}$$

where $\Delta F = F_r - F_c$ and b is an accommodation gain. If we assume the condition that catheter contact force always increases with an increase in insertion position x_p, i.e., applying more deflection, then:

$$\frac{\partial F_c}{\partial x_p} = \kappa(x) \tag{17}$$

where $\kappa(x) > 0$ represents whole catheter insertion stiffness.

The sufficient condition for the force error to converge to zero is to have a system with $\gamma(x) > 0$ where:

$$\frac{d}{dt}(\Delta F) = -\gamma(x)\Delta F \tag{18}$$

In order to prove this condition in our system, the left side of Eq. 18 can be written as:

$$\frac{d}{dt}(\Delta F) = -\frac{\partial F_c}{\partial x}\dot{x} = -\kappa(x)\dot{x}, \tag{19}$$

considering $\Delta F = F_r - F_c$.

Substituting ΔF from 16 and equating 18 and 19 result in:

$$\kappa(x)\dot{x} = \gamma(x)b^{-1}\dot{x}_p \tag{20}$$

where $\dot{x} = \dot{x}_p$

$$\kappa(x) = \gamma(x)b^{-1} \tag{21}$$

choosing b as a positive value and considering the stability condition where $\kappa(x) > 0$, then

$$\gamma(x) > 0 \tag{22}$$

which proves force convergence based on inverse damping law of 16. A proof of stability of nonlinear stiffness contact controller based on force/velocity mapping, i.e., inverse of damping, is discussed in [151].

4.2.3 Control Methods

The control method aims to keep intraluminal contact forces in a safe range and respond fast to the procedure to prevent force over-shoot and overload in interactions. Catheter insertion potentially might be controlled based on an insertion force control law:

$$\vec{F}_I = \vec{F}_{c_d} + \sum \vec{F}_{c_i} + \vec{F}_{dst} + \vec{C\dot{x}} \tag{23}$$

where $\vec{F}_I$ is the insertion force, $\vec{F}_{c_d}$ is the desired max safe contact force, $\vec{F}_{c_i}$ are the other contact forces, $\vec{F}_{dst}$ are disturbance forces and $\vec{C\dot{x}}$ is the damping force. There are nonlinearity, disturbances, and damping in catheter insertion, which are hard to control. Thus, the robot driver force regulator, F_i, based on force error would not respond correctly to contact force tracking as the nonlinear dynamics of catheter prevent proper transmission control action to end effector, i.e., contact points.

A velocity actuated force controller is proposed, where the outer-loop is the force controller, which commands the catheter insertion velocity references in the direction that decreases the force error. The cascade design of the control system gives an improved response to disturbances. Let us assume two conditions where the frictional force and disturbance are significantly different, but the contact force error is the same, then the force controller output is giving an equal insertion velocity reference, in which the inner-loop velocity controller adjusts the effort needed to transmit action to the end effector. The cascade control arrangement isolates nonlinearity and friction to prevent the loop from becoming unstable or sluggish. Fig. 30 presents the architecture of the designed control system block diagram. Proximal insertion velocity controller, as the inner-loop, is nesting inside the contact force controller loop. The image-based

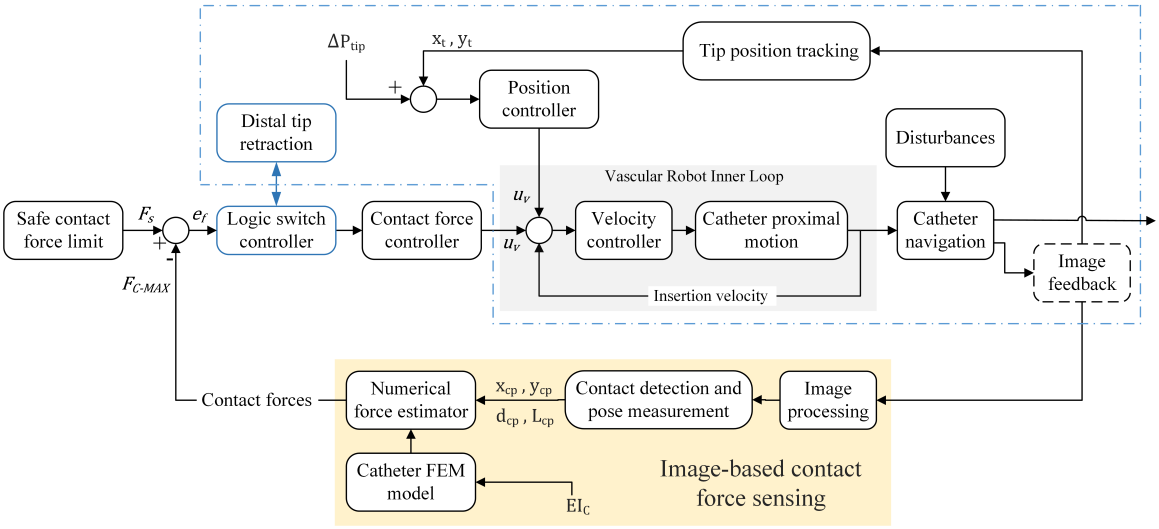

Figure 30: Control block diagram of the proposed system. Intraluminal contact force controller (lower loop) drives catheter in insertion and the tip position controller (upper loop) automatically retract tip to relax excessive CF.

contact force sensing block provides force feedback based on the sensor-less estimation method presented in [150]. A numerical force estimator computes contact forces using the catheter FEM model and pose measurements of contact point from the image processing. The force feedback is the maximal contact force ($F_{c_{max}}$) between all contact forces F_{c_i} through the length of interaction and its position changes during navigation. The desired force set point is the maximal prescribed safe force (F_s). Force controller does the driving procedure while regulating the insertion velocity set point based on the contact force error. The inner-loop controller sets the robot effort to meet the velocity setpoint based on the proximal insertion velocity feedback. As the catheter or guidewire navigates through the vasculature, the distal section interacts with the vessel wall, i.e., the plant. Plant image feedback closes the control loop. The velocity level loop responds quickly and considerably reduces the level of force fluctuations that could have occurred with the single loop force control system.

Retraction of the catheter based on a tip position controller is proposed once the maximum safe contact force is reached, i.e., the force error $e_f = 0$. This would prevent the oscillation of the contact force controller and its consequences in hitting

the vessel's wall and injuring it. A logic block switches the control scenario between the contact force controller, which does the insertion, and the catheter tip position controller, which automatically retracts the catheter. As explained, such system is proposed based on the fact that retracting catheter let the buckling, friction forces and significant catheter deflections relax and leads to smoother reinsertion. There is almost no chance for tool kinking as the safe limit is much smaller compare to kinking/buckling load. To do so, a minimal catheter tip retraction (ΔP_t) is enough because the whole catheter body axial deflection (buckling) would relax before the distal end retracts. We propose a velocity actuated position control strategy for tip translational motion as shown in the upper loop of Fig. 30. It is a cascade arrangement similar to contact force control for the same reasons of system limitation. Catheters' motion is a nonlinear system meaning that the tip translation is not proportional to the point of entry insertion. It is because of significant flexibility in the catheter and frictional forces acting along the length. The outer-loop controller commands proximal insertion velocity reference based on distal tip position feedback. Without the internal velocity control loop, the outer loop must be detuned as the catheter moves, and its boundary condition, deflections, and frictional forces are changing. Visual servoing technique is employed using position feedback extracted from the vision sensing. Tip desired position is

$$P_{t_d} = P_{t_{CF}} - \Delta P_t \tag{24}$$

where P_{t_d} is the desired tip position in retraction, $P_{t_{CF}}$ is tip position where max contact force happens and ΔP_t is a predefined retraction value based on navigation case conditions. Tip detection and tracking are based on catheter segmentation methods as described in previous studies [134, 150].

Classic closed-loop proportional-integral-derivative (PID) control algorithm is utilized to minimize the error between the desired and actual inputs. PID can effectively deal with nonlinear uncertain dynamic systems [152], such as the vascular

navigation process. The classic PID controller has control function of:

$$u(t) = k_p e(t) + k_i \int_0^t e(\tau) d(\tau) + k_d \dot{e}(t) \tag{25}$$

where e is the control error, defined by:

$$e(t) = y^* - y(t) \tag{26}$$

for any desired reference value $y^* \in \mathbb{R}$ and $y(t)$ parameter at the time instant t, and k_p, k_i, k_d are the control parameters to be designed. The contact force controller uses a PD controller without the integration term since the controller is designed to keep force lower than a limit rather than maintaining force on a desired value, the integral term should be avoided. A relatively high k_d parameter is designed for fast damping response to possible peak contact forces. This would smoothen contact forces high-frequency peaks, which are most difficult to be avoided in manual catheter insertion. Tip retraction position controller designed based on PID terms. The controller is designed for an aggressive fast retraction to save time. In the cascade structure, tuning the internal robot driver velocity controller should be performed in the primary step, and then tuning of the outer-loop controllers will been achieved. During the retraction-reinsertion loop the proximal wiggling is activated to add intentional disturbance aimed a lower friction force and less slip stick occurrence.

4.3 Experimental Setup and Hardware Design

The proposed framework is verified through the teleoperation catheterization experimental setup shown in Fig. 31, also presented in [150]. The operator conducts aortic artery cannulation tasks using the robotic catheter manipulator in a transparent, realistic, anthropomorphic training phantom. The camera provides image feedback for

force estimation, visual servoing, as well as operator visual guidance. Live gray-scale imaging is projected on a monitor to simulate the X-Ray fluoroscopy for the operator. A six-axis force/torque sensor capable of detecting force with a resolution of 5 millinewtons (Mini40; ATI Industrial Automation, Inc, Apex, NC) carries phantom to record total vascular contact forces exerted on the phantom. J-shape *ZipwireTM Stiff* guidewire (Boston Scientific, USA) with no support catheter was employed. A guide catheter functions the passage from robotic unit to the phantom and delivers GW up to the abdominal aorta. The camera captures fluid video at 45 frames per second (fps) rate, and image processing algorithm achieved catheter pose tracking at 40Hz, i.e., catheter tip position feedback for control loop and pose measurement for force estimation. The numerical force estimator runs parallel to image processing at a lower rate of 24Hz due to inverse FEM model computations. Thus, the update rate of PD force controller is limited to force feedback rate (24Hz), while the inner velocity PID controller runs at a much higher frequency of 2.4kHz. The robotic manipulator has two degrees of freedom to advance, retract, and rotate catheter/GW. The proposed design includes a linear drive assembled on a rotating drive through a slip-ring gantry. Two servomotors (Dynamixel XH430 series, ROBOTIS, CA, US) under velocity control law based on a PID controller were utilized in drivers. Linear fractional wheel provides translation motion. Rotational drive rotates transnational unit, delivering an unlimited rotation motion through gears. The inner velocity PID controllers of servomotors were tuned based on manufacturer instruction before tuning the outer loops. Max velocity limits were set to $70\,mm.s^{-1}$ in linear motion and $120\,degree.s^{-1}$ in rotational motion. The operator can accelerate or slow down motion velocities while navigating in a manual mode. Outer loop controllers are tuned through hardware in the loop method, followed by manual fine-tuning. Contact force controller tuning is performed where GW is introduced to Right Common Carotid Artery (RCCA) and intraluminal max CF raised near the max safe CF set-point. The goal of CF tuning

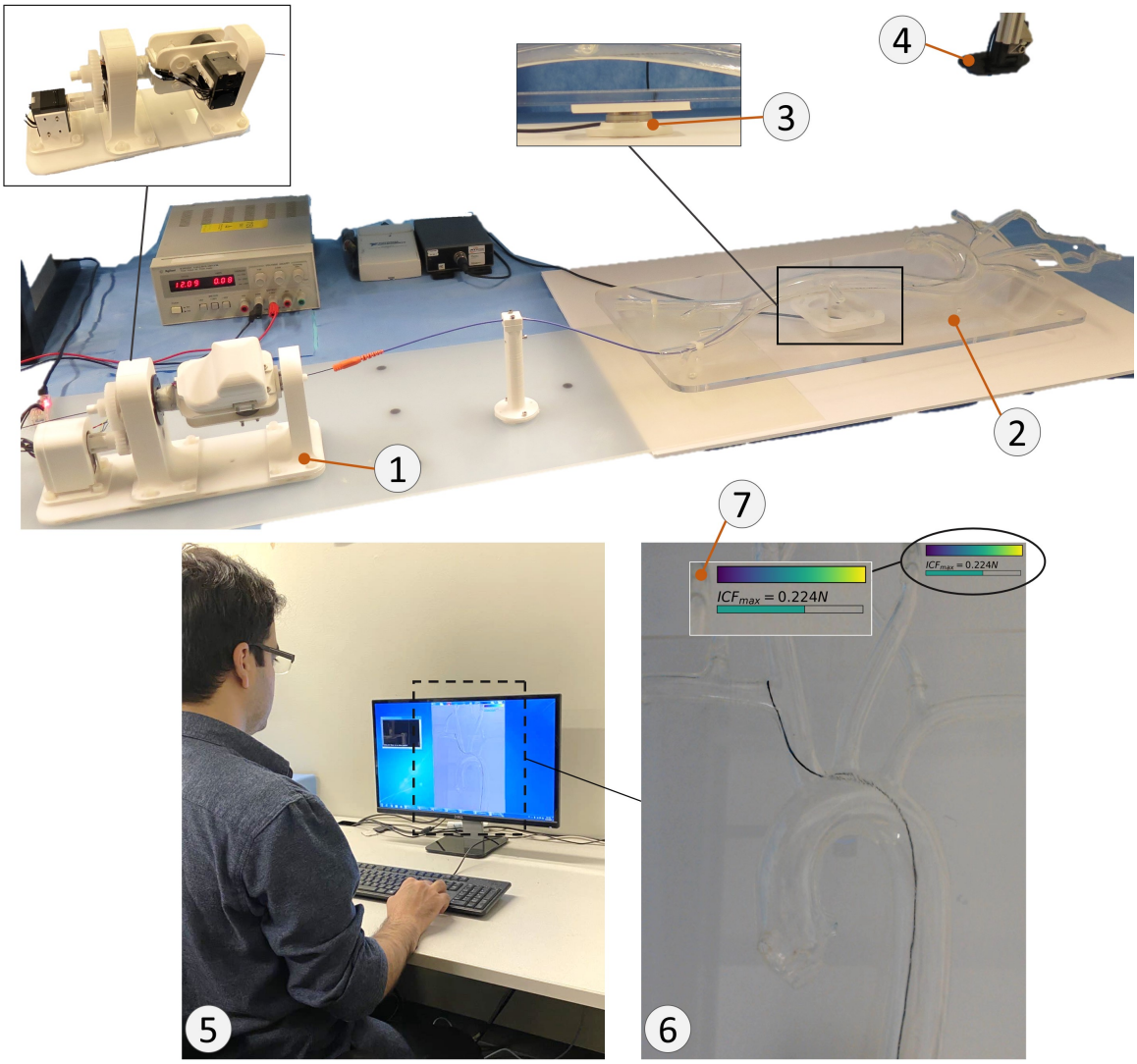

Figure 31: Teleoperation catheterization platform to verify proposed control scenarios includes: (1) robotic catheter manipulator, (2) vascular aortic arc phantom, (3) phantom force sensing, (4) camera, (5) operator work station, (6) visual guidance, and (7) ICF_{max} monitoring

was to achieve a critically damped response with no overshoot and minimum rise time. The tip position controller is tuned during retracting GW over a jammed condition that occurred in RCCA with a predefined retraction value $\Delta P_t = 5mm$. The system is tuned with large proportional and integral terms to respond fast to the change in tip position and reduce the settling time to meet the target value.

4.4 Results and Discussion

4.4.1 Study Protocol

In order to evaluate the effectiveness of the proposed framework, an expert was asked to conduct teleoperation navigation tasks. An operator highly familiar with the procedure and setup is chosen to eliminate variability in the trials due to operator-to-operator and insufficient navigation skills in manual teleoperation. The navigation tasks are cannulation of the Right Subclavian Artery (RSA) and the Right Common Carotid Artery (RCCA) to meet a target. The operator was asked to perform each cannulation task five times in three modes:

- **Teleoperated**: Teleoperation navigation of guidewire under visual guidance where no ICF data is given to the operator.
- **Teleoperated under visual contact force monitoring (VCFM)**: Teleoperation navigation under visual guidance with ICF_{max} monitoring, *i.e.,* maximal contact force value, is displayed on the screen as presented in Fig. 31.
- **Teleoperated under intraluminal contact force control (ICFC)**: Shared control navigation using the proposed intraluminal CF control and automated retraction framework, in which the robot controls the insertion and the operator guides the rotation.

4.4.2 Force Control-based Catheterization

The first experiment is designed to validate the overall accuracy and performance of RIFCC and ACR in limiting the contact forces in the safe range chosen by the operator. For this purpose, the operator conducts the cannulation of RSA and RCCA using the proposed framework in the human-robot shared teleoperation control loop. When the ICF_{max} is far enough from the safe limit, the internal velocity controller runs at a

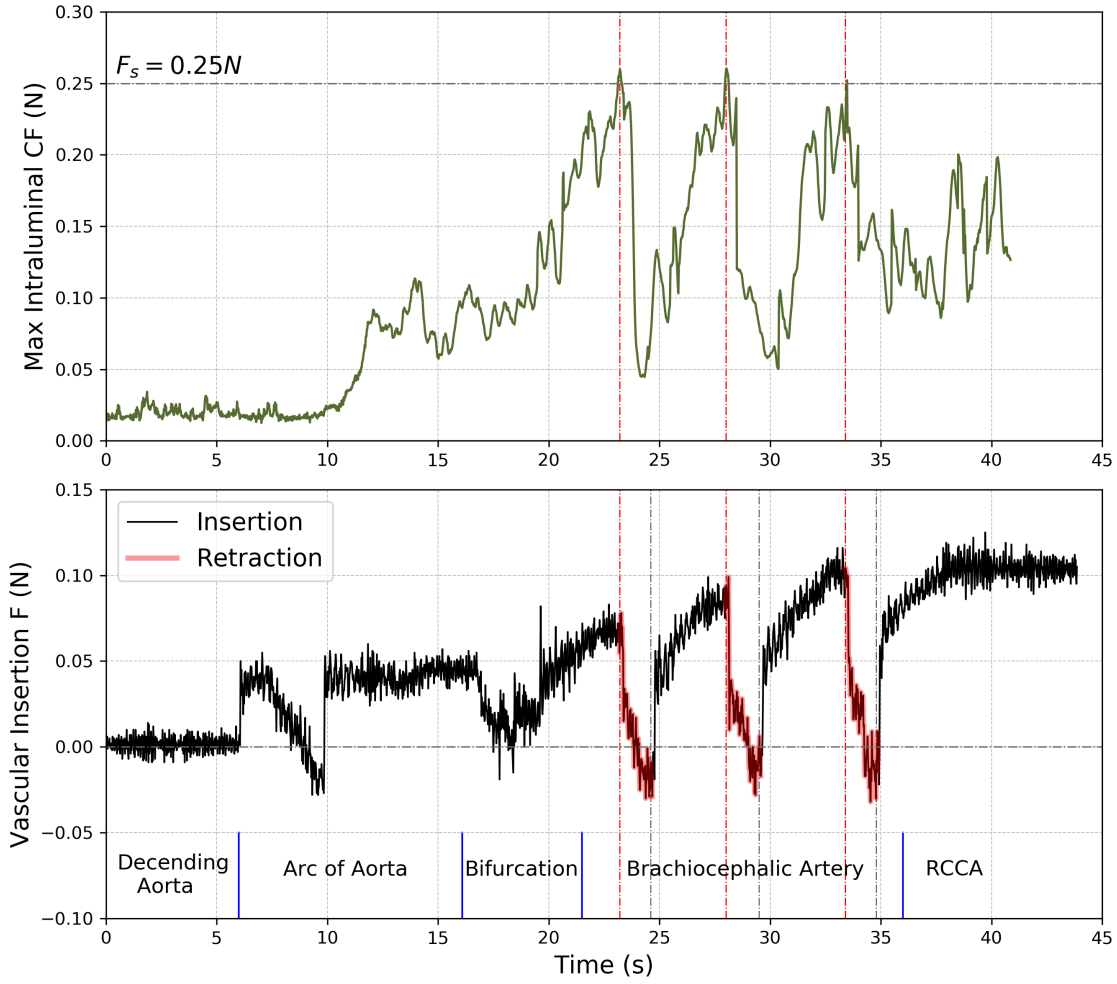

Figure 32: ICF_{max} (maximum of all contact forces) and VIF during intraluminal CF control teleoperation with safe ICF limit reference (F_s) is set to $0.25\,N$. System autonomously performs retraction and re-insertion to limit the ICF. Navigation states based on tip position are indicated in the bottom that shows tool motion through descending aorta to reach the arc of aorta, passing bifurcation toward brachiocephalic artery, and then retraction-reinsertion in brachiocephalic artery to attain the RCCA.

saturation limit for maximum possible insertion speed. The operator can adjust the velocity saturation limit to control the insertion speed if required for the navigation procedure. Thus, operator commands insertion or retraction via a joystick/keyboard interface, while robot automatically controls the process to maintain ICF_{max} and perform retract-reinsert trials, using image-based force and position sensing. Fig. 32 shows ICF_{max} and VIF in an example of RCCA cannulation using the proposed

automated framework, in which the safe force limit reference (F_s) was set to $0.25\,N$. ICF_{max} is the maximum magnitudes of points contact force vectors applied on the inner lumen vessel wall extracted from image-based estimations. VIF is the insertion forces measured directly to the phantom, which is calculated as a root-mean-square force modulus from 3D components measured by the F/T sensor under phantom. Automated force control, i.e., IFCC and ACR, limits the ICF_{max} in the prescribed safe range. ICF_{max} is fairly low in the aorta through the beginning of the procedure until it gets into the brachiocephalic artery. As ICF_{max} raises and gets closer to the limit F_s, the force controller slows the insertion process, resulting in ICF_{max} and VIF ascending rate to drop. Smoother increase in ICF_{max} shows effective controller response to sudden change in force which would otherwise lead to peaks over safe limit. Vertical dashed red lines show where the force controller reached the maximal safe ICF and momentarily the ACR engaged and retracted the GW. Fig. 33 shows examples of jammed states as longitudinal friction, regardless of friction types (coulomb, stribeck, etc), along the guidewire build up and caused large deflection with excessive ICF on the vasculature, where advancing the tool will cause complications. The automated framework retracted the GW until the whole excessive deflection relaxed and the distal tips moved backward at a minimum value, where relaxed states are achieved (Fig. 33 bottom image). In the relaxed state, the deflections are just caused by lateral contact forces of the vessel wall. Automated retractions reduced ICF_{max} significantly, as well as, VIF dropped sharply due to relaxing elastic forces induced to the GW by longitudinal friction built-up through the insertion process. Retractions are highlighted in red on the VIF graph (Fig. 32). VIF value goes negative, once the GW is fully stretched and whole GW body, including distal tip, is retracting. Vertical black dashed lines are the end of visual servoing loop where tip position met predefined displacement and the ICF control loop engages for reinsertion process. The followed reinsertion trial started with significantly smaller ICF_{max} and advanced the

(a) (b) (c) (d)

Figure 33: Jammed state of the GW (top) caused by friction build up, excessive deflections and large ICF transferred to a relaxed state (bottom) in the following re-insertion by automated retraction and ICF control framework.

procedure forward. Autonomous retraction and reinsertion are repeated three to four times until the cannulation target was achieved. It shows the effectiveness of the proposed automated framework to advance catheterization procedure while limiting ICFs and reforming the jammed condition,*i.e.,* extreme deflections and friction, and the associated CF peaks. Results of RSA cannulation also suggested a similar trend in ICF_{max} and VIF.

The second set of experiments was designed to compare the teleoperation performance with and without the proposed automated framework and further evaluate the improvement by employing the visual intraluminal CF monitoring system. The task was defined to meet a target point of artery in three modes: (*i*) Teleoperated, (*ii*) Teleoperated under visual ICF_{max} monitoring (VCFM), and (*iii*) Automated teleoperation under ICF control. Safe CF limit of $0.2\,N$ and $0.25\,N$ were prescribed.

The operator was instructed to try the best use of ICF data to maintain force value in the safe range during the procedure. Fig. 34 illustrates a comparison in the ICF_{max} between the frameworks and the force distribution during the cannulation. Results highlight that the automated ICFC framework restricted contact force under safe limit, whereas VCFM teleoperated and manual teleoperated navigations had several force peaks over the safe limit. ICFC outperformed both manually controlled modes, and the distributions show a significant reduction in force values. At the lower F_s of 0.2 N, teleoperation with ICF_{max} monitoring was less effective as the operator struggles to keep the contact force smaller, which underlines the need of a force control system.

However, the visual ICF_{max} monitoring system helped the operator avoid extreme peaks (over $0.3\,N$) and keep the majority of navigation near safe range compared to without force monitoring. It suggests that VCFM effectively improves the performance of navigation and can potentially prevent serious complications. Observations showed that the operator might struggle to manage the navigation tasks to follow the path while simultaneously keeping an eye on the ICF_{max} value and modified navigation tasks accordingly. On the other hand, the robot effectively performed a safe automated insertion and retraction in the shared control framework and let the operator only handle the rotation.

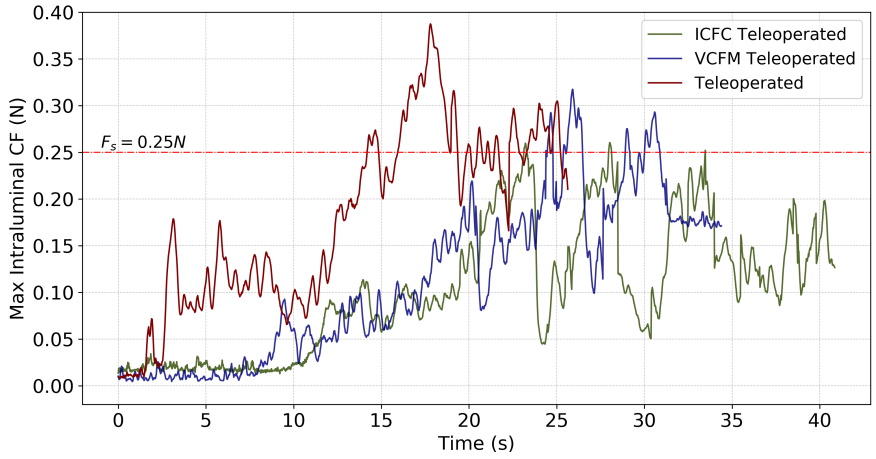

(a)

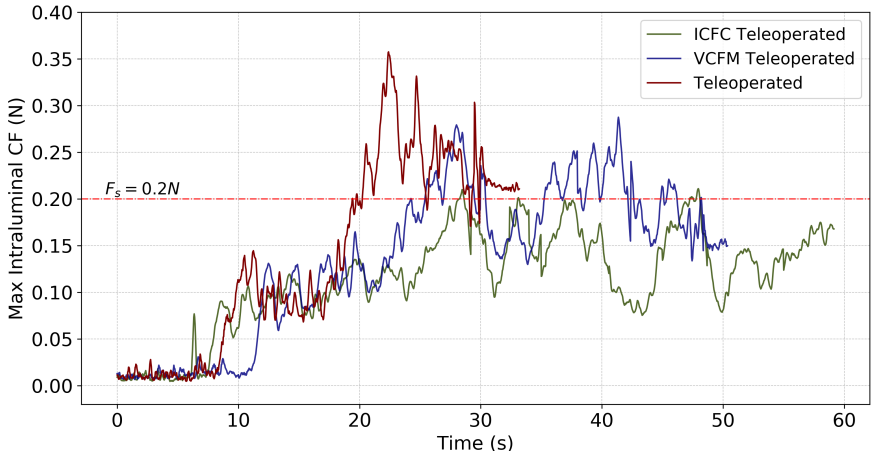

(b)

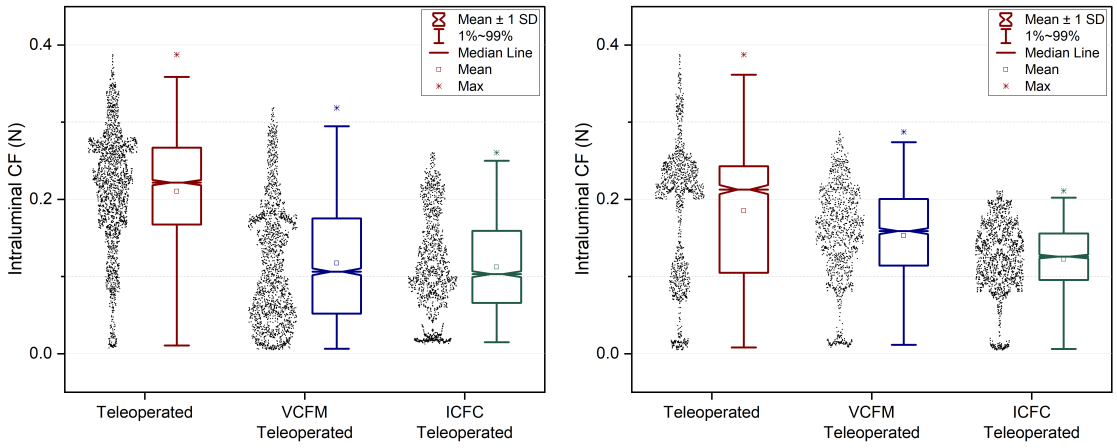

(c) (d)

Figure 34: ICF in automated mode is compared with teleoperation under visual ICF monitoring and teleoperation without ICF data, $F_s = 0.25\,N$ (a, c), $F_s = 0.2\,N$ (b, d).

4.4.3 Metrics Extraction and Evaluation

The quantitative evaluation of robotic catheterization frameworks was assessed through the metrics of ICF_{max}, VIF and tip kinematic. The quantitative performance metrics for ICF_{max} and VIF in this study include:

1. Maximum force value (N)
2. Mean force value (N)
3. Standard deviation of force (N)
4. Force impact over time (FIT, $N.s$, calculated only for ICF_{max} values over safe limit)
5. Minimum force value (N, only for VIF)

Table 6 shows the average of the performance metrics for all trials in cannulations of RSA and RCCA. Significant improvement can be seen in the force metric in favor of the ICFC approach. Maximum ICF was $0.204\,N$ and $0.257\,N$ in ICFC for the F_s of $0.2\,N$ and $0.25\,N$ respectively, where VCFM achieved $0.287\,N$ and $0.304\,N$. ICFC and VCFM reduced ICF_{max} compare to traditional teleoperated ($0.36\,N$). Mean ICF_{max} for automated control framework ($0.112\,N$, $0.135\,N$) was also smaller than VCFM ($0.115\,N$, $0.146\,N$) and teleoperated ($0.176\,N$). Considering maximum and mean ICF_{max} as the primary metrics of safety, ICFC achieved significantly safer tool motion.

Table 6: Average values for statistical analysis of intraluminal contact force and force exerted on vasculature from automated ICFC procedures versus VCFM and traditional teleoperation.

	ICFC teleoperated		VCFM teleoperated		teleoperated
	Fs=0.2N	Fs=0.25N	Fs=0.2N	Fs=0.25N	
Maximum ICF, N	0.204	0.257	0.287	0.304	0.36
Mean ICF, N	0.112	0.135	0.115	0.146	0.176
STD ICF, N	0.062	0.075	0.084	0.086	0.095
Maximum VIF, N	0.125	0.159	0.164	0.175	0.215
Minimum VIF, N	-0.058	-0.042	-0.023	0.01	0
Mean VIF, N	0.054	0.068	0.095	0.107	0.143
STD VIF, N	0.038	0.041	0.042	0.051	0.092

Maximum and mean VIF, as the metric for the quality of procedure rather than safety, were lower in automated ICFC compare to VCFM and traditional teleoperated. Overall, ICFC reduced vascular insertion force 36%-46% compared to VCFM, and 39%-52% compared to traditional teleoperated. The lower VIF translates into a more controlled procedure and improved quality by limiting the risk of complications. Standard deviations of both ICF_{max} and VIF were also smaller for the automated ICFC framework. Decreased variation in forces suggests smoother guidewire-vessel interaction with limited extreme deflections.

Force metrics of VCFM compared to the traditional teleoperation shows clear improvements in navigation, i.e., lower intraluminal contact forces and insertion forces. VCMF outperformed traditional teleoperated cannulation by 18% reduction in ICF_{max}, 25% reduction in mean ICF, and 29% smaller VIF.

The *risky* contact force is defined where the ICF_{max} value is higher than the prescribed safe limit, F_s. The larger ICF_{max} and longer duration over safe limit lead to a higher chance of complications. With the definition above, the time integration of contact force (FIT) over safe limit can be the quantitative metric for risk of complication:

$$FIT = \sum_{i=0}^{N} max\big\{(ICF_{max_i} - F_s),\ 0\big\}\Delta t \tag{27}$$

where ICF_{max_i} is ICF_{max} at time index i.

Fig. 35 (a) presents the box plot for FIT over safe limit. ICFC framework has nearly zero FIT over safe limit (0 - 0.006 $N.s$) compared to 0.224 $N.s$ (interquartile range IQR 0.201 - 0.255 $N.s$) for VCFM and 0.415 $N.s$ (IQR 0.27 - 0.453 $N.s$) for teleoperated. Minimizing *risky* contact force contributes in minimizing risk of complications, specially vessel perforation and dissection. In this regard, the ICFC framework associates the minimal risk, and the VCFM framework benefits less risk as of teleoperated. Tip trajectory is analyzed to extract the tip kinematic metrics of speed, including: 1. maximum speed ($mm.s^{-1}$) 2. mean speed ($mm.s^{-1}$), and 3. standard deviation of

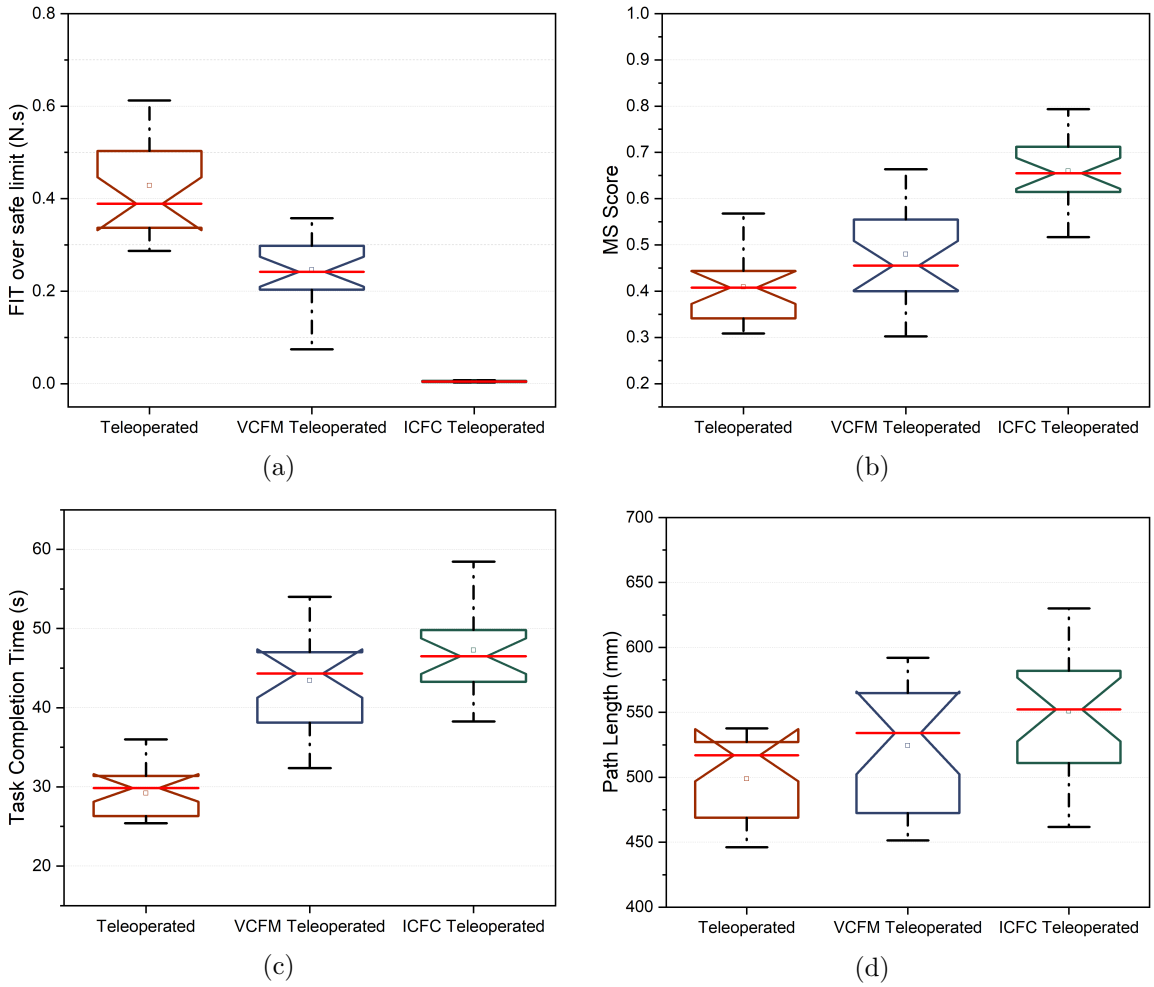

Figure 35: Metric results for the comparative study in cannulation tasks: (a) FIT over safe limit, $N.s$, (b) MS score, (c) task completion time, s, (d) path length, mm.

speed ($mm.s^{-1}$). Table 7 includes the tip motion values for manually teleoperated vs proposed automated framework. ICFC performed cannulation tasks at a lower mean speed, and VCFM mode was slower than traditional navigation. The mean speed was reduced at the lower targeted safe limit ($F_s = 0.2\,N$) for both robot and operator. The lower STD seen in ICFC framework indicates a more continuous, controlled, and smoother motion in automated navigation than manually derived.

To further assess the GW tip motion during navigation of each mode, motion smoothness (MS) was computed [153] as a quantitative measure of smoothness. This factor is based on instantaneous jerk defined as third derivative of end effector position,

Table 7: Tip kinematic metrics between automated ICF control teleoperation framework versus manually teleoperated with and without visual ICF monitoring system.

	ICFC teleoperated		VCFM teleoperated		teleoperated
	Fs=0.2N	Fs=0.25N	Fs=0.2N	Fs=0.25N	
Max Speed, mm/s	70	70	70	70	70
Mean Speed, mm/s	13.75	15.4	15.2	17.6	23.15
STD Speed, mm/s	18.3	16.3	23.4	21.6	27.6

($J = \frac{d^3x}{dt^3} = \dddot{x_t}(mm.s^{-3})$) and represents a change in acceleration. The jerk data is normalized in the range of 0 to 1 to ease the interpretation of MS and to present a relative normalized value. MS is calculated as the time-integrated squared jerk by replacing the integration operator with its discrete-time equivalent:

$$MS = 1 - \frac{1}{N}\sum_{i=0}^{N}\sqrt{J_{x,i}^2 + J_{y,i}^2 + J_{z,i}^2} \tag{28}$$

where

$$J_{u,i} = \frac{u_{i+\frac{3}{2}} - 3u_{i+\frac{1}{2}} + 3u_{i-\frac{1}{2}} - u_{i-\frac{3}{2}}}{\Delta t^3} \tag{29}$$

is the third-order central finite difference of discrete trajectory signal along u axis [153]. Smoother catheterization is where change in tip acceleration is small, which results in smaller jerk and higher normalized MS. In clinical condition, the impact of the blood flow disturbances on the tool tip motion should be filtered prior to jerk integration for computing MS metric. MS box chart is shown in Fig. 35 (b) based on all experiments for different prescribed safe limit. Mean MS score were 0.65 (0.51 - 0.79) for the ICFC teleoperated, 0.46 (0.3 - 0.67) for the VCFM teleoperated, and 0.41 (0.3 - 0.57) manual teleoperated. The ICFC framework outperformed both visual CF monitoring framework and traditional teleoperation by 41.3% and 58.5%, respectively. VCFM resulted in smoother motion compared to manual as the operator could adjust insertion based on ICF_{max} data to avoid peaks and jerky motion; however operator rarely achieved as smooth motion as ICFC. The other absolute quantitative

standard metrics are task completion time (TCT) and path length (PL). PL is the length of the curve traversed by tip over time. Fig. 35 shows the quantitative results as the box plots with these metrics compared, $TCT\,(s)$, and $PL\,(mm)$. The task completion time for ICFC teleoperated (range $37\,s$ - $59\,s$, mean $46\,s$) was close to VCFM teleoperated (range $32\,s$ - $54\,s$, mean $44\,s$), but both are longer than teleoperated (range $25\,s$ - $36\,s$, mean $30\,s$). ICFC navigation lasted longer because of the slower procedure as ICF_{max} increases and the added time of automated retraction-reinsertions to relax GW deflections. Likewise in VCFM mode, the operator slowed the insertion to prevent ICF_{max} overshoot and performed trail/error. Path length of ICFC teleoperated ($555\,mm$) is slightly greater than VCFM teleoperated ($525\,mm$), and latter is greater than teleoperated ($500\,mm$). Retraction trials increased the tip path length 5 to 10%.

4.4.4 Discussion and Limitations

Vessel perforation, dissection, crossing through subintimal space and other complications associated with tool-tissue interactions can be minimized by limiting the magnitude and time impact of local intraluminal contact force with the arterial wall. The proposed semi-automated contact force control-based framework successfully maintained ICF within the safe force limit, i.e., depicting minimal FIT over safe limit. The automated retraction feature was able to restore stuck guidewire in the vessel to a relaxed shape, and automated re-insertions advanced the procedure to achieve the targeted location. Comparing the ICFC framework with manually controlled teleoperated modes demonstrates a reduction in both ICF and total vascular insertion force values, i.e., mean, maximum, STD, and FIT. ICFC also shows a smoother tip motion as it damps the sudden changes in force and guidewire deflections; consequently, it results in a lower jerk and less slip/stick in tool motion. However, ICFC procedures took more time and longer path to complete. Quantitatively and qualitatively, the automated robotic control outperformed manual control in the presence of visual

ICF_{max} monitoring. Moreover, VCFM teleoperation compared to traditional teleoperation resulted in a significant FIT reduction over safe limit and lower maximum and mean ICF_{max} with no extreme peak over $0.3\,N$. The standard deviation of forces and tip jerk were also lower, which indicates that the operator can achieve smoother and more stable arterial wall interactions by adjusting navigation tasks based on ICF_{max} feedback. Accordingly, VIF metrics are also showing an improvement due to the use of VCFM. Albeit VCFM shows promising results, it can be challenging for operators to monitor and control ICF while handling navigation tasks simultaneously. The performance could be highly dependent on operator skills, as several studies have also highlighted the steep learning curve associated with safe carotid artery cannulation [154, 155]. The automated system decreases user workload of top skilled operators while improving the skills of the novice user. It can make the clinician task easier as the robotic vascular intervention may be less stressful, less prone to complications, and help tackle more challenging lesions. The automated robotic features can standardize the procedure for a wide range of operators, different fatigue levels, and age.

Some limitations remained to this work and may be addressed in the future studies. The operator was highly skilled in controlling the robotic teleoperation, but not a clinician. The comparative results are only for one expert operator whereas more operators with different skill levels can involve in an extensive study. The safe contact force value in this study is set based on our experimental setup and to evaluate the concept of the proposed method. The safe ICF level should clinically be investigated, which depends on the targeted vessel and patient conditions, e.g., the diseased and weaken arterial wall can be perforated at a lower force level. It is also a factor of type and property of interventional device such as tip shape and size. On the other hand, the reference safe force limit should be feasible to accomplish. A minimum level of force is being applied to the vascular wall due to the lateral deflections in vasculature which can not be avoided. The proposed system may take long to finish a task with

an extremely low prescribed safe limit. Sometimes high contact forces are needed, e.g. passing a lesion, perforating for shunts or anchoring, which the proposed system can be adapted to such cases. Lastly, automated tip rotation control can be added to the system to have a fully automated movement and to overcome excessive friction and crossing lesion with tip spinning and wiggling.

4.5 Conclusion

Complications and risk of injury may happen in vascular tool interaction due to overloading of intraluminal contact forces. The control of interactions with vasculature through the entire tool shape is still unsolved, specifically for common non-steerable guidewire and catheters. A novel control technique was proposed to limit contact forces through the tool interaction with the vessel wall. The proposed method employs a velocity actuated contact force controller to conduct the regulated insertion of the tool and an automated retraction based on visual servoing of tip to relax jammed condition. The method was deployed on robotic-assisted cannulation of carotid arteries. The robot autonomously controls the insertion and the operator handles the rotation in a human-robot shared control system. The proposed technique successfully performed tool insertion with controlled ICF in the safe limit and attained retraction-reinsertion trials once safe force limit is reached. It allows advancing vascular tools without worrying of damage to the vessel wall. The effectiveness was demonstrated through experiments in comparison with manual teleoperation using visual ICF_{max} monitoring and traditional teleoperation. Automated ICFC framework outperformed both manually teleoperated modes with a significantly reduced ICF, decreased force on the phantom, improved tool motion, and lower workload. Providing ICF_{max} data through the VCFM system also guided the operator to achieve improved navigation compared to traditional teleoperated, but still *risky* ICF peaks have been observed.

The more controlled tool-tissue interactions through employing intraluminal force feedback in both automated control and visual guidance techniques can translate into a reduction in intraoperative and post-treatment complications, e.g., perforation, dissection, embolization, brain lesion, and stroke.

Chapter 5

Conclusion and Future Research Directions

5.1 Conclusion

The current practice of endovascular interventions, in both robotic and manual manipulations, carries limited control on tool-tissue interactions. Studies reported intraprocedural and post-treatment complications, e.g., perforation, dissection, embolization, brain lesion, and stroke, due to overloading of intraluminal tool interactions with the vasculature. The main objective of this thesis is to develop a platform for measuring and controlling intraluminal interactions of endovascular tool with the vessel wall in order to improve the quality and safety of intervention procedures. A model-based method is used to estimate contact forces by simulating the tool during the endovascular navigation procedure. The required data for the numerical model is extracted from image feedback. By achieving intraluminal force sensing in real-time, a robotic control method is used to maintain interactions within a safe limit. This thesis focuses on tool-tissue contact point force at the extreme condition with the highest risk of over-pressure on arterial wall. Methods and automation techniques are proposed and

tested with the off-the-shelf flexible catheters and guidewires without instrumented sensors and actuation modules. The proposed methods contribute to the development of technologies using the current imaging feedback available in endovascular intervention practice. In the second and third chapter of this thesis, an image-based force estimation approach is developed and implemented for ICF interaction monitoring in a robotic teleoperated navigation. In Chapter 4, an automated robotic insertion technique is proposed to control the interaction forces.

The sensor-less contact force estimation approach proposed in Chapter 2 employs numerical FEM modeling of an endovascular tool using image-based data. The FEM model that was constructed from nonlinear beam elements achieves real-time solution. The real-time image processing algorithms extracts the tool body to locate the contact points and compute their deflection as the inputs for the FEM model. Three-point-bending tests were performed to obtain the equivalent bending modulus of the complex structure of a guidewire which is a fixed input in the FEM model. The force estimation accuracy was experimentally validated through a custom-designed setup which enables direct CF measurement on several contact point phantoms (CPP). Comparing force estimations to real measurements under random deflection confirms proposed method effectiveness and accuracy for multiple contact forces estimations at the side of an interventional tool. Demonstrating that image-based approach has great potential for simultaneous sensing of side CFs and the applicability to conventional off-the-shelf catheters/guidewires in lack of force skin element.

In the second study, an intraluminal tool-tissue monitoring is developed using the proposed image-based force estimation concept. The method was implemented on cannulation of aortic arteries in a cardiovascular phantom using teleoperated robotic navigation. The FEM beam model formulation is updated to consider shear deformations. The image processing algorithms achieve tracking contacts and computing the required pose measurement to feed FEM model. The model continuously simulates

tool motion as it is being navigated through cannulation procedures and estimates the tool-arterial wall interaction forces. Tracking of multiple ICFs is successfully elicited and the ICF contours are mapped on the arterial wall. Results suggest that RCCA and RSA cannulations are associated with higher forces where maximal ICF is seen at the bifurcation edge of the aortic arch. In addition to monitoring ICFs intraoperatively, the results can provide insight into force patterns and place of maximal ICF to raise our understating of tool behavior. The intraprocedural stress analysis of the tool is also achieved, a potential method for evaluation in practice to design catheters/guidewires with enhanced efficacy. Evaluating ICF compared to the forces exerted on the vasculature showed a gradual increase in intravascular force to large values while resultant forces and similarly insertion forces stay relatively small. These findings suggest the potential need for intravascular tool interaction monitoring. ICF can be visualized intraoperatively for clinicians to minimize the risk and to optimize the novices learning curve. The online intraluminal monitoring system also provides insight into the design of autonomous robotic platforms that can potentially guarantee a safe tool-tissue interactions. Proposed system can also be used as a training tool for novice operators to provide feedback during manual manipulation.

Chapter 4 introduces a semi-automated endovascular insertion framework to control the interaction forces. Robotic control can maintain the force limit and perform a regulated insertion smoothing force peaks while preserving safe motions. It essentially has a closed-loop intraluminal contact force controller that uses visual force sensing feedback. An automated retraction feature is developed based on visual tracking of tip position to ease ICF build-up by relaxing excessive deflections. The proposed technique successfully advanced insertion with the ICF controller and attained retraction-reinsertion trials by tip visual servoing. Automated force control-based catheterization accomplished limiting interaction forces in the prescribed safe range, damping peak ICF and restoring jammed conditions. The automated

framework outperforms manually teleoperated framework using visual ICF monitoring and traditional teleoperation quantitatively and qualitatively, i.e., smoother navigation, reduced ICF, reduced vascular insertion force, and decreased operator workload. Employing the visual ICF monitoring system in manual teleoperation also indicates improvement in force and motion metrics compared to traditional teleoperation. However, ICF peaks have been observed as manual handling cannot respond fast to the sudden changes in forces. Also, it can be challenging for operator to control ICF while handling navigation tasks simultaneously. The more controlled tool-tissue interactions via intraluminal force information in both automated control and visual guidance frameworks translate into a reduction in intraoperative and post-treatment complications.

The future trend of robotic vascular system orients toward improving the quality of procedures where human skills and abilities are limited. Automated features can potentially be implemented to the current robotic platforms to secure a safe navigation, reduce user workload, standardize the procedure, and support tackling complex cases.

5.1.1 Limitations

Some limitations remain to the works presented in this thesis. The proposed FEM model uses the bending modulus profile along the tool from the distal tip toward the proximal end. In our work, continuous variation in the flexural rigidity of the tool has been obtained by fitting a curve to the discrete three-point-bending measurements. However, the rigidity distribution profile can be improved by smaller sequential step size in testing or having information about the tool mechanical properties from the manufacturer. Mechanical properties are dependent to the type of specific vascular tool. Also, our model considers a solid cross-section with equivalent bending modulus whereas endovascular tools are usually made of a composite material including core metal, polymer coating, coils, etc. This assumption should not affect force estimation

accuracy but can affect tool's structural stress analysis presented in Chapter 3. To overcome this limitation, the FEM model can be updated based on each specific endovascular tool design. Another limitation is related to the correctness of image-based pose measurements that depends to the accuracy of camera calibration. The imaging platform was based on an RGB webcam camera which can be improved using a higher resolution camera or commercially available imaging systems in a more clinically relevant test setup. Also, real-time camera calibration techniques can be performed to increase the imaging correctness. In this thesis, the image-based estimation has been developed considering 2D deflection of the tool to prove the concept. Future work could address the improvement and testing with 3D imaging with the same estimation concept. The experimental setup used in Chapters 3 and 4 may not completely capture clinical conditions. The phantom frictional forces can be different from a human vessel. Moreover, image processing and force estimation frequency were limited to an ordinary personal computer's computational power, in which a high-performance computing system could improve the sampling frequency to a much higher value suitable for clinical control and automation applications.

5.2 Future Research Directions

The robotic endovascular intervention brought several benefits to clinicians by moving operators away from the radiation source, adding comfort and enhancing controllability of interventional tools. However, current robotic platforms do not address an unmet need in treatment of cardiovascular diseases and do not bring significant clinical benefits over conventional interventions, especially in PVI and PCI procedures. The value of robotic systems is in delivering treatment or a task that humans struggle to achieve. The Magellan ^{TM} system has an advanced steerable catheter for navigation through the complex case but has been failed in the medical market due to the limited number

of compatible therapeutic devices. The Corpath® system has been accepted in the market as being compatible with most off-the-shelf tools and can be used for treatment purpose as well as navigation. The recent automated feature added to the Corpath® system is the path to improve patient care and to standardize the procedure for a wide range of operators. Future research directions can integrate more automated and image-guided methods to increase safety, minimize complications, facilitate complex tasks, and more importantly increase the success rate for interventional procedures to avoid open surgeries. Another shortcoming of the robotic platform is the lack of tactile sensing and haptic feedback. Several studies worked on developing tactile and haptic displays, but an ergonomic design based on clinicians conventional learning is still missing. Also, the proximal sensing is composed of overall tool-tissue interactions and friction between the instruments where clinicians struggle to distinguish actual tool-tissue interactions. The tactile displays can be further improved to render local intraluminal interaction forces in general vascular navigation and the tip CF in the EP procedures.

Some aspects of this thesis can be improved in future works. The phantom can be replaced with a artificial tissue made model with similar elastic properties of a vessel wall which upgrades the setup to a more clinically relevant condition. The experimental studies can be extended to other endovascular intervention procedures in peripheral arteries. 3D image processing algorithm to detect and track tool-vasculature interactions can be investigated and implemented. Machine learning algorithms have shown promising results for image processing, which can be used for catheter-vessel contact detection and tip tracking. The proposed image-based force monitoring can be studied in navigating through coronary arteries, where the heart's dynamic motion brings method implementation to a higher complexity level. Learning-based techniques can be investigated to track vessel motion or estimate the collisions.

Emerging development in machine learning techniques and autonomous robotic

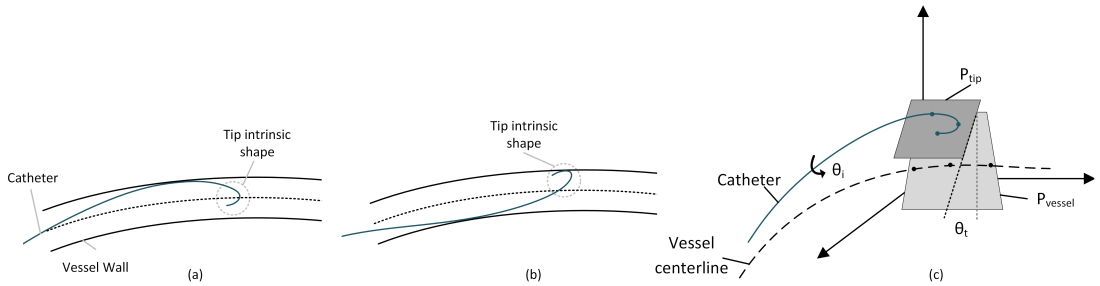

Figure 36: Tip rotation angle along, (a), and against, (b), the vessel curvature. Analysis and control of tool motion can be investigated based tip rotation angle, (c), to improve the quality of navigation and limit significant interactions.

systems can be employed to improve current state of robotic endovascular intervention. Experts use tactile feedback in the proximal end and visual understanding based on their experience to perform optimized navigation and minimize possible complications. Learning from demonstration methods can be developed to extract experts navigation techniques and reduce tool-tissue interactions while an ICF control acts as an extreme safeguard. The expert techniques also can be integrated within automated retraction-insertion control methods to optimize the performance and to reduce procedure time. The safe limit of ICF used for the proposed ICF control approach can be studied. The focus of this work was to present and prove the concept of automated force control of intraluminal interactions. A potential study could be ex-vivo experiments on cultivated human vessels to define the safe range of pressure/force of tools on the internal wall. In addition to perforation, dissection, and tearing, the small injuries on the intimia wall layer should be investigated. The safe ICF level depends on targeted anatomy, patient condition, vessel characteristics and varies over different vascular tools based on their design and mechanical properties.

Another research direction can study a fully autonomous system in which the tip rotation angle is controlled and directed though bifurcations toward the object path. Common GW tip has a *J curved* or *angled* shape. The tip rotation angle can be controlled based on the angle with the vessel centerline, as depicted in Fig. 36. Two planes can be fitted to the tool distal end and vessel centerline, and a control

algorithm can be used to achieve the desired angle θ_i. Extracting the expert technique based on analysis of tip deviation angle from the vessel centerline could be an idea in learning-based automation methods. A smoother insertion procedure also can be reached by keeping the intrinsic tip curvature of such tools along with the curvature of the vessel centerline (see Fig. 36). It would potentially help to minimize the number of tip contact points with the vessel and decrease the amount of deformation, consequently resulting in lower interaction forces.

Modeling and model-based control of the tool inside the vessel is quite challenging, considering the significant nonlinearity in the tool-tissue interactions. Another research direction in endovascular intervention can focus on precise predictive modeling of vascular navigation based on patient-specific parameters.

Bibliography

[1] Arrhythmia treatment — robotic catheter ablation - stereotaxis. `http://www.stereotaxis.com/`, 2020.

[2] Ejaz M Khan, William Frumkin, G Andre Ng, Suresh Neelagaru, Freddy M Abi-Samra, Jay Lee, Michael Giudici, Douglas Gohn, Roger A Winkle, Jonathan Sussman, et al. First experience with a novel robotic remote catheter system: Amigo™ mapping trial. *Journal of Interventional Cardiac Electrophysiology*, 37(2):121–129, 2013.

[3] Corindus, a siemens healthineers company. `https://www.corindus.com/`, 2020. (Accessed on 12/15/2020).

[4] Tejas M Patel, Sanjay C Shah, and Samir B Pancholy. Long distance tele-robotic-assisted percutaneous coronary intervention: a report of first-in-human experience. *EClinicalMedicine*, 14:53–58, 2019.

[5] Jessica Burgner-Kahrs, D Caleb Rucker, and Howie Choset. Continuum robots for medical applications: A survey. *IEEE Transactions on Robotics*, 31(6):1261–1280, 2015.

[6] Jean Bismuth, Cassidy Duran, Milenko Stankovic, Borut Gersak, and Alan B Lumsden. A first-in-man study of the role of flexible robotics in overcoming navigation challenges in the iliofemoral arteries. *Journal of vascular surgery*, 57(2):14S–19S, 2013.

[7] Giulio Dagnino, Jindong Liu, Mohamed EMK Abdelaziz, Wenqiang Chi, C Riga, and G-Z Yang. Haptic feedback and dynamic active constraints for robot-assisted endovascular

catheterization. In *2018 IEEE/RSJ International Conference on Intelligent Robots and Systems (IROS)*, pages 1770–1775. IEEE, 2018.

[8] Kit-Hang Lee, Kin Chung Denny Fu, Ziyan Guo, Ziyang Dong, Martin CW Leong, Chim-Lee Cheung, Alex Pui-Wai Lee, Wayne Luk, and Ka-Wai Kwok. Mr safe robotic manipulator for mri-guided intracardiac catheterization. *IEEE/ASME Transactions on Mechatronics*, 23(2):586–595, 2018.

[9] Yogesh Thakur, Jeffrey S Bax, David W Holdsworth, and Maria Drangova. Design and performance evaluation of a remote catheter navigation system. *IEEE Transactions on biomedical engineering*, 56(7):1901–1908, 2009.

[10] Yusof Ganji, Farrokh Janabi-Sharifi, and Asim N Cheema. Robot-assisted catheter manipulation for intracardiac navigation. *International journal of computer assisted radiology and surgery*, 4(4):307–315, 2009.

[11] Julia Merkle, Christopher Hohmann, Anton Sabashnikov, Thorsten Wahlers, and Jens Wippermann. Central vascular complications following elective catheterization using transradial percutaneous coronary intervention. *Journal of Investigative Medicine High Impact Case Reports*, 5(1):2324709617698717, 2017.

[12] techniq - smart procedural automation. `https://www.corindus.com/corpath-grx/techniq`, 2020. (Accessed on 12/15/2020).

[13] Frederick S Keller. Interventional radiology: new paradigms for the new millennium. *Journal of Vascular and Interventional Radiology*, 6(11):677–681, 2000.

[14] Anthony Ciarallo, Cam-Tu Emilie Nguyen, and Lawrence Stein. Interventional radiology: from idea to device to patient. *McGill Journal of Medicine: MJM*, 10(2):144, 2007.

[15] DS Baim. Cardiac catheterization, angiography and intervention. *ANGIOLOGIA-BARCELONA-*, 52(6):259–260, 2000.

[16] Fred Morady. Radio-frequency ablation as treatment for cardiac arrhythmias. *New England Journal of Medicine*, 340(7):534–544, 1999.

[17] Ariel Roguin, Jacob Goldstein, Olivier Bar, and James A Goldstein. Brain and neck tumors among physicians performing interventional procedures. *The American journal of cardiology*, 111(9):1368–1372, 2013.

[18] James A Goldstein, Stephen Balter, Michael Cowley, John Hodgson, and Lloyd W Klein. Occupational hazards of interventional cardiologists: prevalence of orthopedic health problems in contemporary practice. *Catheterization and cardiovascular interventions*, 63(4):407–411, 2004.

[19] Celia Riga, Colin Bicknell, Nicholas Cheshire, and Mohamad Hamady. Initial clinical application of a robotically steerable catheter system in endovascular aneurysm repair. *Journal of Endovascular Therapy*, 16(2):149–153, 2009.

[20] Giora Weisz, D Christopher Metzger, Ronald P Caputo, Juan A Delgado, J Jeffrey Marshall, George W Vetrovec, Mark Reisman, Ron Waksman, Juan F Granada, Victor Novack, et al. Safety and feasibility of robotic percutaneous coronary intervention: Precise (percutaneous robotically-enhanced coronary intervention) study. *Journal of the American College of Cardiology*, 61(15):1596–1600, 2013.

[21] Sabine Ernst, Feifan Ouyang, Christian Linder, Klaus Hertting, Fabian Stahl, Julian Chun, Hitoshi Hachiya, Dietmar Bansch, Matthias Antz, and Karl-Heinz Kuck. Initial experience with remote catheter ablation using a novel magnetic navigation system: magnetic remote catheter ablation. *Circulation*, 109(12):1472–1475, 2004.

[22] Luigi Di Biase, Tamer S Fahmy, Dimpi Patel, Rong Bai, Kenneth Civello, Oussama M Wazni, Mohamed Kanj, Claude S Elayi, Chi Keong Ching, Mohamed Khan, et al. Remote magnetic navigation: human experience in pulmonary vein ablation. *Journal of the American College of Cardiology*, 50(9):868–874, 2007.

[23] Walid Saliba, Vivek Y Reddy, Oussama Wazni, Jennifer E Cummings, J David

Burkhardt, Michel Haissaguerre, Josef Kautzner, Petr Peichl, Petr Neuzil, Volker Schibgilla, et al. Atrial fibrillation ablation using a robotic catheter remote control system: initial human experience and long-term follow-up results. *Journal of the American College of Cardiology*, 51(25):2407–2411, 2008.

[24] Luigi Di Biase, Yan Wang, Rodney Horton, G Joseph Gallinghouse, Prasant Mohanty, Javier Sanchez, Dimpi Patel, Matthew Dare, Robert Canby, Larry D Price, et al. Ablation of atrial fibrillation utilizing robotic catheter navigation in comparison to manual navigation and ablation: Single-center experience. *Journal of cardiovascular electrophysiology*, 20(12):1328–1335, 2009.

[25] Prapa Kanagaratnam, Michael Koa-Wing, Daniel T Wallace, Alex S Goldenberg, Nicholas S Peters, and D Wyn Davies. Experience of robotic catheter ablation in humans using a novel remotely steerable catheter sheath. *Journal of Interventional Cardiac Electrophysiology*, 21(1):19–26, 2008.

[26] Shinsuke Miyazaki, Ashok J Shah, Olivier Xhaët, Nicolas Derval, Seiichiro Matsuo, Matthew Wright, Isabelle Nault, Andrei Forclaz, Amir S Jadidi, Sébastien Knecht, et al. Remote magnetic navigation with irrigated tip catheter for ablation of paroxysmal atrial fibrillation. *Circulation: Arrhythmia and Electrophysiology*, 3(6):585–589, 2010.

[27] Carlo Pappone, Gabriele Vicedomini, Francesco Manguso, Filippo Gugliotta, Patrizio Mazzone, Simone Gulletta, Nicoleta Sora, Simone Sala, Alessandra Marzi, Giuseppe Augello, et al. Robotic magnetic navigation for atrial fibrillation ablation. *Journal of the American College of Cardiology*, 47(7):1390–1400, 2006.

[28] Zohaib A Shaikh, Michael F Eilenberg, and Todd J Cohen. The amigo™ remote catheter system: From concept to bedside. *The Journal of Innovations in Cardiac Rhythm Management*, 8(8):2795, 2017.

[29] Ehtisham Mahmud, Jesse Naghi, Lawrence Ang, Jonathan Harrison, Omid Behnamfar, Ali Pourdjabbar, Ryan Reeves, and Mitul Patel. Demonstration of the safety and

feasibility of robotically assisted percutaneous coronary intervention in complex coronary lesions: results of the cora-pci study (complex robotically assisted percutaneous coronary intervention). *JACC: Cardiovascular Interventions*, 10(13):1320–1327, 2017.

[30] Tejas M Patel, Sanjay C Shah, Yash Y Soni, Rajni C Radadiya, Gaurav A Patel, Pradyot O Tiwari, and Samir B Pancholy. Comparison of robotic percutaneous coronary intervention with traditional percutaneous coronary intervention: A propensity score–matched analysis of a large cohort. *Circulation: Cardiovascular Interventions*, 13(5):e008888, 2020.

[31] Paul T Campbell, Kevin R Kruse, Christopher R Kroll, Janet Y Patterson, and Michele J Esposito. The impact of precise robotic lesion length measurement on stent length selection: ramifications for stent savings. *Cardiovascular Revascularization Medicine*, 16(6):348–350, 2015.

[32] Alexander Eric Rolls, Celia V Riga, Colin D Bicknell, Lesley Regan, Nick J Cheshire, and Mohamad S Hamady. Robot-assisted uterine artery embolization: a first-in-woman safety evaluation of the magellan system. *Journal of Vascular and Interventional Radiology*, 25(12):1841–1848, 2014.

[33] Jian Guo, Shuxiang Guo, Lin Shao, Peng Wang, and Qiang Gao. Design and performance evaluation of a novel robotic catheter system for vascular interventional surgery. *Microsystem Technologies*, 22(9):2167–2176, 2016.

[34] Shuxiang Guo, Nan Xiao, and Baofeng Gao. A novel robot-assisted catheter surgery system with force feedback. In *Selected Topics in Micro/Nano-robotics for Biomedical Applications*, pages 175–190. Springer, 2013.

[35] Jun Woo Park, Jaesoon Choi, Hui-Nam Pak, Seung Joon Song, Jung Chan Lee, Yongdoo Park, Seung Min Shin, and Kyung Sun. Development of a force-reflecting robotic platform for cardiac catheter navigation. *Artificial organs*, 34(11):1034–1039, 2010.

[36] Hedyeh Rafii-Tari, Jindong Liu, Su-Lin Lee, Colin Bicknell, and Guang-Zhong Yang. Learning-based modeling of endovascular navigation for collaborative robotic catheterization. In *International Conference on Medical Image Computing and Computer-Assisted Intervention*, pages 369–377. Springer, 2013.

[37] Mohammad Ali Tavallaei, Daniel Gelman, Michael Konstantine Lavdas, Allan C Skanes, Douglas L Jones, Jeffrey S Bax, and Maria Drangova. Design, development and evaluation of a compact telerobotic catheter navigation system. *The International Journal of Medical Robotics and Computer Assisted Surgery*, 12(3):442–452, 2016.

[38] Linshuai Zhang, Shuxiang Guo, Huadong Yu, and Yu Song. Performance evaluation of a strain-gauge force sensor for a haptic robot-assisted catheter operating system. *Microsystem Technologies*, 23(10):5041–5050, 2017.

[39] Honghua Zhao, Xingguang Duan, Qiang Huang, Xingtao Wang, Yue Chen, and Huatao Yu. Mechanical design and control system of vascular interventional robot. In *The 2011 IEEE/ICME International Conference on Complex Medical Engineering*, pages 357–362. IEEE, 2011.

[40] Jagadeesan Jayender, Mahdi Azizian, and Rajni V Patel. Autonomous robot-assisted active catheter insertion using image guidance. In *2007 IEEE/RSJ International Conference on Intelligent Robots and Systems IROS 2007*, pages 889–894. IEEE, 2007.

[41] Jagadeesan Jayender, Mahdi Azizian, and Rajni V Patel. Autonomous image-guided robot-assisted active catheter insertion. *IEEE Transactions on Robotics*, 24(4):858–871, 2008.

[42] Jagadeesan Jayender, Rajnikant V Patel, and Suwas Nikumb. Robot-assisted active catheter insertion: algorithms and experiments. *The International Journal of Robotics Research*, 28(9):1101–1117, 2009.

[43] Carlos Tercero, Seiichi Ikeda, Tomomi Uchiyama, Toshio Fukuda, Fumihito Arai, Yuta Okada, Yoshinari Ono, Ryohei Hattori, Tokunori Yamamoto, Makoto Negoro,

et al. Autonomous catheter insertion system using magnetic motion capture sensor for endovascular surgery. *The International Journal of Medical Robotics and Computer Assisted Surgery*, 3(1):52–58, 2007.

[44] Shuxiang Guo, Qianrui Chen, Nan Xiao, and Yuan Wang. A fuzzy pid control algorithm for the interventional surgical robot with guide wire feedback force. In *2016 IEEE International Conference on Mechatronics and Automation (ICMA)*, pages 426–430. IEEE, 2016.

[45] Wenqiang Chi, Jindong Liu, Hedyeh Rafii-Tari, Celia Riga, Colin Bicknell, and Guang-Zhong Yang. Learning-based endovascular navigation through the use of non-rigid registration for collaborative robotic catheterization. *International journal of computer assisted radiology and surgery*, 13(6):855–864, 2018.

[46] W. Chi, G. Dagnino, T. M. Y. Kwok, A. Nguyen, D. Kundrat, M. E. M. K. Abdelaziz, C. Riga, C. Bicknell, and G. Z. Yang. Collaborative robot-assisted endovascular catheterization with generative adversarial imitation learning. In *2020 IEEE International Conference on Robotics and Automation (ICRA)*, pages 2414–2420, 2020.

[47] Wenqiang Chi. Context-aware learning for robot-assisted endovascular catheterization. *Imperial College London*, 2019.

[48] Wenqiang Chi, Jindong Liu, Mohamed Emk Abdelaziz, Giulio Dagnino, Celia Riga, Colin Bicknell, and Guang-Zhong Yang. Trajectory optimization of robot-assisted endovascular catheterization with reinforcement learning. In *2018 IEEE/RSJ International Conference on Intelligent Robots and Systems (IROS)*, pages 3875–3881. IEEE, 2018.

[49] Shuxiang Guo, Yu Song, Xuanchun Yin, Linshuai Zhang, Takashi Tamiya, Hideyuki Hirata, and Hidenori Ishihara. A novel robot-assisted endovascular catheterization system with haptic force feedback. *IEEE Transactions on Robotics*, 35(3):685–696, 2019.

[50] H-J Cha, H-S Yoon, KY Jung, B-J Yi, S Lee, and JY Won. A robotic system for percutaneous coronary intervention equipped with a steerable catheter and force feedback function. In *2016 IEEE/RSJ International Conference on Intelligent Robots and Systems (IROS)*, pages 1151–1156. IEEE, 2016.

[51] Naveen Kumar Sankaran, Pramod Chembrammel, Adnan Siddiqui, Kenneth Snyder, and Thenkurussi Kesavadas. Design and development of surgeon augmented endovascular robotic system. *IEEE Transactions on Biomedical Engineering*, 65(11):2483–2493, 2018.

[52] Govindarajan Srimathveeravalli, Thenkurussi Kesavadas, and Xinyan Li. Design and fabrication of a robotic mechanism for remote steering and positioning of interventional devices. *The International Journal of Medical Robotics and Computer Assisted Surgery*, 6(2):160–170, 2010.

[53] T. Mei, C. Budelmann, T. A. Kern, S. Sindlinger, C. Minamisava, and R. Werthschutzky. Intravascular palpation and haptic feedback during angioplasty. In *World Haptics 2009 - Third Joint EuroHaptics conference and Symposium on Haptic Interfaces for Virtual Environment and Teleoperator Systems*, pages 380–381, 2009.

[54] Mitsutaka Tanimoto, Fumihito Arai, Toshio Fukuda, Kouichi Itoigawa, Masashi Hashimoto, Ikuo Takahashi, and Makoto Negoro. Telesurgery system for intravascular neurosurgery. In *International Conference on Medical Image Computing and Computer-Assisted Intervention*, pages 29–39. Springer, 2000.

[55] Yusof Ganji and Farrokh Janabi-Sharifi. Catheter kinematics and control to enhance cardiac ablation. In *Proc. SPIE*, volume 6374, pages 63740U–1, 2006.

[56] Klaus A Hausegger, Peter Schedlbauer, Hannes A Deutschmann, and Kurt Tiesenhausen. Complications in endoluminal repair of abdominal aortic aneurysms. *European journal of radiology*, 39(1):22–33, 2001.

[57] Carlotta Sorini Dini, Giulia Nardi, Francesca Ristalli, Alessio Mattesini, Brunilda

Hamiti, and Carlo Di Mario. Contemporary approach to heavily calcified coronary lesions. *Interventional Cardiology Review*, 14(3):154, 2019.

[58] Leigh-Ann Topfer and Carolyn Spry. New technologies for the treatment of peripheral artery disease. In *CADTH Issues in Emerging Health Technologies*. Canadian Agency for Drugs and Technologies in Health, 2018.

[59] Jorg Ederle, Roland L Featherstone, and Martin M Brown. Randomized controlled trials comparing endarterectomy and endovascular treatment for carotid artery stenosis: a cochrane systematic review. *Stroke*, 40(4):1373–1380, 2009.

[60] Henrik Gensicke, Thomas Zumbrunn, Lisa M Jongen, Paul J Nederkoorn, Sumaira Macdonald, Peter A Gaines, Philippe A Lyrer, Stephan G Wetzel, Aad van der Lugt, Willem P Th M Mali, et al. Characteristics of ischemic brain lesions after stenting or endarterectomy for symptomatic carotid artery stenosis: results from the international carotid stenting study–magnetic resonance imaging substudy. *Stroke*, 44(1):80–86, 2013.

[61] Frank D Hammer, Valerie Lacroix, Thierry Duprez, Cecile Grandin, Robert Verhelst, Andre Peeters, and Guy Cosnard. Cerebral microembolization after protected carotid artery stenting in surgical high-risk patients: results of a 2-year prospective study. *Journal of vascular surgery*, 42(5):847–853, 2005.

[62] Eugenio Stabile, Anna Sannino, Gabriele Giacomo Schiattarella, Giuseppe Gargiulo, Evelina Toscano, Linda Brevetti, Fernando Scudiero, Giuseppe Giugliano, Cinzia Perrino, Bruno Trimarco, et al. Cerebral embolic lesions detected with diffusion-weighted magnetic resonance imaging following carotid artery stenting: a meta-analysis of 8 studies comparing filter cerebral protection and proximal balloon occlusion. *JACC: Cardiovascular Interventions*, 7(10):1177–1183, 2014.

[63] Klaudija Bijuklic, Andreas Wandler, Fadia Hazizi, and Joachim Schofer. The profi study (prevention of cerebral embolization by proximal balloon occlusion compared

to filter protection during carotid artery stenting): a prospective randomized trial. *Journal of the American College of Cardiology*, 59(15):1383–1389, 2012.

[64] Piero Montorsi, Luigi Caputi, Stefano Galli, Elisa Ciceri, Giovanni Ballerini, Marco Agrifoglio, Paolo Ravagnani, Daniela Trabattoni, Gianluca Pontone, Franco Fabbiocchi, et al. Microembolization during carotid artery stenting in patients with high-risk, lipid-rich plaque: a randomized trial of proximal versus distal cerebral protection. *Journal of the American College of Cardiology*, 58(16):1656–1663, 2011.

[65] Craig R Smith, Martin B Leon, Michael J Mack, D Craig Miller, Jeffrey W Moses, Lars G Svensson, E Murat Tuzcu, John G Webb, Gregory P Fontana, Raj R Makkar, et al. Transcatheter versus surgical aortic-valve replacement in high-risk patients. *New England Journal of Medicine*, 364(23):2187–2198, 2011.

[66] Heyder Omran, Harald Schmidt, Matthias Hackenbroch, Stefan Illien, Peter Bernhardt, Giso von der Recke, Rolf Fimmers, Sebastian Flacke, Günter Layer, Christoph Pohl, et al. Silent and apparent cerebral embolism after retrograde catheterisation of the aortic valve in valvular stenosis: a prospective, randomised study. *The Lancet*, 361(9365):1241–1246, 2003.

[67] Jean Bismuth, Zsolt Garami, Javier E Anaya-Ayala, Joseph J Naoum, Hosam F El Sayed, Eric K Peden, Alan B Lumsden, and Mark G Davies. Transcranial doppler findings during thoracic endovascular aortic repair. *Journal of vascular surgery*, 54(2):364–369, 2011.

[68] Vivek Y Reddy, Dipen Shah, Josef Kautzner, Boris Schmidt, Nadir Saoudi, Claudia Herrera, Pierre Jaïs, Gerhard Hindricks, Petr Peichl, Aude Yulzari, et al. The relationship between contact force and clinical outcome during radiofrequency catheter ablation of atrial fibrillation in the toccata study. *Heart rhythm*, 9(11):1789–1795, 2012.

[69] Andrea Natale, Vivek Y Reddy, George Monir, David J Wilber, Bruce D Lindsay, H Thomas McElderry, Charan Kantipudi, Moussa C Mansour, Daniel P Melby,

Douglas L Packer, et al. Paroxysmal af catheter ablation with a contact force sensing catheter: results of the prospective, multicenter smart-af trial. *Journal of the American College of Cardiology*, 64(7):647–656, 2014.

[70] Josef Kautzner, Petr Neuzil, Hendrik Lambert, Petr Peichl, Jan Petru, Robert Cihak, Jan Skoda, Dan Wichterle, Erik Wissner, Aude Yulzari, and Karl-Heinz Kuck. EFFICAS II: optimization of catheter contact force improves outcome of pulmonary vein isolation for paroxysmal atrial fibrillation. *EP Europace*, 17(8):1229–1235, 06 2015.

[71] Luigi Di Biase, Andrea Natale, Conor Barrett, Carmela Tan, Claude S Elayi, Chi Keong Ching, Paul Wang, Amin Al-Ahmad, Mauricio Arruda, J David Burkhardt, et al. Relationship between catheter forces, lesion characteristics,"popping," and char formation: experience with robotic navigation system. *Journal of cardiovascular electrophysiology*, 20(4):436–440, 2009.

[72] Yasuo Okumura, Susan B Johnson, T Jared Bunch, Benhur D Henz, Christine J O'BRIEN, and Douglas L Packer. A systematical analysis of in vivo contact forces on virtual catheter tip/tissue surface contact during cardiac mapping and intervention. *Journal of cardiovascular electrophysiology*, 19(6):632–640, 2008.

[73] John Whitaker, Jeffrey Fish, James Harrison, Henry Chubb, Steven E Williams, Thomas Fastl, Cesare Corrado, Jérôme Van Zaen, Jennifer Gibbs, Louisa O'Neill, et al. Lesion index–guided ablation facilitates continuous, transmural, and durable lesions in a porcine recovery model. *Circulation: Arrhythmia and Electrophysiology*, 11(4):e005892, 2018.

[74] Felix Bourier, Gabriele Hessling, Sonia Ammar-Bucsh, Marc Kottmaier, Alessandra Buiatti, Christian Grebmer, Marta Telishevska, Verena Semmler, Carsten Lennerz, Christine Schneider, et al. Electromagnetic contact-force sensing electrophysiological catheters: How accurate is the technology? *Journal of Cardiovascular Electrophysiology*, 27(3):347–350, 2016.

[75] Christopher J Payne, Hedyeh Rafii-Tari, and Guang-Zhong Yang. A force feedback system for endovascular catheterisation. In *2012 IEEE/RSJ International Conference on Intelligent Robots and Systems (IROS)*, pages 1298–1304. IEEE, 2012.

[76] R Ahmadi, J Dargahi, M Packirisamy, and R Cecere. A new hybrid catheter-tip tactile sensor with relative hardness measuring capability for use in catheter-based heart surgery. In *SENSORS, 2010 IEEE*, pages 1592–1595. IEEE, 2010.

[77] Yili Fu, Anzhu Gao, Hao Liu, and Shuxiang Guo. The master-slave catheterisation system for positioning the steerable catheter. *International Journal of Mechatronics and Automation*, 1(3-4):143–152, 2011.

[78] Carola Strandman, Leif Smith, Lars Tenerz, and Bertil Hök. A production process of silicon sensor elements for a fibre-optic pressure sensor. *Sensors and Actuators A: Physical*, 63(1):69–74, 1997.

[79] Panagiotis Polygerinos, Lakmal D Seneviratne, Reza Razavi, Tobias Schaeffter, and Kaspar Althoefer. Triaxial catheter-tip force sensor for mri-guided cardiac procedures. *IEEE/ASME Transactions on mechatronics*, 18(1):386–396, 2013.

[80] Panagiotis Polygerinos, Dinusha Zbyszewski, Tobias Schaeffter, Reza Razavi, Lakmal D Seneviratne, and Kaspar Althoefer. Mri-compatible fiber-optic force sensors for catheterization procedures. *IEEE Sensors Journal*, 10(10):1598–1608, 2010.

[81] Zhenda Yang, Hao Liu, Yuanyuan Zhou, Anzhu Gao, and Hongyi Li. A miniature force sensor for catheter based on optical micro deformation detection. In *2015 IEEE International Conference on Cyber Technology in Automation, Control, and Intelligent Systems (CYBER)*, pages 441–445. IEEE, 2015.

[82] Daniele Tosi, Edoardo Gino Macchi, Giovanni Braschi, Alfredo Cigada, Mario Gallati, Sandro Rossi, Sven Poeggel, Gabriel Leen, and Elfed Lewis. Fiber-optic combined fpi/fbg sensors for monitoring of radiofrequency thermal ablation of liver tumors: ex vivo experiments. *Applied optics*, 53(10):2136–2144, 2014.

[83] Panagiotis Polygerinos, Pinyo Puangmali, Tobias Schaeffter, Reza Razavi, Lakmal D Seneviratne, and Kaspar Althoefer. Novel miniature mri-compatible fiber-optic force sensor for cardiac catheterization procedures. In *2010 IEEE International Conference on Robotics and Automation*, pages 2598–2603. IEEE, 2010.

[84] P. Polygerinos, A. Ataollahi, T. Schaeffter, R. Razavi, L. D. Seneviratne, and K. Althoefer. Mri-compatible intensity-modulated force sensor for cardiac catheterization procedures. *IEEE Transactions on Biomedical Engineering*, 58(3):721–726, 2011.

[85] Hao Su, Iulian I Iordachita, Junichi Tokuda, Nobuhiko Hata, Xuan Liu, Reza Seifabadi, Sheng Xu, Bradford Wood, and Gregory S Fischer. Fiber-optic force sensors for mri-guided interventions and rehabilitation: A review. *IEEE sensors journal*, 17(7):1952–1963, 2017.

[86] David B Camarillo, Christopher F Milne, Christopher R Carlson, Michael R Zinn, and J Kenneth Salisbury. Mechanics modeling of tendon-driven continuum manipulators. *IEEE Transactions on Robotics*, 24(6):1262–1273, 2008.

[87] Mahta Khoshnam, Mahdi Azizian, and Rajni V Patel. Modeling of a steerable catheter based on beam theory. In *2012 IEEE International Conference on Robotics and Automation (ICRA)*, pages 4681–4686. IEEE, 2012.

[88] Mahta Khoshnam and Rajni V Patel. A pseudo-rigid-body 3r model for a steerable ablation catheter. In *2013 IEEE International Conference on Robotics and Automation (ICRA)*, pages 4427–4432. IEEE, 2013.

[89] Mahta Khoshnam and Rajni V Patel. Estimating contact force for steerable ablation catheters based on shape analysis. In *2014 IEEE/RSJ International Conference on Intelligent Robots and Systems (IROS 2014)*, pages 3509–3514. IEEE, 2014.

[90] Mahta Khoshnam, Peyman Yadmellat, and Rajni V Patel. Black-box modeling and control of steerable ablation catheters. In *2016 IEEE International Conference on Advanced Intelligent Mechatronics (AIM)*, pages 1192–1197. IEEE, 2016.

[91] D Caleb Rucker and Robert J Webster. Deflection-based force sensing for continuum robots: A probabilistic approach. In *2011 IEEE/RSJ International Conference on Intelligent Robots and Systems*, pages 3764–3769. IEEE, 2011.

[92] Kai Xu and Nabil Simaan. An investigation of the intrinsic force sensing capabilities of continuum robots. *IEEE Transactions on Robotics*, 24(3):576–587, 2008.

[93] Junghwan Back, Thomas Manwell, Rashed Karim, Kawal Rhode, Kaspar Althoefer, and Hongbin Liu. Catheter contact force estimation from shape detection using a real-time cosserat rod model. In *2015 IEEE/RSJ International Conference on Intelligent Robots and Systems (IROS)*, pages 2037–2042. IEEE, 2015.

[94] Shahir Hasanzadeh and Farrokh Janabi-Sharifi. An efficient static analysis of continuum robots. *Journal of Mechanisms and Robotics*, 6(3), 2014.

[95] S. Hasanzadeh and F. Janabi-Sharifi. Model-based force estimation for intracardiac catheters. *IEEE/ASME Transactions on Mechatronics*, 21(1):154–162, 2016.

[96] Minou Kouh Soltani, Sohrab Khanmohammadi, and Farzan Ghalichi. A three-dimensional shape-based force and stiffness-sensing platform for tendon-driven catheters. *Sensors*, 16(7):990, 2016.

[97] Shun Li, Jixiang Guo, Qiong Wang, Qiang Meng, Yim-Pan Chui, Jing Qin, and Pheng-Ann Heng. A catheterization-training simulator based on a fast multigrid solver. *IEEE computer graphics and applications*, 32(6):56–70, 2012.

[98] Shun Li, Jing Qin, Jixiang Gao, Yim-Pan Chui, and Pheng-Ann Heng. A novel fem-based numerical solver for interactive catheter simulation in virtual catheterization. *Journal of Biomedical Imaging*, 2011:3, 2011.

[99] Maisheng Luo, Hongzhi Xie, Le Xie, Ping Cai, and Lixu Gu. A robust and real-time vascular intervention simulation based on kirchhoff elastic rod. *Computerized Medical Imaging and Graphics*, 38(8):735–743, 2014.

[100] Wen Tang, Tao Ruan Wan, Derek A Gould, Thien How, and Nigel W John. A stable and real-time nonlinear elastic approach to simulating guidewire and catheter insertions based on cosserat rod. *IEEE Transactions on Biomedical Engineering*, 59(8):2211–2218, 2012.

[101] Julien Lenoir, Stephane Cotin, Christian Duriez, and Paul Neumann. Interactive physically-based simulation of catheter and guidewire. *Computers & Graphics*, 30(3):416–422, 2006.

[102] Mahta Khoshnam, Aaron Yurkewich, and Rajni V Patel. Model-based force control of a steerable ablation catheter with a custom-designed strain sensor. In *2013 IEEE International Conference on Robotics and Automation (ICRA)*, pages 4479–4484. IEEE, 2013.

[103] Samuel B Kesner and Robert D Howe. Position control of motion compensation cardiac catheters. *IEEE Transactions on Robotics*, 27(6):1045–1055, 2011.

[104] Samuel B Kesner and Robert D Howe. Robotic catheter cardiac ablation combining ultrasound guidance and force control. *The International Journal of Robotics Research*, 33(4):631–644, 2014.

[105] S. B. Kesner and R. D. Howe. Force control of flexible catheter robots for beating heart surgery. In *2011 IEEE International Conference on Robotics and Automation*, pages 1589–1594, 2011.

[106] Daniel Gelman, Allan C Skanes, Mohammad A Tavallaei, and Maria Drangova. Design and evaluation of a catheter contact-force controller for cardiac ablation therapy. *IEEE Transactions on Biomedical Engineering*, 63(11):2301–2307, 2016.

[107] J. Jayender, R. V. Patel, and S. Nikumb. Robot-assisted catheter insertion using hybrid impedance control. In *Proceedings 2006 IEEE International Conference on Robotics and Automation, 2006. ICRA 2006.*, pages 607–612, 2006.

[108] Biosense webster, inc. - defining the field of electrophysiology. https://www.biosensewebster.com/, 2017.

[109] Tacticath™ quartz contact force ablation catheter — st. jude medical. https://www.sjmglobal.com/, 2018.

[110] Mahta Khoshnam, Allan C Skanes, and Rajni V Patel. Modeling and estimation of tip contact force for steerable ablation catheters. *IEEE Transactions on Biomedical Engineering*, 62(5):1404–1415, 2015.

[111] J. Back, L. Lindenroth, R. Karim, K. Althoefer, K. Rhode, and H. Liu. New kinematic multi-section model for catheter contact force estimation and steering. In *2016 IEEE/RSJ International Conference on Intelligent Robots and Systems (IROS)*, pages 2122–2127, Oct 2016.

[112] S. Hasanzadeh and F. Janabi-Sharifi. Model-based force estimation for intracardiac catheters. *IEEE/ASME Transactions on Mechatronics*, 21(1):154–162, Feb 2016.

[113] Juliette Gindre, A Bel-Brunon, Michel Rochette, Antoine Lucas, Adrien Kaladji, Pascal Haigron, and Alain Combescure. Patient-specific finite-element simulation of the insertion of guidewire during an evar procedure: Guidewire position prediction validation on 28 cases. *IEEE Transactions on Biomedical Engineering*, 64(5):1057–1066, 2017.

[114] A. Hooshiar, M. Razban, N. M. Bandari, and J. Dargahi. Sensing principle for real-time characterization of viscoelasticity in the beating myocardial tissue. In *2017 IEEE International Conference on Computational Intelligence and Virtual Environments for Measurement Systems and Applications (CIVEMSA)*, pages 72–77, June 2017.

[115] Hedyeh Rafii-Tari, Christopher J Payne, and Guang-Zhong Yang. Current and emerging robot-assisted endovascular catheterization technologies: a review. *Annals of biomedical engineering*, 42(4):697–715, 2014.

[116] Maria Panayiotou, Andrew P King, R James Housden, YingLiang Ma, Michael Truong, Michael Cooklin, Mark O'Neill, Jaswinder Gill, C Aldo Rinaldi, and Kawal S Rhode. Image-based view-angle independent cardiorespiratory motion gating for x-ray-guided interventional electrophysiology procedures. In *International Workshop on Statistical Atlases and Computational Models of the Heart*, pages 158–167. Springer, 2014.

[117] Ali Al Moussawi, Cedric Galusinski, and Christian Nguyen. 3d reconstruction of blood vessels. *Engineering with Computers*, 31(4):775–790, Oct 2015.

[118] YingLiang Ma, Nicolas Gogin, Pascal Cathier, R James Housden, Geert Gijsbers, Michael Cooklin, Mark O'Neill, Jaswinder Gill, C Aldo Rinaldi, Reza Razavi, et al. Real-time x-ray fluoroscopy-based catheter detection and tracking for cardiac electrophysiology interventions. *Medical physics*, 40(7), 2013.

[119] Amplatz super stiff™ guidewire - boston scientific. `http://www.bostonscientific.com/en-US/products/guidewires/amplatz-super-stiff.html`, 2018.

[120] JD Kakisis, ED Avgerinos, CN Antonopoulos, TG Giannakopoulos, K Moulakakis, and CD Liapis. The european society for vascular surgery guidelines for carotid intervention: an updated independent assessment and literature review. *European Journal of Vascular and Endovascular Surgery*, 44(3):238–243, 2012.

[121] RGA Ackerstaff, Angioplasty Antonius Carotid Endarterectomy, and Stenting Study Group. Transcranial doppler monitoring in angioplasty and stenting of the carotid bifurcation. *Journal of Endovascular Therapy*, 10(4):702–710, 2003.

[122] H.J. Kim, H.J. Lee, J.H. Yang, I.S. Yeo, J.S. Yi, I.W. Lee, S.B. Lee, S.Y. Ryu, J.K. Kim, and P.S. Yang. The influence of carotid artery catheterization technique on the incidence of thromboembolism during carotid artery stenting. *American Journal of Neuroradiology*, 31(9):1732–1736, 2010.

[123] Niten Singh and David Deaton. Endovascular interventions. In *Surgical Pitfalls*, pages 651–656. Elsevier, 2009.

[124] George A Antoniou, Celia V Riga, Erik K Mayer, Nicholas JW Cheshire, and Colin D Bicknell. Clinical applications of robotic technology in vascular and endovascular surgery. *Journal of vascular surgery*, 53(2):493–499, 2011.

[125] Nathaniel R Smilowitz and Giora Weisz. Robotic-assisted angioplasty: current status and future possibilities. *Current cardiology reports*, 14(5):642–646, 2012.

[126] Joseph P Carrozza. Robotic-assisted percutaneous coronary intervention—filling an unmet need. *Journal of cardiovascular translational research*, 5(1):62–66, 2012.

[127] Celia V Riga, Colin D Bicknell, Alexander Rolls, Nicholas J Cheshire, and Mohamad S Hamady. Robot-assisted fenestrated endovascular aneurysm repair (fevar) using the magellan system. *Journal of Vascular and Interventional Radiology*, 24(2):191–196, 2013.

[128] Xianqiang Bao, Shuxiang Guo, Nan Xiao, Youxiang Li, Cheng Yang, Rui Shen, Jinxin Cui, Yuhua Jiang, Xinke Liu, and Keyun Liu. Operation evaluation in-human of a novel remote-controlled vascular interventional robot. *Biomedical microdevices*, 20(2):34, 2018.

[129] Alvin I Chen, Max L Balter, Timothy J Maguire, and Martin L Yarmush. Deep learning robotic guidance for autonomous vascular access. *Nature Machine Intelligence*, 2(2):104–115, 2020.

[130] Karl-Heinz Kuck, Vivek Y Reddy, Boris Schmidt, Andrea Natale, Petr Neuzil, Nadir Saoudi, Josef Kautzner, Claudia Herrera, Gerhard Hindricks, Pierre Jaïs, et al. A novel radiofrequency ablation catheter using contact force sensing: Toccata study. *Heart rhythm*, 9(1):18–23, 2012.

[131] Yusof Ganji, Farrokh Janabi-Sharifi, et al. Catheter kinematics for intracardiac navigation. *IEEE Transactions on Biomedical Engineering*, 56(3):621–632, 2009.

[132] Hedyeh Rafii-Tari, Celia V Riga, Christopher J Payne, Mohamad S Hamady, Nicholas JW Cheshire, Colin D Bicknell, and Guang-Zhong Yang. Reducing contact

forces in the arch and supra-aortic vessels using the magellan robot. *Journal of vascular surgery*, 64(5):1422–1432, 2016.

[133] Hedyeh Rafii-Tari, Christopher J Payne, Colin Bicknell, Ka-Wai Kwok, Nicholas JW Cheshire, Celia Riga, and Guang-Zhong Yang. Objective assessment of endovascular navigation skills with force sensing. *Annals of biomedical engineering*, 45(5):1315–1327, 2017.

[134] Masoud Razban, Javad Dargahi, and Benoit Boulet. A sensor-less catheter contact force estimation approach in endovascular intervention procedures. In *2018 IEEE/RSJ International Conference on Intelligent Robots and Systems (IROS)*, pages 2100–2106. IEEE, 2018.

[135] J. F. Canny. Computational approach to edge detection. *IEEE Transactions on Pattern Analysis and Machine Intelligence*, 8:679–698, Nov. 1986.

[136] R. E. Woods R. C. Gonzalez. Digital image processing. *Prentice Hall International*, 2002.

[137] Stephan P Timoshenko. X. on the transverse vibrations of bars of uniform cross-section. *The London, Edinburgh, and Dublin Philosophical Magazine and Journal of Science*, 43(253):125–131, 1922.

[138] DL Thomas, JM Wilson, and RR Wilson. Timoshenko beam finite elements. *Journal of Sound and Vibration*, 31(3):315–330, 1973.

[139] JN Reddy. On the dynamic behaviour of the timoshenko beam finite elements. *Sadhana*, 24(3):175–198, 1999.

[140] Klaus-Jürgen Bathe, Ekkehard Ramm, and Edward L Wilson. Finite element formulations for large deformation dynamic analysis. *International journal for numerical methods in engineering*, 9(2):353–386, 1975.

[141] Klaus-Jurgen Bathe. Finite element procedures. englewood cliffs, nj: Prentice-hall; 1996. In *rev. de: Finite element procedures in engineering analysis*. 1982.

[142] Janusz S Przemieniecki and Przemieniecki. *Theory of matrix structural analysis*, volume 1. McGraw-Hill New York, 1968.

[143] Klaus-Jürgen Bathe and Said Bolourchi. Large displacement analysis of three-dimensional beam structures. *International journal for numerical methods in engineering*, 14(7):961–986, 1979.

[144] Craig Walker. Guidewire selection for peripheral vascular interventions. *Endovascular Today*, 5:80–83, 2013.

[145] Hedyeh Rafii-Tari, Celia V. Riga, Christopher J. Payne, Mohamad S. Hamady, Nicholas J.W. Cheshire, Colin D. Bicknell, and Guang-Zhong Yang. Reducing contact forces in the arch and supra-aortic vessels using the magellan robot. *Journal of Vascular Surgery*, 64(5):1422 – 1432, 2016.

[146] Kundong Wang, Ximing Mai, Haijin Xu, Qingsheng Lu, and Weiwu Yan. A novel sea-based haptic force feedback master hand controller for robotic endovascular intervention system. *The International Journal of Medical Robotics and Computer Assisted Surgery*, page e2109, 2020.

[147] Kundong Wang, Jianyun Liu, Weiwu Yan, Qingsheng Lu, and Shengdong Nie. Force feedback controls of multi-gripper robotic endovascular intervention: design, prototype, and experiments. *International Journal of Computer Assisted Radiology and Surgery*, pages 1–14, 2020.

[148] Yuan Wang, Shuxiang Guo, Ping Guo, and Nan Xiao. Study on haptic feedback functions for an interventional surgical robot system. In *2015 IEEE International Conference on Mechatronics and Automation (ICMA)*, pages 715–720. IEEE, 2015.

[149] Yuhua Jiang, Keyun Liu, and Youxiang Li. Initial clinical trial of robot of endovascular treatment with force feedback and cooperating of catheter and guidewire. *Applied bionics and biomechanics*, 2018, 2018.

[150] Masoud Razban, Javad Dargahi, and Benoit Boulet. Image-based intraluminal contact force monitoring in robotic vascular navigation, arXiv: 2012.10762 (cs.RO), 2020.

[151] Werner Kraus Jr and Brenan J McCarragher. Modelling and control of interaction forces in nonlinear-stiffness types of contact. *IFAC Proceedings Volumes*, 30(20):657–662, 1997.

[152] Jinke Zhang and Lei Guo. Theory and design of pid controller for nonlinear uncertain systems. *IEEE Control Systems Letters*, 3(3):643–648, 2019.

[153] Zhaoshuo Li, Mahya Shahbazi, Niravkumar Patel, Eimear O'Sullivan, Haojie Zhang, Khushi Vyas, Preetham Chalasani, Anton Deguet, Peter L Gehlbach, Iulian Iordachita, et al. Hybrid robot-assisted frameworks for endomicroscopy scanning in retinal surgeries. *IEEE Transactions on Medical Robotics and Bionics*, 2(2):176–187, 2020.

[154] Peter H Lin, Ruth L Bush, Eric K Peden, Wei Zhou, Marlon Guerrero, Esteban A Henao, Panagiotis Kougias, Imran Mohiuddin, and Alan B Lumsden. Carotid artery stenting with neuroprotection: assessing the learning curve and treatment outcome. *The American journal of surgery*, 190(6):855–863, 2005.

[155] Leo H Bonati, Lisa M Jongen, Sven Haller, H Zwenneke Flach, Joanna Dobson, Paul J Nederkoorn, Sumaira Macdonald, Peter A Gaines, Annet Waaijer, Peter Stierli, et al. New ischaemic brain lesions on mri after stenting or endarterectomy for symptomatic carotid stenosis: a substudy of the international carotid stenting study (icss). *The Lancet Neurology*, 9(4):353–362, 2010.